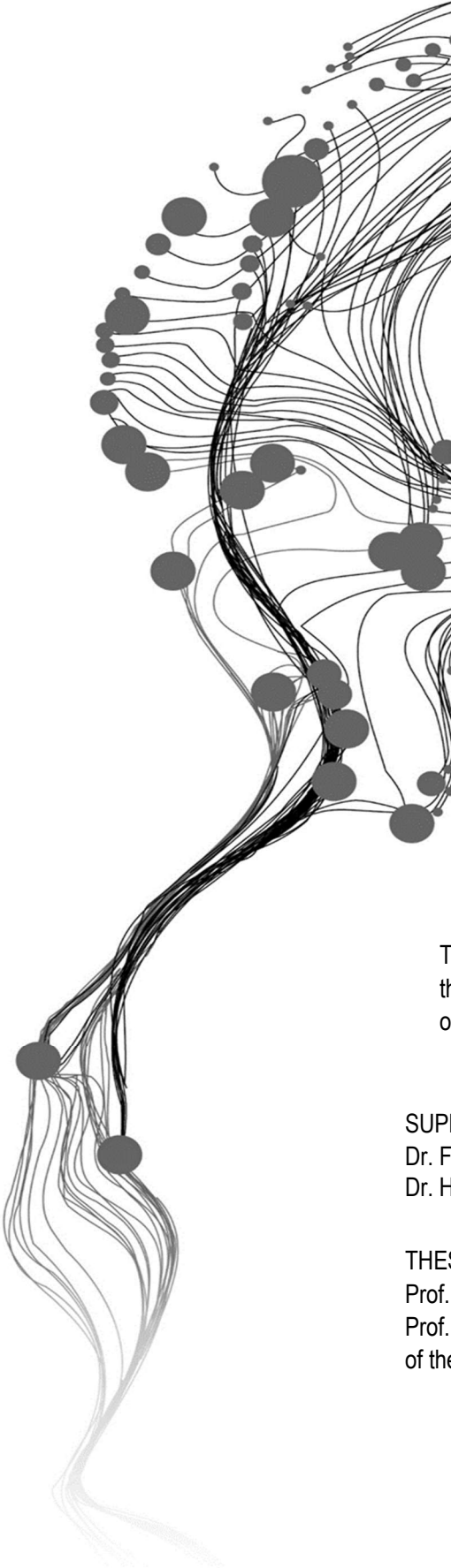


**DATA INTEGRATION FOR RECONSTRUCTING OF
VOLCANO-SEDIMENTARY SEQUENCES IN THE
COONGAN GREENSTONE BELT, EASTERN
PILBARA CRATON,**

MEAZA GIRMAY BOGALE
JUNE, 2020

SUPERVISORS:

Dr. F.J.A. van Ruitenbeek
Dr. H.M.A. van der Werff



DATA INTEGRATION FOR RECONSTRUCTING OF VOLCANO- SEDIMENTARY SEQUENCES IN THE COONGAN GREENSTONE BELT, EASTERN PILBARA CRATON,

MEAZA GIRMAY BOGALE

Enschede, The Netherlands, June, 2020

Thesis submitted to the Faculty of Geo-Information Science and Earth Observation of the University of Twente in partial fulfillment of the requirements for the degree of Master of Science in Geo-information Science and Earth Observation.

SUPERVISORS:

Dr. F.J.A. van Ruitenbeek

Dr. H.M.A. van der Werff

THESIS ASSESSMENT BOARD:

Prof. M. van der Meijde (Chair)

Prof. Dr. K. Hein (External Examiner, Emeritus & visiting professor at the University of the Witwatersrand in South Africa)

DISCLAIMER

This document describes work undertaken as part of a program of study at the Faculty of Geo-Information Science and Earth Observation of the University of Twente. All views and opinions expressed therein remain the sole responsibility of the author and do not necessarily represent those of the Faculty.

ABSTRACT

Archean greenstone belts are known for their ore deposits, diverse lithostratigraphy, and well-preserved evidence of the early earth. The Coongan greenstone belt, located in Western Australia, is one of the Archean greenstone belts, which is part of the Eastern Pilbara Craton. Rock units of the Coongan greenstone belt might be a host of economic ore deposits. Several studies have been done in the Coongan greenstone belt, mostly using geological field methods and geophysical interpretations. However, remote sensing methods for mapping mineral indices were not used in this area. Remote sensing data can provide information on abundances of different mineral groups, their relationship to the lithological units, and indications of hydrothermal alterations. Moreover, a data integration approach is useful in assessing the various geological aspects of an area and improving the quality of interpretation. Still, it is not well-known how the integration of gamma-ray and remote sensing data with geological field studies can improve the lithostratigraphic interpretation of the northern Coongan greenstone belt. Therefore this study aims at 1) providing surface mineral distribution maps, 2) determine the contribution of each dataset in the lithostratigraphic interpretations, 3) delineate the possible indications of hydrothermal alterations

Stratigraphic sequences of the study area were defined from the previous works (literature works and geological data). In this study, an integrated data analysis approach was used, including a quantitative and qualitative analysis of gamma-ray, ASTER, Sentinel-2, aerial photograph, and field observation datasets, as well as a geological map. Relationships were established based on the properties of the lithologic units in different datasets. A surface mineral distribution mapping and lithological interpretations were made using band ratio, visual interpretation, and image classification methods. Training and validation areas were selected for detailed lithological interpretations. The approach was a step-wise interpretation starting from interpretation of the broad lithological boundaries and going to a more detailed analysis. This approach was accomplished by starting from the 90-meter resolution gamma-ray data followed by a 30-meter resolution ASTER data, then Sentinel-2, and an aerial photograph. The gamma-ray and remote sensing images were classified based on the visual interpretations in the training and validation areas. After estimating the classification accuracies of the training and validation areas, the classifications were extrapolated to the whole study area. In this study, the validation area was used as an “uncommon” kind of validation that is to see the variations in radiometric/spectral characteristics of the lithologic units throughout the study area (i.e., not to assess the quality of classification).

The results of this interpretation were able to provide information on the surface distribution of minerals in the northern Coongan greenstone belt, to show the contribution of each dataset in reconstructing of the volcano-sedimentary stratigraphy, and to locate the possible indications of hydrothermal alterations. Ferrous iron, aluminum hydroxyl, kaolin group minerals, and iron oxides were the dominant minerals which were able to be mapped using ASTER-SWIR and Sentinel-2-VNIR images. In all datasets, visual interpretations were able to provide more accurate lithological boundaries compared to image classifications. Accuracy estimations in the training area show a partial decrease as more lithologic units were interpreted within the predefined boundaries. This partial decrease might be due to low spectral/radiometric contrast between the newly interpreted units. Classification accuracies in the training area were much higher than those in the validation area, which implies compositional variations in the stratigraphic units of the study area. Integration of remote sensing and gamma-ray data with geological field studies was able to improve the lithostratigraphic interpretation of the northern Coongan greenstone belt by adding more details, delineating accurate lithological boundaries, and determining the prominent areas of hydrothermal alteration. The chert units and gossans are examples of the new units delineated in this study but not in the previous studies. The

Duffer formation, which is part of the Warrawoona group rocks, was delineated as a hydrothermally altered unit.

Keywords: Archean, greenstone belt, Coongan, remote sensing, mineral indices, hydrothermal alteration, data integration, gamma-ray, ASTER, Sentinel-2, aerial photographs, field data, band ratio, visual interpretation, image classification

ACKNOWLEDGEMENTS

Glory to the Almighty God for His unlimited blessings throughout my life!

I would like to acknowledge the Orange Knowledge Program (OKP) and the International Institute for Geoinformation Science and Earth observation (ITC) for giving me a chance to join this program and arranging all the necessary logistics throughout my study period.

I would like to express my heartfelt gratitude to my supervisors' Dr. F.J.A. van Ruitenbeek (Frank) and Dr. H.M.A. van der Werff (Harald), for their continuous follow-up, and constructive criticism from the beginning to the end of this thesis. I thank them for making themselves available every time for me, leading me in the right direction, and introducing me to various new subjects. This thesis could not be facilitated without their excellent help.

I am very grateful to Prof. dr. K. Hein Emeritus & visiting professor at the University of the Witwatersrand in South Africa; for providing me a lot of data and information about the study area, including the field observation data, field notebook, and her document on the summary of the geology of the study area.

I would like to thank Prof. M. van der Meijde (Mark) for his constructive comments and advice during the proposal and midterm defenses.

I appreciate all the members of ITC and my friends for motivating me every time, especially in this hard time.

TABLE OF CONTENTS

1.	Introduction.....	1
1.1.	Research background and justification.....	1
1.2.	The radio element content of rocks.....	2
1.3.	Research problem.....	3
1.4.	Research objectives and research questions.....	4
2.	Geology of the study area and literature review.....	5
3.	Data and software.....	8
3.1.	Software.....	8
3.2.	Data.....	8
4.	Methodology.....	10
4.1.	Pre-processing.....	10
4.2.	Vegetation cover analysis.....	10
4.3.	Mineral indices.....	10
4.4.	The overall geological interpretation approach.....	11
4.5.	Lithological interpretation.....	12
4.6.	Indicators of hydrothermal alteration.....	14
5.	Results.....	15
5.1.	Pre-processing.....	15
5.2.	Vegetation cover analysis.....	15
5.3.	Mineral indices.....	15
5.4.	Lithological interpretations.....	21
6.	Discussion.....	36
6.1.	Mineral indices.....	36
6.2.	Lithological interpretation and images classifications.....	37
6.3.	Hydrothermal alteration.....	42
6.4.	Chert layers of the Coongan greenstone belt.....	45
6.5.	Data integration.....	46
7.	Conclusion and recommendations.....	47
7.1.	Conclusion.....	47
7.2.	Recommendations.....	49

LIST OF FIGURES

Figure 1. 1: The stratigraphic sequence of the northern Coongan greenstone belt.	6
Figure 1. 2: Location map of the study area showing the main stratigraphic units	7
Figure 4. 1: Flow chart showing the general interpretation approach.	12
Figure 4. 2: summarized flow chart showing the interpretation steps.	14
Figure 5. 1: Spectral plots of ASTER mineral indices compared to USGS spectral libraries (Ferrous iron and FeOH)	16
Figure 5. 2: Spectra of AlOH group minerals extracted from the ASTER image compared to USGS spectral library plots.	17
Figure 5. 3: A color composite map of three mineral group indices.	18
Figure 5. 4: ASTER spectra of the kaolin group index compared to the USGS spectral library.	19
Figure 5. 5: MgOH group minerals spectra collected from ASTER image compared to USGS spectral library.	19
Figure 5. 6: Sentinel-2 band ratio (b4/b3) showing ferric iron content and comparison with the aerial photograph.	20
Figure 5. 7: Sentinel_2 spectral plots of goethite and hematite minerals.	21
Figure 5. 8: Visual interpretation of gamma-ray data along with two stripes as training and validation areas.	22
Figure 5. 9: A visual interpretation of ASTER enhanced images and mineral occurrence maps within the predefined boundaries using the gamma-ray data.	25
Figure 5. 10: Lithological interpretation along the training strip using sentinel_2 image.	30
Figure 5. 11: Maximum likelihood classified gamma-ray map and visually interpreted gamma-ray map of the training area.	32
Figure 5. 12: Maximum likelihood classified map of stacked gamma-ray and ASTER data and the visually interpreted ASTER image in the validation area.	33
Figure 5. 13: Surface area of the lithologic units versus the accuracy of classifications.	34
Figure 5. 14: Maximum likelihood classified map derived from stacked gamma-ray and ASTER data using classification signatures from the training area (extrapolation).	35
Figure 6. 1: Gamma-ray interpretations of the training and validation areas underlying the major stratigraphic boundaries of the northern Coongan greenstone belt.	41
Figure 6. 2: Maximum likelihood classified map of stacked gamma-ray, ASTER, and Sentinel-2 images. ...	43

LIST OF TABLES

Table 1.1: Types of radioelements and their characteristics	2
Table 1. 2: Radioelement content of common rocks and soils.....	3
Table 4. 1: Minerals mapping algorithms.....	11
Table 5. 1: lithological interpretation results of the training and validation strips using gamma-ray data. ..	23
Table 5. 2: Lithological interpretation of the training and validation strips using ASTER-SWIR data within the pre-defined boundaries from gamma-ray data.	26
Table 5. 3: Description of the lithological boundaries interpreted using Sentinel-2 data.	31

1. INTRODUCTION

1.1. Research background and justification

Mineral resources provide significant economic contributions to the development of our world. Finding new mineral deposits is needed to sustain the economic development of a country. Understanding the geology of an area is a critical element of mineral exploration, which assists in defining the potential mineral targets before intensive field exploration activities (Haldar, 2018). Mineral deposits are formed as part of natural earth processes. Geological processes that formed the mineral deposits are responsible for their location and distribution. Identification of rock types and deformation structures helps to understand the type of geological processes that formed the rock units (i.e., deposition, precipitation, volcanism) and the type of minerals that can be expected in an area. Mineral exploration activities usually include identification of predictive features such as hydrothermal alteration minerals (Yong-gui, Zheng-le, Xing-tong, & Bai-lin, 2014).

Hydrothermal alterations are mineralogical, compositional, and textural changes in rocks formed by the interaction of hot and chemically active fluids with surrounding rocks (Pirajno, 2010). This rock-fluid interaction process leads to a replacement of the primary minerals and the formation of new mineral assemblages (Van Kranendonk, 2006). Hydrothermal fluids usually carry economic minerals from the subsurface environment and placed them at a favorable location, such as faults and shear zones (Pirajno, 2010). Therefore, hydrothermally altered minerals are predictive features for economic mineral deposits, especially precious and metallic minerals, which have higher economic value (Yong-gui et al., 2014).

Archean greenstone belts are known sources of economic mineral deposits, and the interest of exploring them is increasing through time (Huston, Blewett, Mernaugh, Sun, & Kamprad, 2000). The diversified geological processes that happened during the Archean period resulted in several complex geological structures, and these structures are crucial features to be interpreted due to their purpose as hydrothermal fluid circulation pathways (Hickman & Van Kranendonk, 2012). In this thesis, the lithological contacts were studied as important geological structures.

Hydrothermal alteration processes and stratigraphic layering are the most important geological aspects of the study area (i.e., Coongan greenstone belt). Consequently, detailed analysis and integrating of different data sources are required to provide a complete geological interpretation of the study area. The need for data integration is to identify the various geological aspects of the study area (Slavinski et al., 2010). Remote sensing can provide surface mineralogical information, whereas integrating remote sensing with geophysical and field datasets can give mineralogical, lithological, alteration, and structural information (Schetselaar, Chung, & Kim, 2000).

The study of Archean greenstone belts is also crucial due to their importance as sources of the earliest evidence of earth's lithospheric history (Hickman & Van Kranendonk, 2012). Much information that can help to understand the composition of the mantle and tectonic processes of the earth can be extracted from Archean greenstone belts (Van Kranendonk, Hickman, Smithies, & Nelson, 2002). Although several works have been done in the eastern Pilbara craton, many of them did not include remote sensing methods. Further studies using updated data sources are still required to understand the mineralogy, stratigraphy, and hydrothermal alteration processes of the area.

The basic concepts of this study are generalized as components of hydrothermal alteration systems. The concept of hydrothermal alteration system comprises a host rock with which the hydrothermal fluids react,

weak zones through which the fluids migrate (e.g., faults and shear zones), and new mineral assemblages formed by the rock-fluid interaction (i.e., volcanogenic massive sulphides, and exhalative layers). Remote sensing image interpretation can deliver the mineral constituents of some host lithologies of the hydrothermal alteration system. Detecting the rock-forming minerals using remote sensing images can be used to identify the rock types. Ultramafic/mafic volcanic rocks, carbonate rocks, and iron formations are some of the lithologies of the Coongan greenstone belt that can be determined using remote sensing images (Scherrenberg, Hein, & White, 2004).

Hydrothermally altered units can be identified using the remote sensing images due to their mineralogical change compared to the host rocks, and their distinctive spectral characteristics. These features can also be identified using the airborne gamma-ray image because they usually show depletion/enrichment in radioelement contents compared to the host rocks (Chiozzi, Pasquale, & Verdoya, 2007; Maden & Akaryali, 2015). Rock units containing volcanic-hosted massive sulphides were expected to be found in the study area (Van Kranendonk, 2006). Volcanic hosted massive sulphides are ore deposits originated from volcanic-related hydrothermal alteration fluids and deposited at a seafloor (Shanks, 2012). These ore deposits are composed of sulphide minerals such as pyrite, chalcopyrite, and galena. They are well-known sources of metallic minerals such as zinc and copper (Solomon et al., 2004). Once the ore deposits expose to surface conditions, they quickly oxidize, and the sulphide minerals leached out. The oxidized rocks are called gossans, and they are compositionally rich in iron oxides (Shanks, 2012). Mineral constituents of gossans (iron oxides) are active in the VNIR wavelength range of the electromagnetic spectrum (van der Werff & van der Meer, 2015).

1.2. The radio element content of rocks

Most lithologic units show various ranges of radioactivity response due to the occurrence of the three radioactive elements potassium, thorium, and uranium. The element potassium is usually a common constituent of rock units, especially those with felsic composition. On the other hand, the elements thorium and uranium are associated with a few accessory minerals such as zircon and apatite (Dentith & Mudge, 2014). The abundance of these radioelements can be measured by airborne and ground-based gamma-ray methods. [Table 1.1](#) shows the abundance of the three radioelements on the earth's crust and their half-life. Half-life is the time taken for a radio element to decay half of its initial amount (Dentith & Mudge, 2014). Radioelements release energy during their decay processes. Gamma-ray spectrometry measures the energy emitted by radioelements and helps to count their concentration at a specific rock type (Wilford, Bierwirth, & Craig, 1997).

Table 1.1: Types of radioelements and their characteristics

Element	Radioactive isotope	Stable daughter isotope	Energy (MeV)	Half-life (*10 ⁹ years)
K	⁴⁰ K	⁴⁰ Ar	1.370–1.570	1.3
Th	²³² Th	²⁰⁸ Pb	2.410–2.810	13.9
U	²³⁸ U ²³⁵ U	²⁰⁸ Pb ²⁰⁷ Pb	1.660–1.860	4.46 0.71

The gamma-ray ternary image (RGB color composite of potassium, equivalent thorium, and equivalent uranium) uses to display the relative abundances of radio elements. The difference in relative abundances of the radioelements are indicators of lithological variations and are used to identify the contacts between contrasting lithologies (Youssef & Elkhodary, 2013). The total count channel of gamma-ray spectroscopy shows the total radioactivity of a rock. Rocks with higher total radioactivity displayed as white, and those with lower radioactivity show dark colors in the ternary image of the three radio elements (Dentith & Mudge, 2014). The channels of individual radioelements are used to express the absolute concentrations of the

radioelements whereas, the ratios of each radioelement channel give a relative abundance of one radioelement compared to the other radioelements (Dentith & Mudge, 2014; Wilford et al., 1997). Where a mineralizing process alters the initial radioactivity response of a rock, the resulting signature is related to alteration and provides exploration guidance (Ford, Harris, Shives, Carson, & Buckle, 2008). [Table 1.2](#) shows the radioactivity response of common rock groups and their weathering products according to (Nicolet & Erdi-Krausz, 2003; Wilford et al., 1997). The range of values mentioned in the table will be compared with the results of this thesis later.

Table 1. 2: Radioelement content of common rocks and soils.

Rock types	Rock			soil		
	K (%)	Th (ppm)	U (ppm)	K (%)	Th (ppm)	U (ppm)
Intrusive						
granitoids	0.4-4.5 (2.4)	2.3-45 (16)	0.4-7.8 (3.3)	0.4-3.9 (2.1)	2-37 (13)	0.5-7.8 (2.7)
Gneissic rock	2.4-3.8 (2.4)	18-55 (15)	2.1-3.6 (2.5)	0.7-1.9 (1.3)	6-19 (12)	1.6-3.8 (2.2)
pegmatite	2.6-5.5 (3.7)	0.3-9.6 (2)	0.3-1(0.7)			
Quartz-feldspar porphyry	1-5 (2.9)	6-14 (13)	1.3-2.9 (1,7)			
Intermediate intrusives	0.7-5.6 (2.7)	0.8-6.1 (2.4)	0.1-1.2 (0.8)	0.7-3.4 (1.6)	2.9-8.4(5.6)	1.5-2.3 (1.9)
Mafic intrusives	0.1-0.8 (0.4)	0-1.1 (0.3)	0.1-0.8 (0.4)	0.0-3.1 (1.2)		
Extrusives						
Felsic volcanics	2.0-4.4 (3.7)	13-28 (17)	1.4-13 (2.4)	1.8-3.2 (2.4)	10-18 (13)	1.5-2.4 (2.1)
Intermediate volcanics	1.8-4.1 (2.7)	1.5-15 (9)	0.9-5.6 (2.3)	1.0-17 (1.9)	4-17 (10)	1.2-3.6 (2.1)
Low K andesites	0.7-0.9 (0.8)	3-8 (5)	1.0-2.5 (1.6)	0.8-1.5 (1.1)	4-6 (5)	1.2-1.5 (1.3)
Mafic volcanics	0.3-1.3 (0.9)	2-5 (3.0)	0.3-1.3 (0.7)	0.2-1.4 (0.7)	3.3-13 (7.9)	0.6-2.5 (1.6)
Ultramafic volcanics	0.2-0.9 (0.4)	0-4 (1.2)	0.3-0.9 (0.6)	0.6	6	2.0
Sedimentary rocks						
Archean shales	0.4-1.6 (0.9)	1-5 (2.7)	0.3-1.3 (0.9)	0.8	3	1.2
carbonates	0.0-0.5 (0.2)	0-2.9 (1.4)	0.4-2.9 (1.6)			
sandstones	1.1		2.2			

1.3. Research problem

Geological maps and mineral occurrence maps are crucial in the exploration of economic mineral deposits. Geological studies related to lithostratigraphy of the Coongan greenstone belt have been done using geological field methods, geochemical analysis, and geophysical methods (Hickman & Van Kranendonk, 2012; Van Dijk, 2006; Van Kranendonk & Pirajno, 2004). However, it is not well known how the integration of remote sensing and gamma data with other geological datasets can help to better map and understand the volcano-sedimentary stratigraphy of the northern Coongan greenstone belt. Furthermore, remote sensing methods for mineral index mapping was not applied in the northern Coongan greenstone belt even

though it was used in other parts of the Eastern Pilbara Craton (Brown, Walter, & Cudahy, 2005; Brown, Cudahy, & Walter, 2006). Hence this study aims at 1) providing mineral occurrence maps, 2) determine the contribution of each dataset in the lithostratigraphic interpretations, 3) delineate the possible indications of hydrothermal alterations.

The use of remote sensing data for geological applications allows effective localization of mineral exploration targets and reduces cost, time, and human labor spent at fieldwork (Al-Nahmi et al., 2017). The ability of remote sensing methods to define surface mineral distribution is useful in identifying mineral groups that could be related to hydrothermal alteration processes and provides a clue for further mineral exploration.

1.4. Research objectives and research questions

1.4.1. General objective

The goal of this study is to determine how the integration of gamma-ray and remote sensing data with geological field data can improve the interpretation of the volcano-sedimentary stratigraphy of the northern Coongan greenstone belt as well as to show possible indications of hydrothermal alteration.

1.4.2. Specific objectives

1. To produce maps of mineral indices.
2. To show the contribution of each data in identifying the stratigraphic sequence of the study area.
3. To quantify the accuracy of the geological map that is resulted from the interpretation and classification of the remote sensing and gamma-ray data.
4. To identify the occurrence of hydrothermal alteration minerals.

1.4.3. Research Questions

- Which VNIR/SWIR active minerals are present in the study area?
- How does the contribution of each dataset can help in reconstructing the volcano-sedimentary sequence of the northern Coongan greenstone belt?
- What is the accuracy of the geological maps produced from geophysical and remote sensing data?
- Are there any indications of hydrothermal alteration processes? What are the unique characteristics of hydrothermal alteration minerals in different datasets?
- How does the data integration approach can improve the lithostratigraphic interpretation of the northern Coongan greenstone belt?

2. GEOLOGY OF THE STUDY AREA AND LITERATURE REVIEW

The Eastern Pilbara Craton is located in Western Australia and is one of the only two well-preserved mid-Archean granitoid-greenstone terrains on the earth. The other oldest preserved craton is the Kaapvaal Craton found in southern Africa (Van Kranendonk et al., 2002). The Eastern Pilbara Craton shows well-preserved evidence of Archean geological structures since there was no significant deformation after 2.8 Ga (Giga annum) in the area. According to Hickman & Van Kranendonk, (2012), stratigraphy and structures in the area together confirm that the Eastern Pilbara terrain was evolved by a magmatic intrusion, volcanism, and deformation processes. The lithology of Eastern Pilbara provides complete exposures of well-preserved Paleoproterozoic crust from which most of the information about the crustal processes has been obtained (Hickman & Van Kranendonk, 2012; Anhaeusser, 2014).

The Coongan greenstone belt (CGB) is part of the Eastern Pilbara Craton, which is located in the southwest of the Marble Bar township (Scherrenberg et al., 2004). It consists of the Warrawoona (ca. 3.525-3.426 Ga), Gorge Creek (ca. 3.05-2.94 Ga), Croydon (Ca. 2.97-2.94 Ga), Kelly (Ca. 3.35-3.30 Ga), Fortescue (Ca. 2.78-2.63 Ga), and Dalton suite (Ca. 3.20-3.07 Ga) group rock types (Geoscience Australia and Australian Stratigraphy Commission., 2017; Hein, Leeuw, Scherrenberg, Wijbrans, & S., n.d.) However, most of the Coongan greenstone belt is from the Warrawoona group of Pilbara supergroup (Zegers, 1996). The Coongan greenstone belt is composed of a succession of volcanic, volcano-sedimentary, and sedimentary rocks deposited during the middle Archean period (Scherrenberg et al., 2004). It consists of ultramafic, mafic, and intermediate volcanic rocks interbedded with sedimentary rocks like cherts, carbonates, and banded iron formations. It is characterized by a sub vertically tilted greenstone belt, which often intruded by ultramafic dikes and sills at various locations (Scherrenberg et al., 2004). The location map of the study area is displayed in [Figure 2.2](#) below with the summarized stratigraphic units based on (Geoscience Australia and Australian Stratigraphy Commission., 2017; Zegers, 1996) and the overlying field observation data by prof. dr. Kim Hein, emeritus & visiting professor at the University of the Witwatersrand in South Africa.

Stratigraphy of the Coongan greenstone belt was studied by (Hein, Leeuw, Scherrenberg, Wijbrans, & S., n.d.; Hickman & Van Kranendonk, 2012; Zegers, 1996). The 1:25,000 scale study by Hein et al., (n.d.) incorporates field observations, interpretation of aerial photographs, and topographic data. This paper is still unpublished, and it was used as a starting point for this thesis due to its specificity to the study area. The unpublished paper summarizes the stratigraphy and major geological structures of the northern Coongan greenstone belt. It summarizes the regional/local geology and major tectonic processes of the study area. This document is one of the latest/updated and detailed works undergone in the northern Coongan greenstone belt, the other being the 1:100,000 scale geological map by Hickman AH, Van Kranendonk, (2008) ([see Figure 2.2](#)). The main stratigraphic units of the study area described by (Hein et al., n.d.; Hickman AH, Van Kranendonk, 2008) can be summarized as follows. [Figure 2.1](#) is the chronological order of the main stratigraphic units of the study area, as published by Geoscience Australia and Australian Stratigraphy Commission., (2017).

- The Talga Talga subgroup comprises mafic and ultramafic volcanic rocks interbedded with dikes and sills of dolerite/gabbro as well as minor felsic volcanic rocks, banded iron formations, and chert layers. It occupies the western part of the study area and shows partial tilting in the north. It is approximately six kilometers thick.

- A felsic volcanic sequence nominated as the Duffer formation overlies the Talga Talga subgroup. The Duffer formation comprises rhyolite, dacite, agglomerate, sandstone, conglomerate, tuff breccia, and chert units. It is intercalation of volcanic and sedimentary rocks dated at ca. 3.471-3.463 Ga.
- The Strelley pool formation is a 20-25 meters thick unit underlain and overlain by the Duffer formation and Salgash subgroup, respectively. It is a chert unit known to contain morphologically diverse stromatolites and microfossils (Brown, Cudahy, & Walter, 2006).
- The Salgash subgroup of the Warrawoona group includes mafic and felsic volcanic rocks dated at 3.452-3.42 Ga. It consists of pillowed to komatiite basalts, chert, ash falls, tuff, siltstone, and felsic lava.
- The Wyman formation dated at ca. 3.32-3.31 Ga overlies the Salgash subgroup. The Wyman formation is composed of rhyolite, rhyodacite, and local felsic volcanic rocks interbedded with chert units. It is part of the Kelly group and covers several parts of the study area (see Fig.2.2).
- The Emu Pool supersite splits the southern half of the Talga Talga subgroup into western and eastern parts. This unit has relatively felsic composition compared to the surrounding mafic rocks. It includes meta-monzogranite, and mafic schist rock types dated at Ca. 3.32-3.29 Ga.
- The Cleaverville formation of the Gorge Creek group is a thick sedimentary sequence overlaying the Wyman formation. It is a banded iron formation dated Ca. 3.022-3.015 Ga, which is about 1 km thick. Residual Cenozoic sediments cover a large portion of this unit.

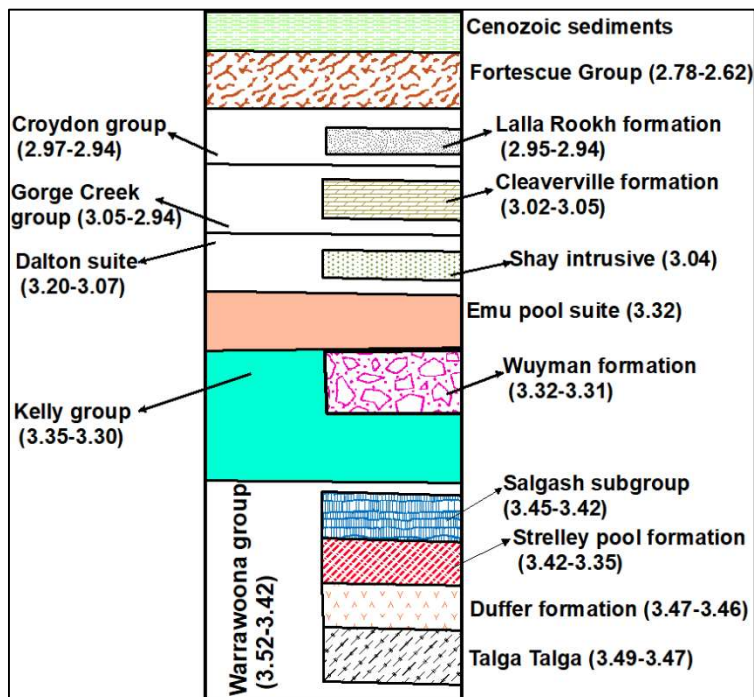


Figure 1. 1: The stratigraphic sequence of the northern Coongan greenstone belt (Geoscience Australia and Australian Stratigraphy Commission, 2017).

- The BIF unit is superimposed by a 1.5 km thick-bedded sandstone dated at 2.95-2.94 Ga. This overlying unit is called Lalla Rookh sandstone, which consists of sandstone, siltstone, and minor conglomerate. The Lalla Rookh sandstone is part of the Croydon group.
- The northern and northwestern parts of the study area are covered by pillowed and hyaloclastite breccia of the Mt Roe basalt (Fortescue group). The basalt is conformably overlain by sandstone

beds of the Hardey formation of the Fortescue group. The Fortescue group is dated at Ca. 2.629-2.780.

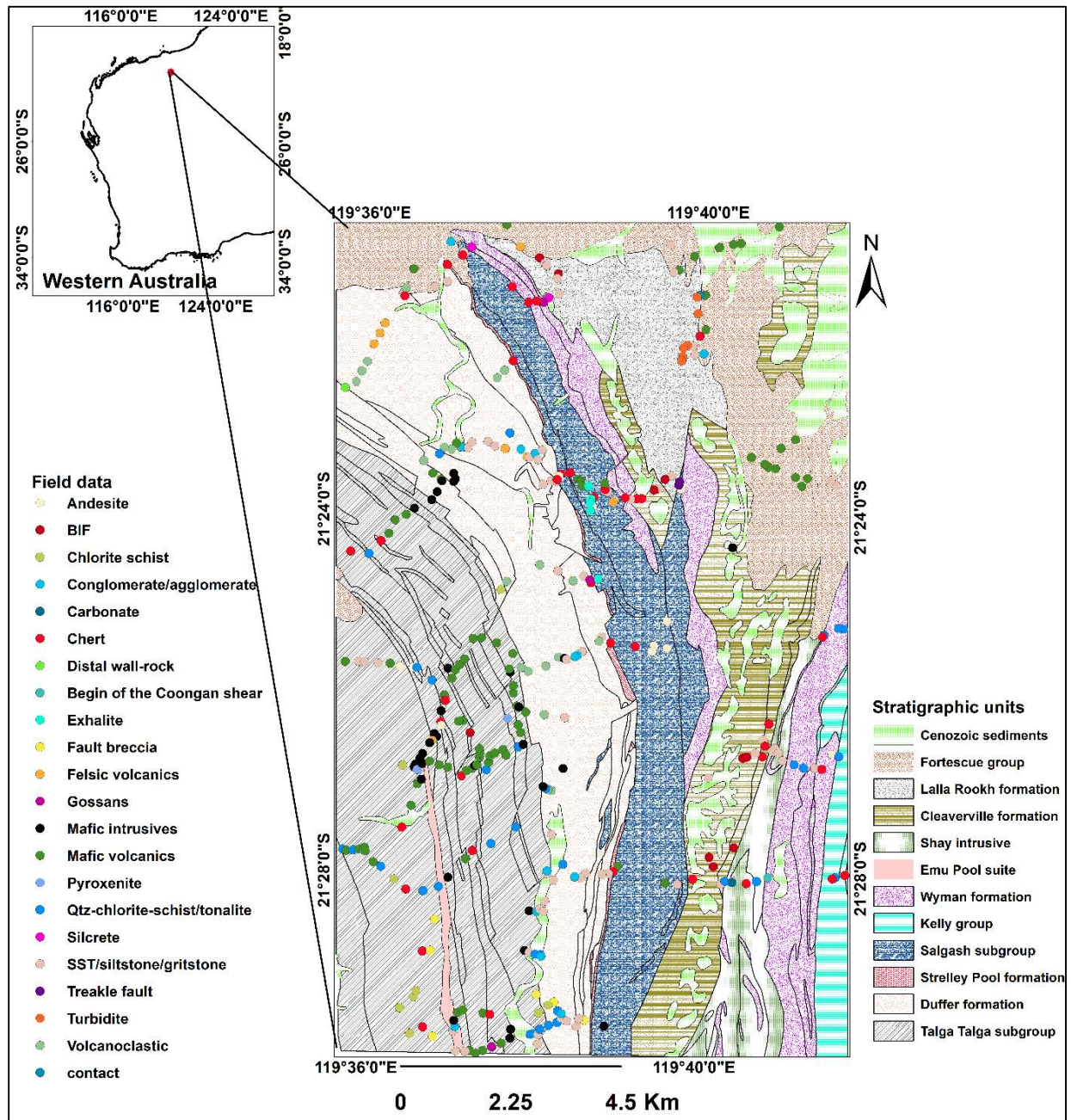


Figure 1.2: Location map of the study area showing the main stratigraphic units. The stratigraphic units were summarized from Hickman AH, Van Kranendonk, (2008)'s geological map. The original geological map is attached as [Appendix 1](#) with its descriptions. The stratigraphic hierarchy of the lithologic units is summarized in [Figure 2.1](#). The overlying field observation point data was collected by Prof. dr. Kim Hein, emeritus & visiting professor at the University of the Witwatersrand in South Africa.

The stratigraphic units of the northern Coongan greenstone belt show partial tilting. Several deformational structures disrupted the lateral stratigraphic sequences of the Coongan greenstone belt (Scherrenberg et al., 2004). Deformation is distributed throughout the study area and is oriented in N-S trending shear zones. Folds, faults, and shear zones dominate the general geometry of the greenstone belt (Zegers, 1996). The pattern that emerges shows a general E-W compressional event that happened between 3.3 and 3.2 Ga throughout the greenstone belt (Zegers, 1996).

3. DATA AND SOFTWARE

3.1. Software

[Envi 5.5.3](#) and [ArcMap 10.8](#) software were used for this research.

3.2. Data

3.2.1. ASTER SWIR image

The Advanced Spaceborne Thermal Emission and Reflection Radiometer (ASTER) is a high performance optical remote sensing instrument containing 14 spectral bands ranging from visible to thermal infrared. It has a spatial resolution of 15, 30, and 90 meters in the VNIR (0.56-0.86 μ m), SWIR (1.60-2.43 μ m), and TIR (8.125-11.65 μ m) wavelength regions respectively (Earth Remote Sensing Data Analysis Center, 2003). ASTER was launched on the EOS-Terra satellite on December 18, 1999, and it is collecting data since February 2000. However, the short wave infrared channels of ASTER stopped their operation in April 2008.

ASTER is the first multispectral spaceborne sensor able to discriminate OH-bearing minerals given the larger number of bands within the SWIR region. Certain diagnostic groups of hydrothermal minerals, such as clays, phyllosilicates, sulfates, and carbonates, can be identified based on their spectral signatures, with diagnostic features mainly in the shortwave infrared (SWIR) portion of the electromagnetic spectrum (Testa, Villanueva, Cooke, & Zhang, 2018). In this thesis, the VNIR and SWIR wavelength regions of ASTER data were used for vegetation cover analysis and geological interpretations, respectively.

The ASTER image used for this study was acquired on 8 November 2007. The pre-processing stage of the data was level-1A (i.e., reconstructed unprocessed instrument data). The ASTER data provided by ITC ([SC:AST L1A.003:2062403663 nov07](#)) had no metadata, and metadata was downloaded from <https://earthexplorer.usgs.gov/>.

3.2.2. Sentinel-2 image

Sentinel_2 data was used to map the occurrence of iron oxide minerals due to its relatively higher spectral resolution compared to the ASTER in the VNIR wavelength region. Sentinel-2 is an optical remote sensing instrument that contains 13 spectral bands. Four bands are at 10 m, six bands at 20 m, and three bands at 60 m spatial resolution (European Space Agency, 2015). Ten of the spectral bands are located at the VNIR range, and the remaining three bands are located at the SWIR wavelength range. Only the VNIR region was used for this study. Sentinel-2A satellite sensor is active since June 2015.

Level 2A Sentinel-2 image acquired on December 10/2019 was downloaded from NASA's website <https://scihub.copernicus.eu/dhus/#/home>. The criteria to download this image is the low cloudiness on that acquisition date.

3.2.3. Spectral libraries

ASTER and sentinel-2 spectral libraries used for this study were resampled from the USGS spectral libraries downloaded from <https://speclab.cr.usgs.gov/spectral-lib.html>.

3.2.4. Airborne gamma-ray data

Gamma-ray image acquired in 1996 by the Australian Geophysical Survey Organisation (AGSO) was used for this study. The spatial resolution of the image is approximately 90 meters. Deadtime correction, energy calibration, and background correction processes were already applied on it. The details about the processing

steps are explained by Richardson (1997). Gamma-ray data contains 256 energy channels and measures the content of potassium, equivalent thorium, and equivalent uranium in rocks and soils.

3.2.5. Aerial photograph

A mosaiced color aerial photograph at a spatial resolution of 0.77 meters provided by [ITC](#) was also used for this research.

3.2.6. Digital elevation model

A 30-meter spatial resolution Shuttle Radar Topography Mission (SRTM) digital elevation model was downloaded from the USGS website <https://earthexplorer.usgs.gov/>. The study area shows a 231-447 meters elevation.

3.2.7. Geological map

A 1:100,000 scale geological map published by Geological Survey of Western Australia was used as a source of lithological information and for comparison of the interpretation results (Hickman AH, Van Kranendonk, 2008). The geological map covers the entire Marble Bar area of Eastern Pilbara.

3.2.8. Field observation data

Field data were collected in 2005 by Prof. dr. Kim Hein, emeritus & visiting professor at the University of the Witwatersrand in South Africa. About five to six traverse lines along the east-west direction overlay the study area, as showing in [Figure 2.2](#).

4. METHODOLOGY

This section explains the details of the interpretation approach starting from the pre-processing, analysis of remote sensing images, and integration of all the datasets.

4.1. Pre-processing

All datasets were projected to WGS 84 UTM Zone 50 and resized to the same spatial extent. The gamma-ray and ASTER images, aerial photograph, geological map, and field observation datasets were in GCS_GDA_1994 projection, whereas the sentinel-2 image was in GCS_WGS_1984 projection.

4.1.1. ASTER pre-processing

Radiometric calibration was applied to the level-1A ASTER data after adding metadata to it. The log residuals method was used to convert the ASTER radiance data to surface reflectance (Gordon & Morel, 1983).

4.1.2. Sentinel-2 pre-processing

Level 2A is surface reflectance data, and there is no need for additional calibration and correction processes. Simple pre-processing steps (i.e., layer stacking, spatial sub-setting, and adding wavelength information) were undertaken.

4.2. Vegetation cover analysis

Before starting any geological interpretation, vegetation cover of the study area was checked by calculating normalized difference vegetation index (NDVI) using the ASTER and Sentinel-2 VNIR images. The reason for doing the vegetation cover analysis twice was because these images were acquired at different times, and temporal variation can affect the presence of vegetation in an area.

4.3. Mineral indices

Remote sensing technology is contributing significantly in geological studies, because it delivers a special opportunity to explore the geological characteristics of the remote areas without the requirement of physical access to an area on the ground (Al-Nahmi et al., 2017). Optical remote sensing examines materials on the earth based on their reflectance characteristics. In geological studies, variations in shape and wavelength position of spectral absorption features indicate changes in mineralogy and chemistry of the minerals and rocks under investigation (Hecker et al., 2017). In this study, ASTER and sentinel-2 remote sensing datasets were used for mineral and lithological interpretations.

Sentinel-2 VNIR and ASTER SWIR images were used to produce surface mineral distribution maps using band ratios developed by (Cudahy 2012; Van der Meer, van der Werff, & van Ruitenbeek, 2014) and others (see [Table 4.1](#)). Five mineral group indices (i.e., ferrous iron content, aluminum hydroxyl (AlOH) group content, kaolin group content, iron hydroxyl (FeOH) group content, and magnesium hydroxyl (MgOH) group content) were produced using ASTER SWIR band ratios. Band ratio can minimize topographic effects (Yong-gui et al., 2014).

The occurrence of iron oxides was analyzed using Sentinel-2 VNIR band ratios, as listed in [Table 4.1](#). The ratios and thresholds used for this interpretation include already published ones and newly developed ones. The occurrence of ferric iron content was mapped using the band ratio derived from the ASTER VNIR processing algorithm (Cudahy, 2012; Van der Meer et al., 2014). Identification of different iron oxide minerals started by observing their spectral characteristics, and two new band ratio algorithms were derived from their spectral behaviors.

Table 4. 1: Minerals mapping algorithms developed by (Cudahy, 2012; Van der Meer et al., 2014) and new band ratios developed in this thesis. The stretch type is linear to all the band ratios.

Data	Product name	Algorithm B=band No.	Stretch limit
ASTER SWIR	Ferrous iron index in silicates/ carbonates. Minerals: actinolite and chlorite, pyroxene, olivine, ferroan dolomite To map un-weathered mafic and ultramafic rocks.	B5/B4	0.75 - 1.025
	AlOH group content (phengite, muscovite, paragonite, lepidolite, illite, montmorillonite, kaolinite, dickite)	(B5+B7)/B6	2.00 -2.25
	Kaolin group index (pyrophyllite, alunite, well-ordered kaolinite)	B6/B5	1.0 - 1.125
	FeOH group content (chlorite, epidote, jarosite, nontronite, gibbsite)	(B6+B8)/B7	2.03 - 2.25
	MgOH group content (calcite, dolomite, magnesite, chlorite, epidote, amphibole, talc, serpentine)	(B6+B9)/(B7+B8)	1.05 - 1.2
Sentinel_2 VNIR	Ferric iron content	B4/b3	1.34-178
	Goethite	(B6+B7)/(B8A+B9)	0.998-1.021
	Hematite	(b6+b9)/(b3+b8A)	1.315-1.417

4.4. The overall geological interpretation approach

The overall approach of this study is an integrated data analysis comprising remote sensing, geophysical, and field datasets. The remote sensing and geophysical data were compared to the geological map and field observation data to establish a relationship between the different datasets. Maps of mineral indices were produced from ASTER and Sentinel-2 images ([see section 4.3 for details](#)). The gamma-ray image was interpreted visually and statistically (i.e., contents of K, eTh, and eU). The aerial photograph was visually interpreted to observe the color contrasts between different lithologies. The summarized interpretation steps are explained as follows.

Training and validation areas were selected for a detailed interpretation of all the datasets, as indicated in [Figure 5.8](#), based on the following criteria.

- The major lithological units should be included
- There should be field observation data overlaying on these areas
- The strip directions are perpendicular to the stratigraphic layering.

All the datasets were interpreted in detail within the selected training and validation areas; lithological boundaries were digitized manually. The interpretation was based on the visual observation of the enhanced geophysical and remote sensing data, the mineral indices, the color contrast between different areas, and correlating these to the ground truth (i.e., geological map and field data). The remote sensing and geophysical data were classified based on the visually interpreted classes in the training area. After observing the relationship between the visually interpreted images and the classified maps, the classification was extrapolated to the whole study area. Classification accuracy was estimated based on the visual interpretation in the training and validation areas. The details of mineral and lithological interpretations are explained in the following subsections. [Figure 4.1](#) shows a summary of the interpretation approach.

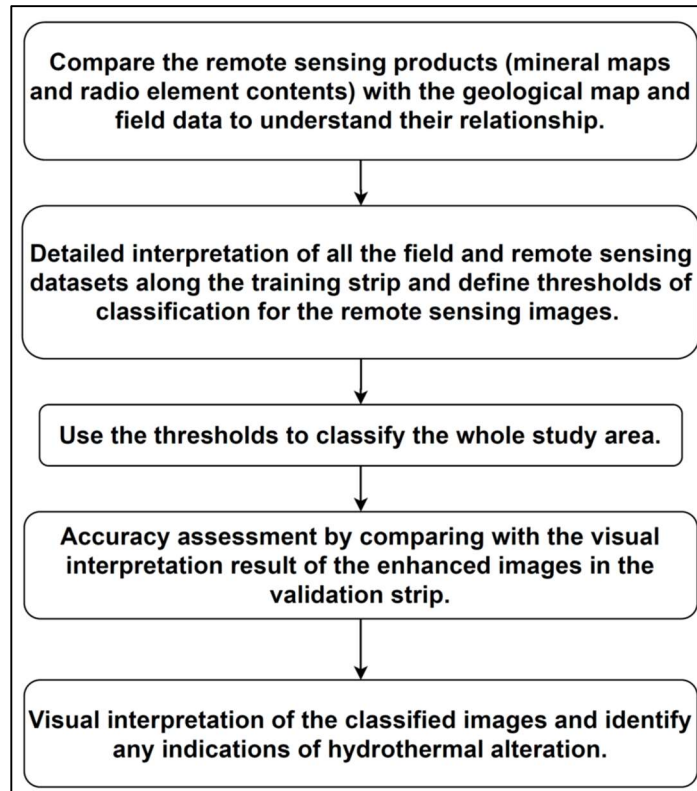


Figure 4. 1: Flow chart showing the general interpretation approach.

4.5. Lithological interpretation

A stepwise visual interpretation approach was used to identify the lithological boundaries, i.e., starting with the low spatial resolution gamma-ray data followed by relatively higher spatial resolution ASTER data, then sentinel_2, and then aerial photograph. As we go from the lower spatial resolution geophysical data to the higher spatial resolution remote sensing images, more details were added within the previously defined lithological boundaries (Section 5.4). The intension of starting from the lower resolution gamma-ray data was to preserve the clearly visible lithological boundaries in the gamma-ray image. All datasets were visually interpreted within the two selected areas for detailed interpretations (i.e., the training and validation areas) in a stepwise approach. The details about lithological interpretations are described as follows.

The broad lithological boundaries (i.e., rock units with high compositional variation) were differentiated using the gamma-ray data. Radiometric image (airborne gamma-ray data) interpretation uses to map the lithological variations based on the hypothesis that absolute and relative contents of the radioelements (K, eTh, and eU) vary considerably with lithological variation (Elawadi, Ammar, & Elsirafy, 2004). Different rock types are composed of certain amounts of rock-forming minerals that contain specific quantities of radioactive elements (Youssef & Elkhodary, 2013). The ternary image, the map of the individual radioelements, and their ratio images were used to differentiate the major lithologic groups of the training and validation areas.

Following the gamma-ray image interpretation, the ASTER image was also visually interpreted within the previously defined boundaries. Color composite of different band combinations of ASTER image, and the mineral indices produced using ASTER band ratio were used for the visual interpretation. Image enhancement methods (MNF, PCA, DCS) were also applied to the ASTER image to see better contrast.

The visual interpretation was continued using the Sentinel-2 data, and more details were added within the previously delineated lithological boundaries. Similar to the previous interpretations, the enhanced color composite image and the mineral maps of the Sentinel-2 data were used for lithological interpretations.

Finally, the high-resolution aerial photograph was visually interpreted to validate the previously interpreted boundaries and to add more details.

After all datasets were interpreted, a maximum likelihood classification method was applied in the training area to classify the images based on the visually interpreted classes step by step. The image classification was done in three successive steps as follows.

In all the classification stages, maximum likelihood classification was applied by taking representative samples from each lithologic group based on the visual interpretations (Richards & Jia, 2006). The samples were taken manually as regions of interest. The sampling system was random and as uniformly distributed as possible. Samples are considered to be representatives of the lithologic groups; hence as many samples as possible were taken from each group.

[Step 1.](#) The gamma-ray image was classified based on its visual interpretations. Representative signatures (ROI) were collected from each of the lithologic groups interpreted using the gamma-ray data. Then a maximum likelihood classification was applied to the gamma-ray image using the collected signatures in the training area.

[Step 2.](#) The 90-meter spatial resolution gamma-ray image was resampled to 30-meter and stacked with the ASTER-SWIR image. From the stacked image, regions of interest (signatures) were collected from each lithologic group based on the ASTER image interpretation. The stacked gamma-ray-ASTER image was classified using the collected signatures in the training area.

[Step 3.](#) The gamma-ray and ASTER images were resampled to 10-meter spatial resolution and stacked with the Sentinel-2 image. Signatures were collected from the stacked gamma-ray, ASTER, and Sentinel-2 image based on the lithologic units interpreted using Sentinel-2 data. Then maximum likelihood classification was applied to the stacked image using the collected signatures in the training area.

The quality of the classifications was assessed using a confusion matrix in the training area (Congalton, 1991). New signatures were collected from each image, which was used for classifications following the same strategy, as mentioned in the above paragraphs. The classified maps in the training area were compared to the visual interpretations (ROI) using a confusion matrix.

The signatures (ROI) collected from the training area were used to classify the validation area. The purpose of the validation area was to see the similarity/difference in spectral/radiometric characteristics of the stratigraphic units throughout the study area. Regions of interest were also collected from the validation area, which was used for accuracy assessment. The accuracy estimations of the validation area were made by comparing the classified maps to the visual interpretations (ROI).

After all, the classifications were extrapolated to the whole study area. The signatures collected from the training area were used to classify the whole study area following the same steps of classification. The interpretation steps are summarized in [Figure 4.2](#).

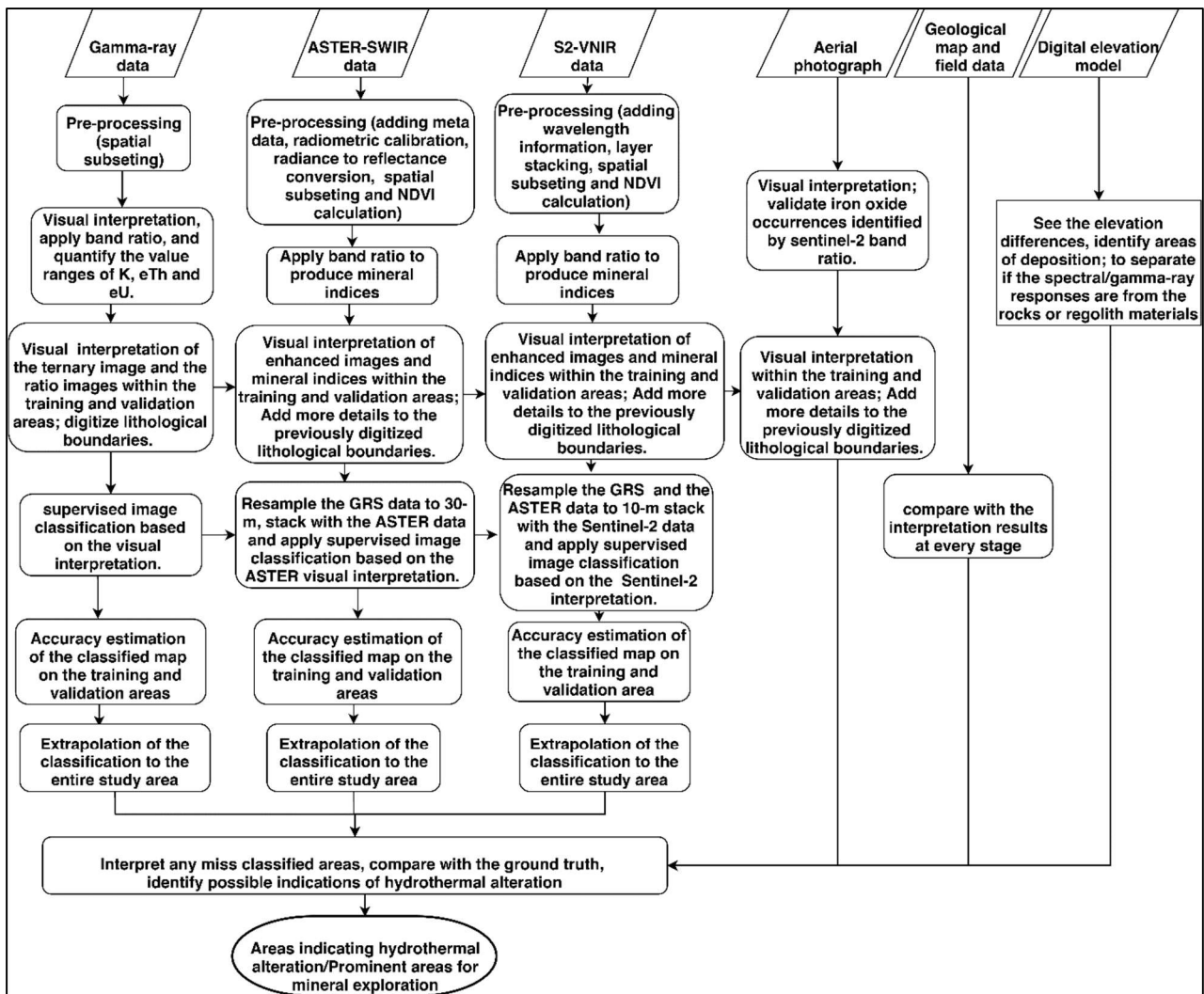


Figure 4. 2: summarized flow chart showing the interpretation steps.

4.6. Indicators of hydrothermal alteration

Visual interpretation of the classified maps leads to the identification of possible discrepancies within a geological unit. The misclassified areas were interpreted in detail to see the possible reasons for disruption. The importance of this detailed interpretation is to see if there are any indications of hydrothermal processes.

5. RESULTS

This section presents the interpretation, classification, and comparison results of all the data sets that started from pre-processing, band ratios, visual interpretations, and image classifications.

5.1. Pre-processing

Results of spatial sub-setting of all datasets provide a spatial extent of the study area that is approximately 400 km².

5.2. Vegetation cover analysis

The NDVI results of the ASTER and Sentinel-2 images are attached as [Appendices 3 and 4](#), respectively. There was no much vegetation during the ASTER image acquisition time. However, the Sentinel-2 NDVI indicates the presence of vegetation cover following streamlines on the study area. Sentinel-2 NDVI map shows higher values(0.23-0.73). Therefore all the values above 0.23 were masked out from the Sentinel-2 image. However, the ASTER NDVI values were low (0-0.36), so there is no need for vegetation masking. In fact, the value 0.36 is high, but it only occurs in a single streamline ([see Appendix 3](#)). It was better not to apply masking in this data because masking can result in losing information.

5.3. Mineral indices

The aster and sentinel-2 band ratio results are explained in the following sub-sections. Spectral endmembers of the ASTER and Sentinel-2 images were extracted automatically (i.e., using SMACC) and manually. A Sequential Maximum Angle Convex Cone (SMACC) extracts endmembers using a convex cone model. It uses extreme points to determine a convex cone. It finds the brightest pixel; then it finds the most different pixel from the first one, and then finds the most different pixel from the first two pixels, and so on (Harris Geospatial Solutions, 2020). The mineral indices were confirmed using these spectral plots (signatures) by comparing them to the USGS spectral libraries (Kokaly et al., 2017). The high spatial resolution aerial photograph was also very helpful in identifying iron oxide rich areas by showing dark brown features. Thresholds of sentinel_2 band ratios were specified by comparing with the aerial photograph and identifying the real iron oxide rich areas.

5.3.1. Ferrous iron content in carbonates/silicates

The ASTER band ratio (b5/b6) is used to map mineral groups containing ferrous iron associated with silicates/carbonates. These mineral assemblages are indicators of well-exposed fresh (non-oxidized) outcrops, especially mafic and ultramafic rocks rich in ferrous silicates and ferrous carbonates. The result of this ratio shows warm colors on the ultramafic/mafic rocks and iron formations. These units include intrusive dolerite/gabbro, extrusive komatiites, and basalts of different compositional variations, as described in the geological map and field data. The felsic volcanics and volcano-sedimentary rocks show dark colors indicating the non-existence of ferrous iron group minerals. Some minerals of this group are actinolite, chlorite, olivine, pyroxene, and dolomite, as explained by (Cudahy 2012). The resulted spectral signatures show the occurrence of these mineral groups in the Talga Talga, Salgash, Dalton suite, Gorge Creek, and Fortescue group stratigraphic units. The north-western part of the Duffer formation also shows relatively higher content of ferrous iron mineral groups, although the units are felsic volcanics and volcanoclastic sediments as described by the geological map. The occurrence of these minerals in the north-western Duffer formation can result from the intercalated dolerite/gabbro sills/dykes as mentioned in the field observation data. The spectral plots of this mineral index are displayed in [Figure 5.1](#). The resulted ratio map is attached as [Appendix 5](#).

5.3.2. Iron hydroxyl (FeOH) group content

ASTER band ratio $((B6+B8)/B7)$ is used to map weathered and hydrothermally altered -OH bearing mafic and ultramafic rocks. The typical minerals which can be identified using this ratio are chlorite (i.e., porphyritic alteration), epidote (i.e., calc-silicate alteration), and nontronite, as explained by (Cudahy, 2012). Iron formations, mafic, and ultramafic rocks show cool colors, which implies low content of FeOH group content mineral groups. The felsic volcanics and volcanoclastic sedimentary rocks of the Duffer and Wyman formations, as well as the Croydon group sandstone, show dark colors indicating the non-appearance of these mineral groups. The resulted spectral plot is illustrated in [Figure 5.1](#). The aluminum hydroxyl group mineral index map is attached as [Appendix 6](#).

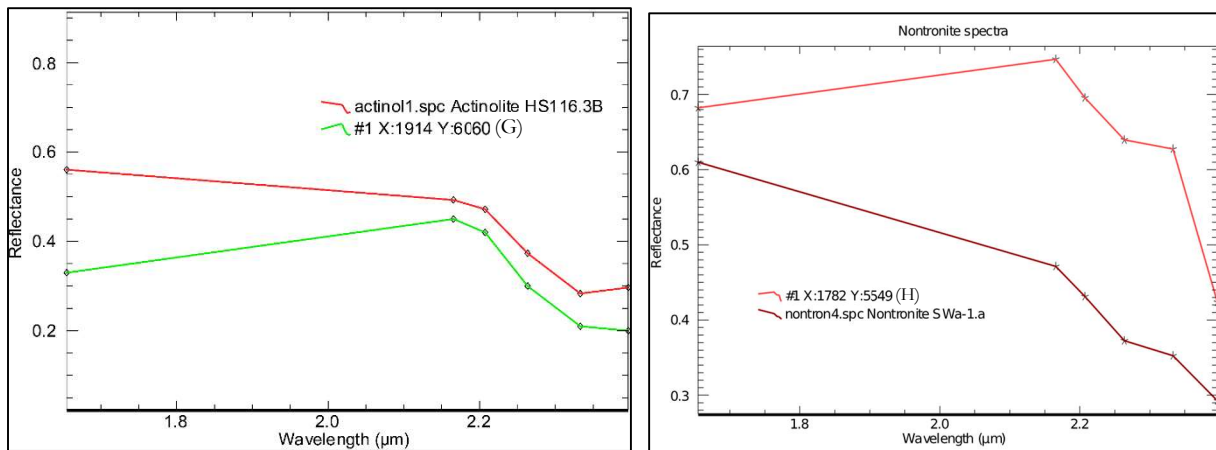


Figure 5. 1: Spectral plots of ASTER mineral indices compared to USGS spectral libraries, ferrous iron group (right-hand side), iron hydroxyl group (left-hand side). The letters indicate the pixel positions from where the spectra were extracted, and they are showing in figure 5.2.

5.3.3. Aluminum hydroxyl (AlOH) group content

The ASTER band ratio $((B5+B7)/B6)$ is used to map clay-rich stratigraphic horizons. Clay minerals have a strong absorption feature around 2.2 μm due to the Al-OH bond. The result of this ratio shows higher signals along with the central and south-eastern parts of the study area (i.e., the Duffer and the Wyman formations; [see Figure 5.3](#)). According to the field data and the geological map, these lithologic units are felsic volcanic rocks and volcanoclastic sandstones. Dacitic volcanic breccia, sandstone, tuff, quartz-mica-schist, porphyritic rhyolite, and rhyodacite rocks are some of the units showing a high content of AlOH group minerals. The mafic and ultramafic rocks appeared as dark features in this band ratio result. The lithology described as Lalla Rookh sandstone in the geological map also shows cool colors, which is the implication of minor AlOH group contents. Some of the AlOH group minerals are kaolinite/dickite, illite, montmorillonite, muscovite, and paragonite (Cudahy, 2012).

These minerals can be either primary constituents of felsic rocks or resulted from hydrothermal alteration processes. In geological studies, these minerals are usually indicators of hydrothermal alteration processes and provide a clue for further investigations. The endmember spectra collected from these lithologies are displayed in the following [Figure 5.2](#). The AlOH mineral group index map is attached as [Appendix 7](#).

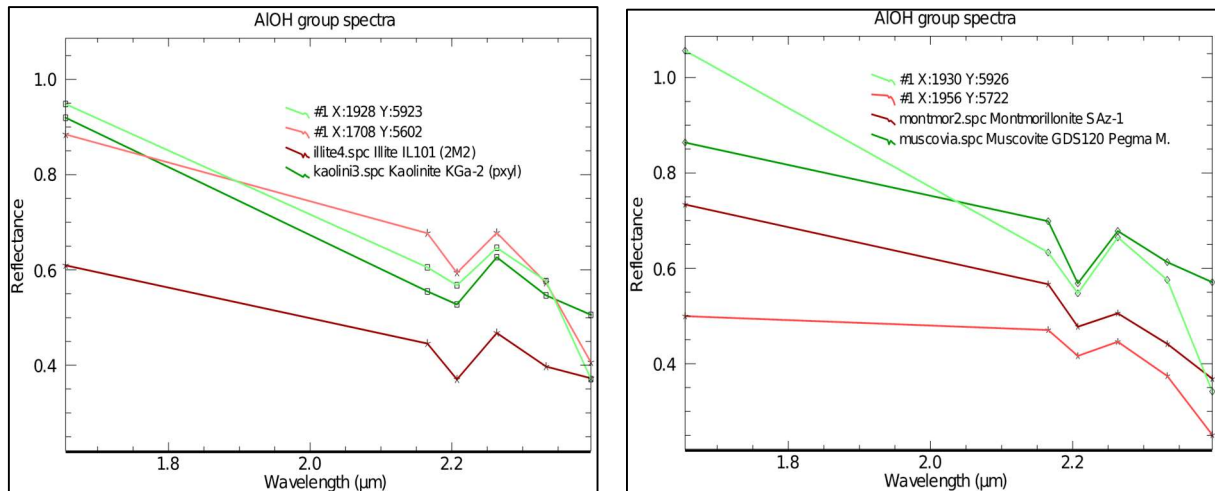


Figure 5. 2: Spectra of AIOH group minerals extracted from the ASTER image compared to USGS spectral library plots. The pixel locations represented by the letters in these spectra are displayed in figure 5.3.

5.3.4. Kaolin group index

Kaolin group index (ASTER B6/B5) is used to map different clay-rich stratigraphic horizons, and rock units that are overprinted by hydrothermal alteration. The result of this band ratio shows warm colors in the north-central part of the study area, including the Salgash subgroup, Wyman formation, and Fortescue group. This mineral index shows a specific pattern, and its spectral signature resembles pyrophyllite mineral. Pyrophyllite mineral was grouped with kaolin group minerals by Cudahy, (2012) due to its spectral characteristics even though geologically, it is not a member of kaolin group minerals. Pyrophyllite mineral can be formed by the following processes as explained by (Pirajno, 2010).

- Hydrothermal alteration of paragonite where Na is replaced by hydrogen
- Hydrothermal alteration of K-mica where K is replaced by SiO₂
- Transformation of kyanite into pyrophyllite through retrograde metamorphism at high temperature

The rocks showing high values of this ratio are quartz sandstone, volcanoclastic sandstone, massive komatiite basalt, porphyritic rhyolite, rhyodacite, and local felsic volcanoclastic rocks only in one specific area as showing in [Figure 5.3](#) above. The felsic volcanic rocks and volcanoclastic sediments along the central part of the study area (i.e., Duffer formation) show dark colors. The mafic rocks metabasalt and meta dolerites also show cool colors ([see Appendix 8](#)). The spectral features of the mafic and ultramafic rocks showing the kaolin group index contain an additional absorption feature at 2.2635 µm, which resembles nontronite spectra ([see Figure 5.4](#)).

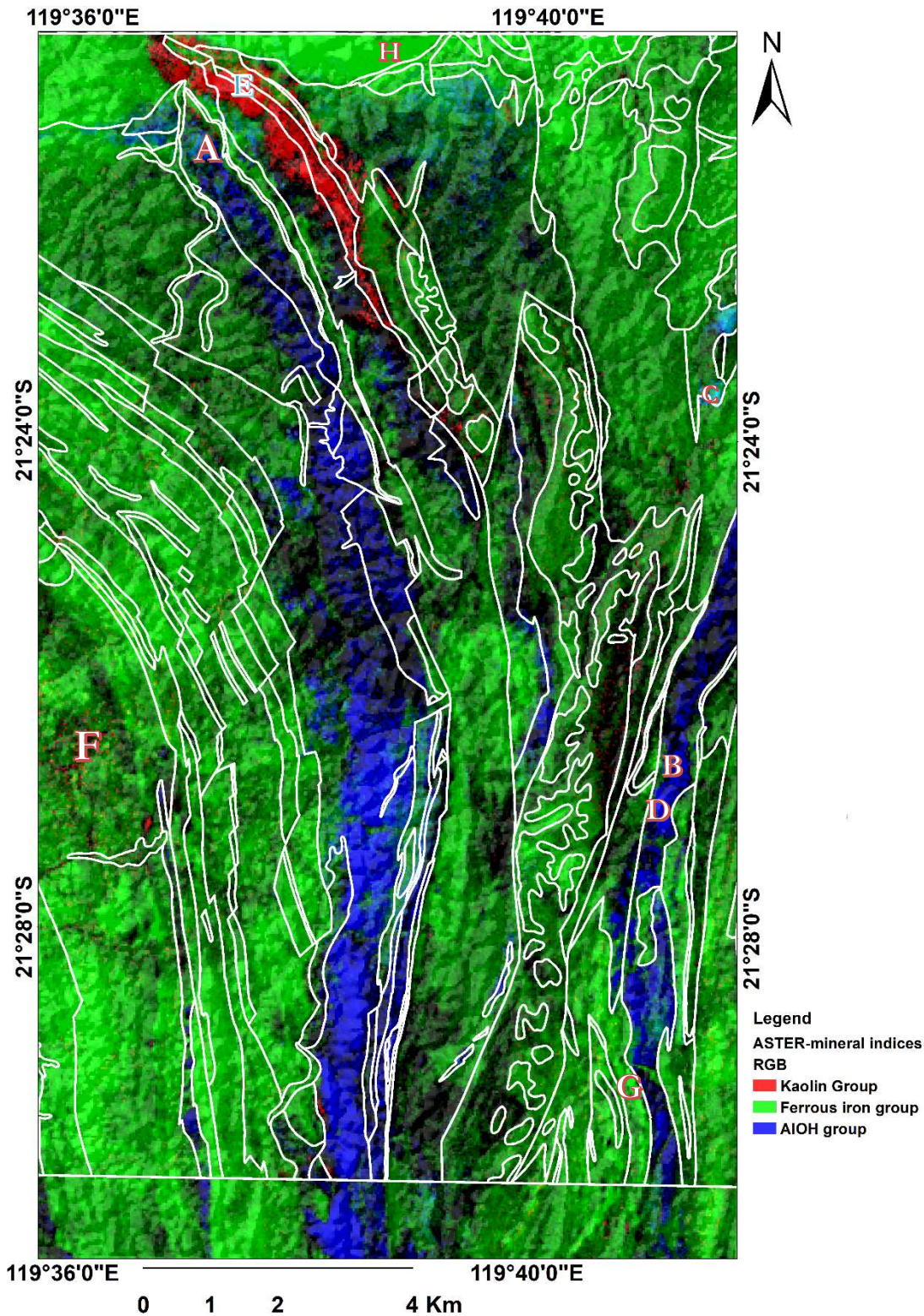


Figure 5. 3: A color composite map of three mineral group indices. Kaolin group index (red), ferrous iron group index (green), and aluminum hydroxyl group index (blue). The white lines come from the geological map. The overlying letters represent pixel positions from which the spectral plots were extracted. The individual mineral group index maps are attached as appendices.

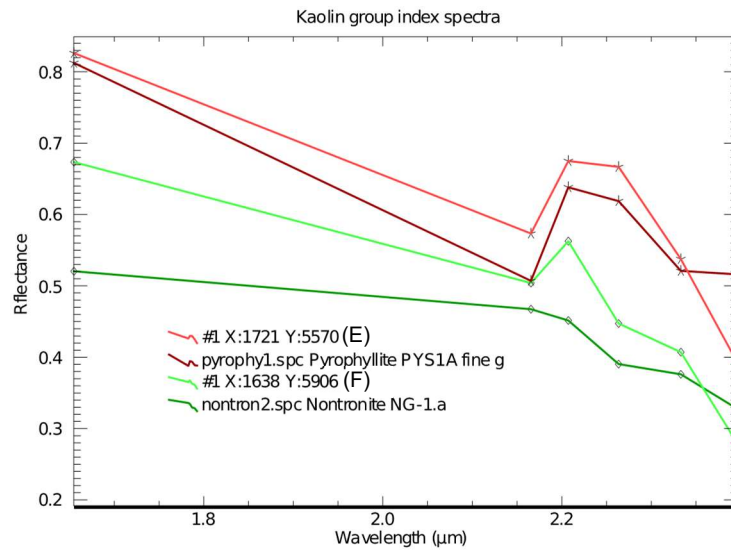


Figure 5. 4: ASTER spectra of the kaolin group index compared to the USGS spectral library. The mineral spectra indicated in reddish colors have absorption features at 2.2 μm , which resembles pyrophyllite mineral spectra. The spectra represented by greenish color shows an additional absorption feature at 2.26 μm , which resembles a nontronite feature. The letters are representing the pixel locations from where the spectral plots were extracted. These pixel locations are showing in figure 5.3.

5.3.5. Magnesium hydroxyl (MgOH) group content

This ASTER band ratio $((B6+B9)/(B7+B8))$ is used to map hydrated ferromagnesian rocks rich in OH-bearing tri-octahedral silicates like actinolite, serpentine, chlorite, talc, and carbonates (Cudahy, 2012). The result of this band ratio indicates the occurrence of these mineral groups in very limited parts of the study area, especially the Shay intrusion and the Talga Talga subgroup. But spectra of carbonate rocks were not detected even though carbonates are expected in the study area. The rock units showing the indication of MgOH group minerals are described as serpentine, schistose, chlorite-schist, meta_peridotite, basalt, and gabbro, according to the geological map and the field data. Spectral plots and a map showing the MgOH mineral group index are illustrated in [Figure 5.5](#) and [Appendix 9](#), respectively

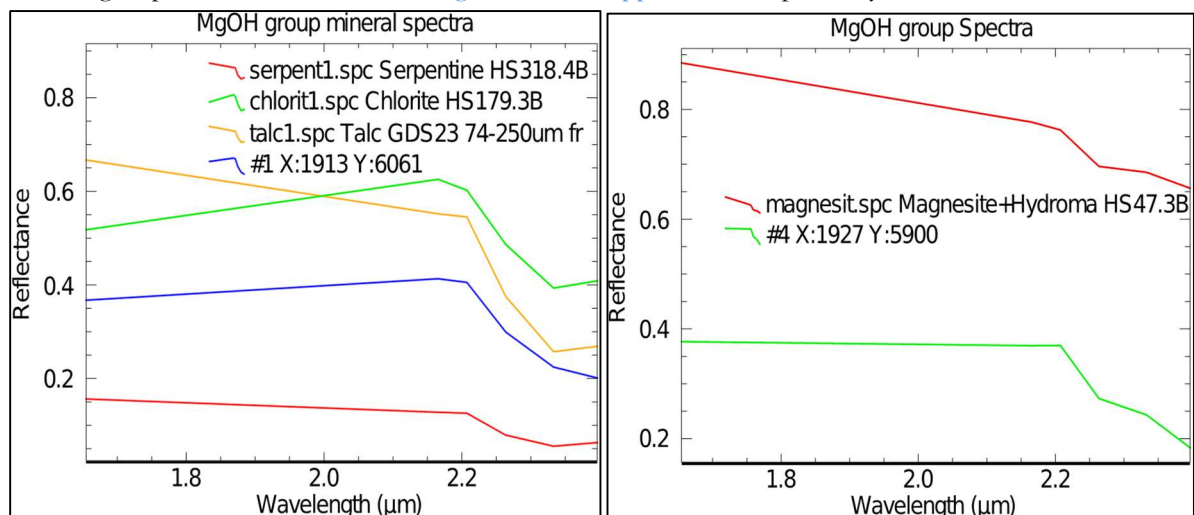


Figure 5. 5: MgOH group minerals spectra collected from ASTER image compared to USGS spectral library.

5.3.6. Iron oxides

The high-resolution sentinel-2 VNIR image was used to map iron oxide minerals. Iron oxides can appear in different ways (i.e., as main constituents of a rock or as coatings). In the case of this study area, the iron formations, gossans as well as red sandstone can contain iron oxide minerals as primary constituents. The

band ratio result of (b4/b3), which represents all iron oxide minerals, indicates warm colors everywhere throughout the study area [Figure 5.6](#). This result reveals the presence of iron oxides throughout the study area, either as coatings or deposited soils in addition to the naturally iron-bearing rocks

5.3.6.1. B4/B3 (Ferric iron content)

The occurrence of ferric iron content was mapped using the sentinel_2 band ratio (b4/ b3) derived from ASTER band ratio algorithms (Van der Meer et al., 2014). The ratio of the high-resolution image was helpful in identifying the spectral response of gossans in combination with the aerial photograph. Otherwise, gossans are not large enough to be mapped using lower resolution images. They have a spatial extent as small as two pixels in a 10 m spatial resolution image. In the aerial photograph, gossans appear as dome-like structures, and they are topographically high against the background lithology due to their resistance to weathering. Their resistance to weathering has resulted from their association with quartz veins. The resulted mineral map of this ratio is illustrated in [Figure 5.6](#) below.

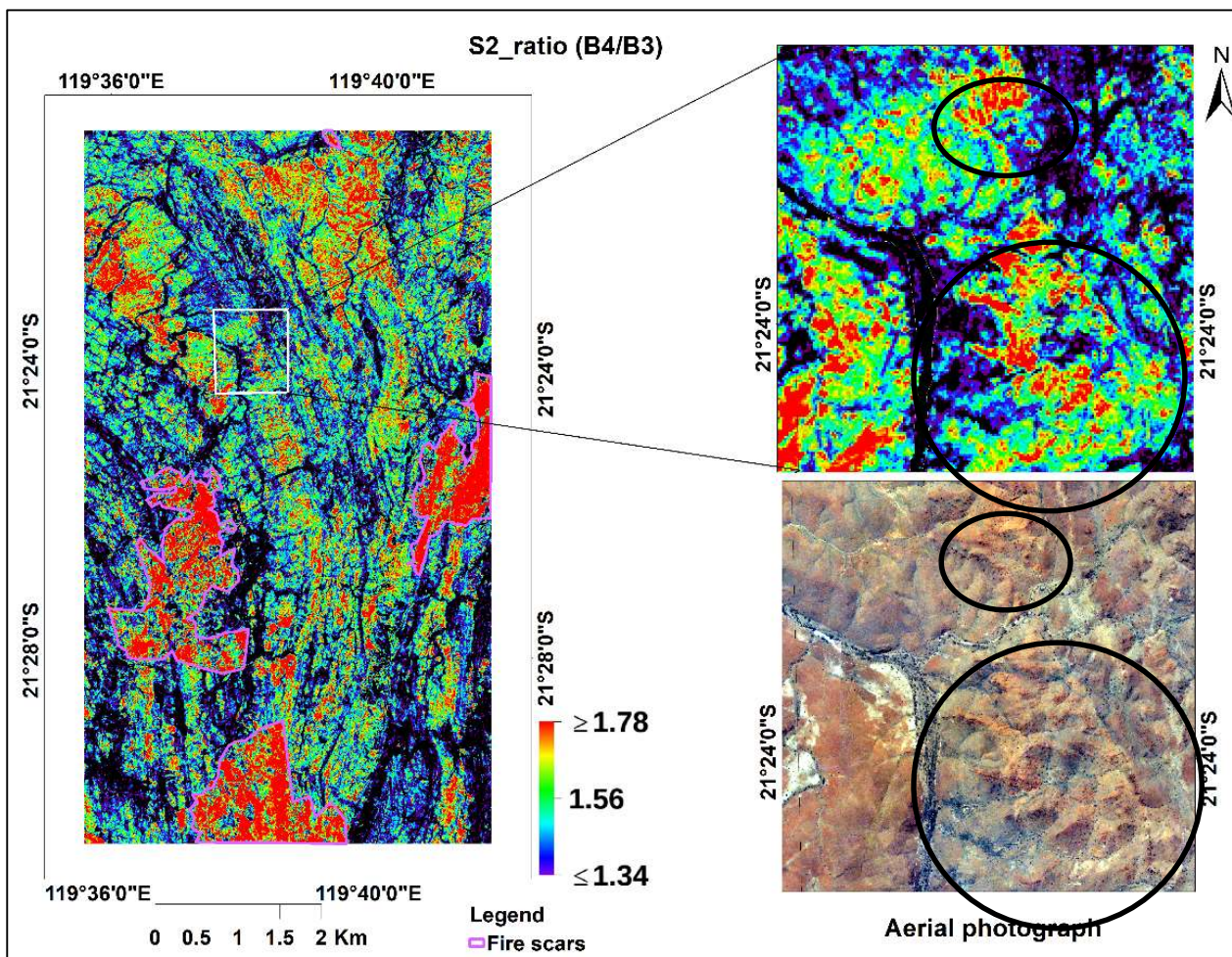


Figure 5. 6: Sentinel-2 band ratio (b4/b3) showing ferric iron content and comparison with the aerial photograph. The large scale maps displayed on the right side of this figure indicated by the circles shows lithological patterns enriched in iron oxide minerals in sentinel-2 band ratio and the aerial photograph. The aerial photograph was used as a validation data for the sentinel-2 band ratio results, and the stretch limits displayed on the color ramp were specified based on the aerial photograph.

5.3.6.2. Identifying different iron oxide minerals

The endmember spectra of the sentinel-2 image indicate the occurrence of two iron oxide species (i.e., hematite and goethite). Spectra of these minerals were visually interpreted to differentiate their occurrence in the study area. The deepest absorption features and the picks of the spectra were carefully inspected to see the difference in spectral characteristics. The deepest absorption feature of goethite is at 0.945 μm with

a peak at 0.740 μm . On the other hand, hematite has a deepest absorption feature at 0.865 μm with peaks at 0.740 and 0.945 μm . Additionally, band 3 (0.560 μm) is a peak for goethite and an absorption feature for hematite. New band ratio algorithms were developed to separate hematite and goethite minerals by considering the above criteria. Hematite band ratio is $(b_6+b_9)/(b_3+b_8A)$ with stretch limits 1.315-1.417 and that of goethite is $(B_6+B_7)/(B_8A+B_9)$ with stretch limits 0.998-1.021. The stretch limits were specified by carefully inspecting the spectra of the band ratio results. The spectral plots are illustrated in [Figures 5.7](#) below. The ratio images of hematite and goethite are attached as [Appendices 10 and 11](#), respectively.

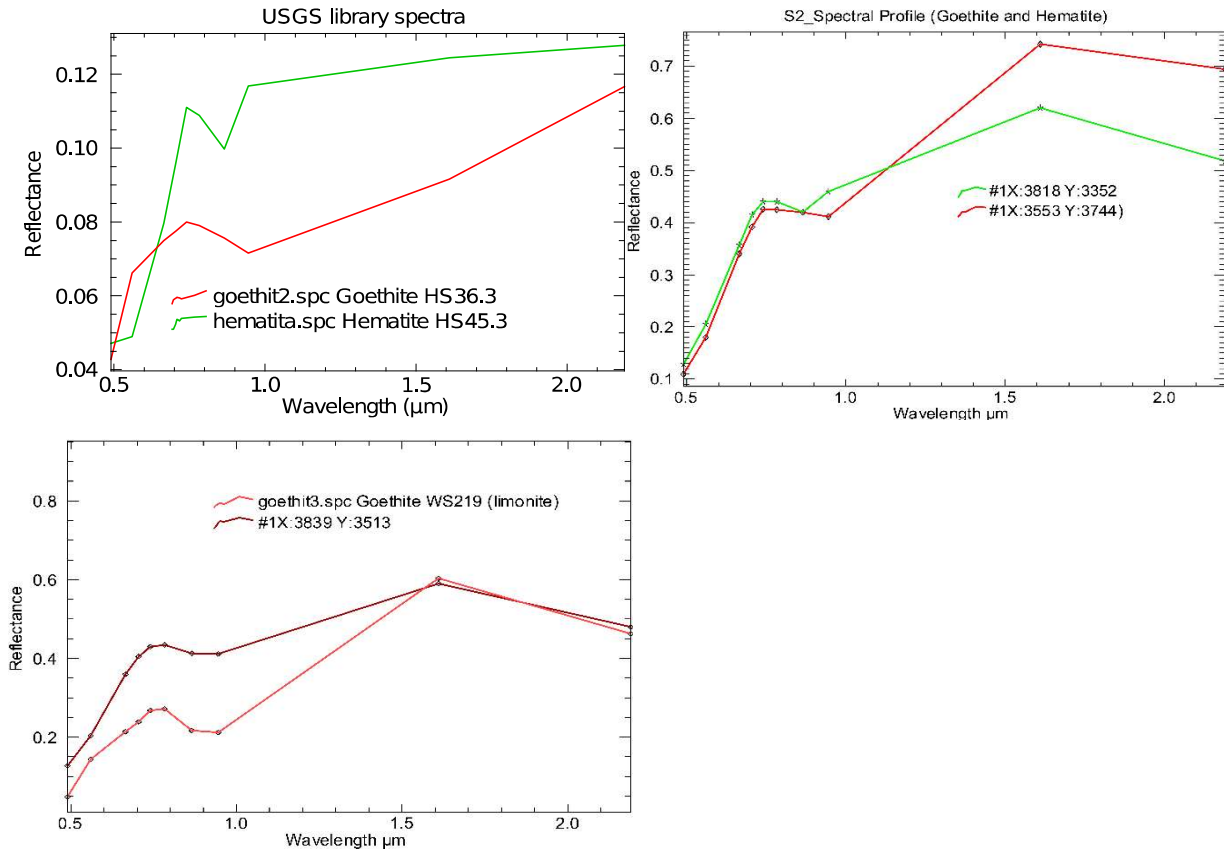


Figure 5. 7: Sentinel_2 spectral plots of goethite and hematite minerals.

Goethite and hematite spectra resampled from USGS spectral library(top right); goethite and hematite spectra extracted from the image (top left); goethite spectra resampled from USGS library and collected from the image (lower left).

The banded iron formation and sandstone units (i.e., Cleaverville formation and Lalla Rookh sandstone) show goethite mineral occurrences, as showing in appendix 12. Iron oxides are constituents of iron-bearing rocks, including iron formations. Iron oxides can occur as cementing materials in sandstone, which usually give reddish colors to the rock. The Lalla Rookh sandstone also shows reddish color in the aerial photograph. Most parts of the study area show hematite mineral occurrences except the mafic and ultramafic rocks in the western part of the study area ([see Appendix 11](#)). The rock units banded iron formation (the Cleaverville formation), sandstone, rhyodacite, rhyolite, quartz, and volcanoclastic sandstone (the Duffer formation) show strong signals of hematite mineral. The Duffer formation is rich in gossans, which makes the result of this band ratio reasonable. In some lithologies, the occurrence of hematite can be only as a coating material and not as a mineral constituent of the lithology.

5.4. Lithological interpretations

Lithological interpretations were made on two parts of the study area as training and validation areas, as showing in [Figure 5.8](#). The strip indicated in the northern part of the study area is a training area, and the

one in the southern part of the study area is used as a validation area. The interpretations were extrapolated to the whole study area using image classifications after all the datasets were interpreted step by step.

5.4.1. Stepwise interpretation within the training and validation areas

The results of this interpretation are explained in the following figures and tables. The codes represent the type of dataset from which the lithologic boundaries were defined. G represents Gamma-ray, A is ASTER, S is Sentinel_2, and P is an aerial photograph. Gi is a lithologic unit defined using the gamma-ray data. GiAj represents a lithologic unit identified using ASTER image within the previously defined boundary from gamma-ray data. The representation continues in the same way as more details added to the already defined boundaries as GiAjSi and GiAjSiPj and so on. This coding system helps to indicate the parent units of the detailed boundaries. Figure 5.8 shows the visual interpretation result of gamma-ray data within the training and validation areas. The interpretation is based on the ternary image, the ratio of the radioelements, the individual contents of the radioelements, and the total count. The gamma-ray data was able to differentiate lithologic groups of high compositional differences as mafic, felsic, sedimentary rocks, and altered/metamorphosed intrusives.

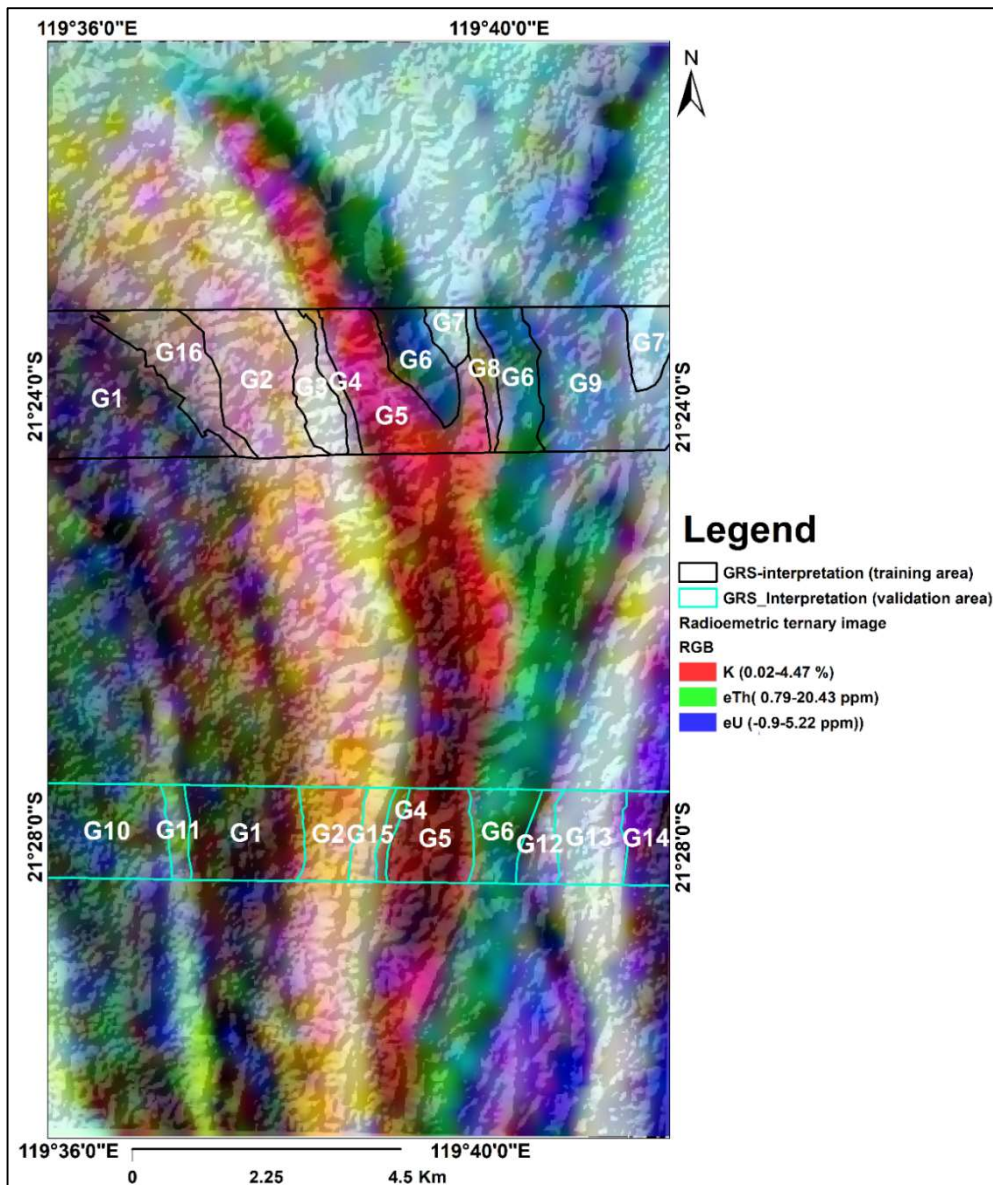


Figure 5. 8: Visual interpretation of gamma-ray data along with the two stripes as training and validation areas. The polygons indicate the major lithological boundaries based on the variation in radioelements abundance. The lithological units represented by the codes are explained in Table 5.1.

Table 5. 1: lithological interpretation results of the training and validation strips using gamma-ray data. Lithologies with similar radioactivity responses in the training and validation strips are represented by the same code. The interpretation was made using the ternary image, the abundance of the individual radioelements, and their ratio images.

Code	K%	eTh (ppm)	eU (ppm)	TC (ppm)	Field data	Geological map	Description
G1	0.2_0.55	1.6_3.4	0.4_1.1	13_23	Basalt, dolerite-gabbro, komatiite	Komatiite basalt, talc-carbonate- chlorite-serpentine	Low radioelement contents
G2	1.2_3.2	4.5_8.5	0.6_2.4	45_80	Basalt, dolerite-gabbro, sandstone, gritstone, rhyolite, dacite, conglomerate	Felsic volcanic sandstone, dacite, dacitic volcanic breccia, porphyritic dacite breccia in a dacite matrix, tuff, wacke, conglomerate	This unit shows a high content of radioelements with relatively elevated potassium. The range of values matches the granitoids group.
G3	2.01_3.2	7.5_14.3	2.0_2.7	70_100	Sandstone, conglomerate, gritstone, andesite, chert	Rhyolitic tuffaceous volcanic sandstone, ash beds, quartz-porphyritic rhyolite, dacitic volcanic breccia	This area appears as a bright feature in the ternary image due to the higher content of all the three radioelements. These values are within the range of quartz-feldspar porphyry lithologic units.
G4	1.2_2.4	4.0_8	1.2_2.2	45_70	Andesite, chert	Komatiite basalt with pyroxene, local talc carbonate rock, chert	High radioelement contents which are unexpected in komatiite basalt.
G5	0.8_2.6	1.5_4.5	0_1.4	25_55	Andesite, exhalate, chert, basalt, sandstone/siltstone, tuff, conglomerate	Komatiite basalt, massive and pillowed lavas, and subvolcanic intrusions, local pyroxene, rhyolite and, rhyodacite BIF and felsic volcanic sandstone.	The ternary image appears as a reddish color showing selective enrichment of potassium.
G6	0.1_0.7	2.5_5.0	0.2_1.8	14_34	Chert, gabbro, BIF_jaspilite, sandstone/siltstone	Ferruginous duricrust, ferricrete, BIF, ferruginous chert, quartz-magnetite-grunerite rock, sandstone, porphyritic rhyolite rhyodacite, conglomerate	It has low radioelement contents and relatively higher thorium content.
G7	0.6_2.0	5.0_13.0	1.0_4.5	35_95	Gritstone, sandstone	Sandstone, colluvial sand, gravel, silt, ferruginous duricrust, conglomerate, shale	High radioelement contents relatively higher thorium and uranium
G8	0.8_1.6	3.0_7.0	0.2_2.0	28_46	No field data	Felsic volcanic sandstone, tuffaceous, local quartz sandstone	

G9	0.3_1.2	3.5_8.0	1.0_3.0	25_55	MT ROE basalt	Massive porphyritic vesicular and amygdaloidal basalt, some pillow basalt	Low radioelement contents, relatively lower potassium content
G10	0.15_0.5	2.2_4.6	-0.2_1.6	11_24	Basalt, quartz vein, chlorite, schist, pyroxenite wall rock	Metabasalt and metadolerite amphibolite and amphibolite schist	Generally, it has low radioelement contents. It shows greenish color due to relative increment in thorium content.
G11	0.35_0.6 5	3_6	0.2_1.6	14_24	Quartz-chlorite-carbonate schist, U/M dike	Schistose, metamonzogranite, talc-carbonate and chlorite serpentine-carbonate schist, metamorphosed ultramafic volcanic rocks	A thin north-south trending unit which has relatively higher radioelements
G12	0.4_1.8	2.5_8.5	0.6_2.2	20_55	Carbonate, chert, greywacke, schist	Serpentine, schistose, metaperidotite, and serpentine-chlorite schist	Relatively uranium enriched lithology
G13	1_2.8	3_12	1.6_4.4	30_80	No field data	Metaperidotite and serpentine-chlorite schist, porphyritic rhyolite, and rhyodacite, local felsic volcanic rocks, colluvial sand silt, and gravel.	The unit appears as a bright feature in a ternary image due to the higher content of all the three radioelements.
G14	0.2_0.8	1.2_3	0_2.2	12_30	Fuchsitic chert, chlorite-quartz schist,	Pelitic schist, shale and siltstone, carbonate-altered and silicified, massive basalt, komatiite basalt, massive and pillowed lavas and subvolcanic intrusions, local pyroxene.	It shows blue color in the ternary image due to the relative enrichment of uranium compared to the other radioelements.
G15	1.5_4	5_8.5	0.6_1.1	40_85	Sandstone, chert	Quartz-porphyritic rhyolite, locally schistose, felsic volcanic sandstone, local chert, wacke, conglomerate, shale, tuffaceous sandstone, and iron formations	It has a relatively higher content of radioelements compared to the surrounding rocks.
G16	0.4_1.8	3.0_6.0	0.7_1.6	20_55	Dolerite/gabbro, tonalite, basalt, volcanoclastic	felsic volcanic sandstone, dolerite/gabbro, wacke, conglomerate, dacitic volcanic breccia, tuff	

Visual interpretation results of the ASTER data within the training and validation areas are showing in [Figure 5.9](#). The interpretation was based on color contrast of different band combinations and relative abundance of the mineral groups. The descriptions of the lithologic units are in [Table 5.2](#).

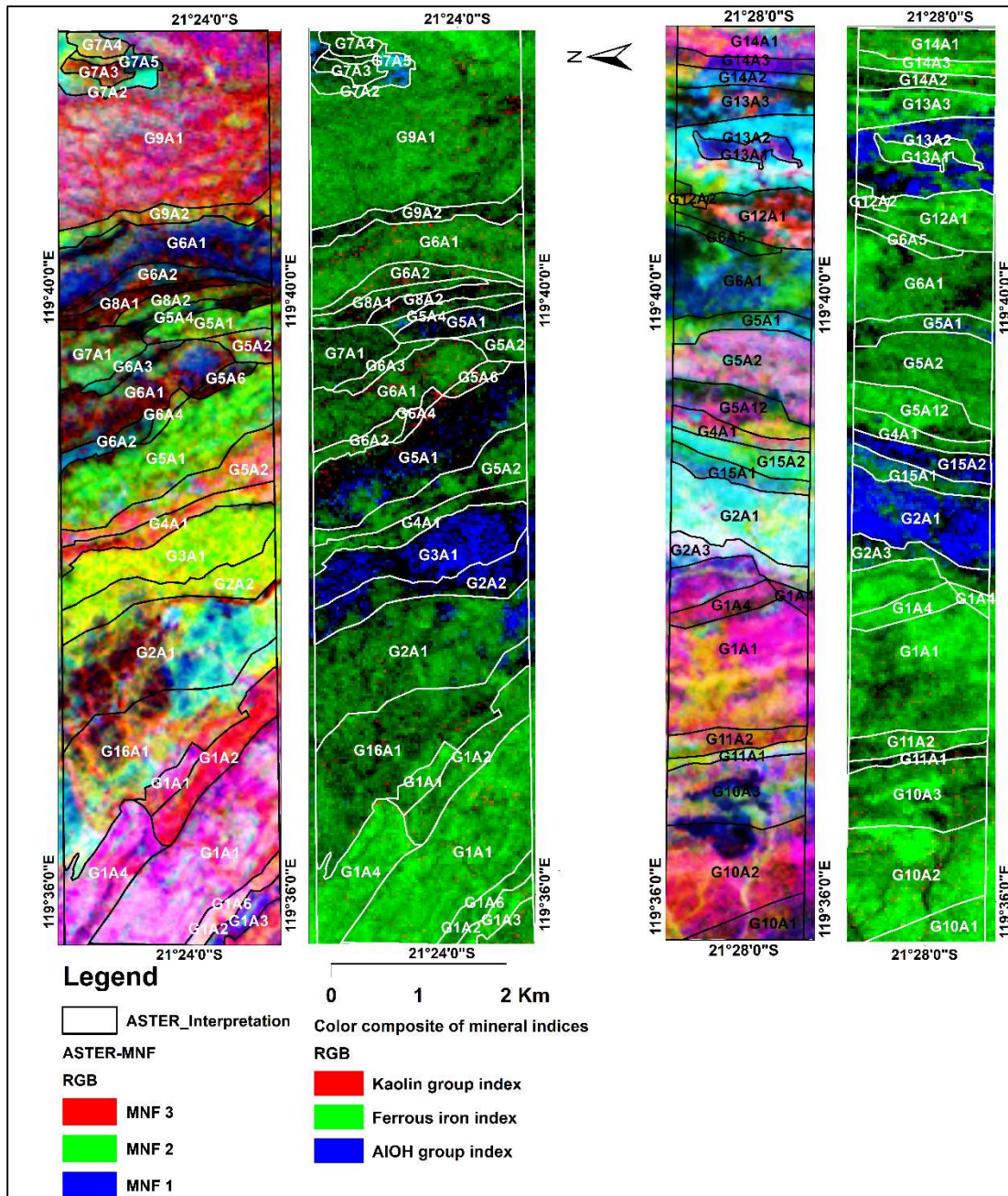


Figure 5. 9: A visual interpretation of ASTER enhanced images and mineral occurrence maps within the predefined boundaries using the gamma-ray data. The first two maps on the left side represent the training stripe, and the last two maps on the right side represent the validation stripe. The codes are explained in the following table (table 5.2).

Table 5. 2: Lithological interpretation of the training and validation strips using ASTER-SWIR data within the previously defined boundaries from gamma-ray data. The analysis was done by visual interpretation of enhanced band combinations and the occurrence of mineral groups produced from ASTER band ratio images. The code Gi represents the lithological group defined by the gamma-ray data, and Ai represents a unit defined using ASTER within the pre-defined unit Gi.

code	Mineral occurrence	Field data	Geological map	Description
G1A1	Ferrous iron, minor contents of kaolin group and FeOH	Basalt,	Komatiite basalt, massive and pillowed lavas, local pyroxene	The minerals occurrence and the field data confirms the geological map.
G1A2	Ferrous iron, FeOH and MgOH	Gabbro, chert,	Komatiite with pyroxene, local talc-carbonate rock, pillowed and variolitic, komatiite basalt	MgOH group minerals appear in limited areas in this study area. These minerals can be indicators of talc-carbonate rocks.
G1A3	Ferrous iron, minor contents of kaolin group and FeOH	Tonalite	Pillowed and variolitic komatiite basalt	The enhanced image shows a unique color in this unit. However, the mineral occurrences are the same as the background lithology.
G1A4	Ferrous iron, FeOH, and MgOH	No field data	Komatiite with pyroxene, local talc-carbonate rock	This unit shows similar spectral characteristics with unit G1A1. The partial enrichment in the FeOH mineral group makes it different.
G1A6	Ferrous iron, minor contents of FeOH group	No field data	Dolerite and local gabbro	This unit shows a similar mineral occurrence as G1A1. However, the enhanced image has a different color.
G16A1	Minor proportions of ferrous iron, kaolin group, and FeOH	Dolerite/gabbro, tonalite, basalt, volcanoclastic	Felsic volcanic sandstone, dolerite/gabbro, wacke, conglomerate, dacitic volcanic breccia, tuff	The relatively lower content of ferrous iron compared to the mafic and ultramafic rocks.
G2A1	Ferrous iron, minor contents of kaolin and FeOH group minerals	Basalt, gritstone, rhyodacite, conglomerate	Local volcanoclastic sandstone, dacite, dacitic volcanic breccia, porphyritic dacite breccia in a dacite matrix, tuff, conglomerate	G16A1 and G2A1 units show similar mineral distributions.
G2A2	AlOH group minerals, and minor ferrous iron content	Agglomerate, dacite, sandstone	Local volcanoclastic sandstone, dacite, dacitic volcanic breccia, tuff, conglomerate, quartz-porphyrific rhyolite; locally schistose	This unit is a transition between the rocks of intermediate and felsic compositions. So the ferrous iron group and AlOH group minerals occur together.

G3A1	High AlOH group content	Sandstone/gritstone, conglomerate, andesite, chert	Rhyolitic tuffaceous volcanic sandstone, ash beds, quartz-porphyritic rhyolite, dacitic volcanic breccia	Only AlOH mineral groups occur in this unit. All the other ASTER band ratio results show dark features in this unit.
G4A1	Ferrous iron and minor FeOH group minerals	Andesite, chert	Komatiite basalt with pyroxene, local talc carbonate rock, chert	The abundance of ferrous iron group minerals in komatiite basalt is geologically reasonable.
G5A1	Sparsely distributed AlOH and kaolin group mineral occurrences	Exhalite, basalt, tuff, chert, conglomerate sandstone/siltstone,	Felsic volcanic sandstone, tuffaceous, local quartz sandstone, porphyritic rhyolite, and rhyodacite	In the geological map, G5A1 and G5A2 units were interpreted as one unit and described as komatiite basalt. However, the ASTER image interpretation shows that these units are different. G5A1 has a felsic composition, but G5A2 shows mafic composition according to the mineral occurrences.
G5A2	Ferrous iron and minor FeOH group minerals	Basalt, exhalite, andesite	Komatiite basalt, massive and pillowed lavas and subvolcanic intrusions, local pyroxene	
G5A4	Minor ferrous iron group minerals	-	Felsic volcanic sandstone, tuffaceous, local quartz sandstone	The spectral characteristics of this unit don't show any felsic composition. Hence the geological map and the mineral distribution do not match.
G5A6	Ferrous iron, minor FeOH, and kaolin group minerals	-	Ferruginous duricrust, ferricrete, BIF, ferruginous chert, quartz-magnetite-grunerite rock.	The geological map interpreted this unit together with G6A1, and it also has similar spectral characteristics. But it was separated due to its radioelement contents.
G6A1	Ferrous iron, minor FeOH, and kaolin group minerals	BIF-jaspilite, gabbro	Ferruginous duricrust, ferricrete, BIF, ferruginous chert, quartz-magnetite-grunerite	It is reasonable for BIF to contain ferrous iron group minerals.
G6A2	Ferrous iron, minor FeOH, and kaolin group minerals		Felsic volcanic sandstone, tuffaceous, local quartz sandstone	The enrichment of ferrous iron mineral groups is unexpected in felsic rocks.
G6A3	Ferrous iron, minor FeOH, and kaolin group minerals	BIF-jaspilite	Sandstone with beds of conglomerate minor siltstone and shale	The geological map has grouped this unit with G7A1. But its radioelement content and mineral distribution show a partial difference.
G6A4	Sparsely distributed FeOH and kaolin group mineral occurrences	Chert, BIF-jaspilite	BIF, ferruginous chert, local banded quartz-magnetite-grunerite rock	This unit interpreted together with G6A1 in the geological map. However, it has completely different spectral characteristics.

G7A1	Sparsely distributed ferrous iron, FeOH, AlOH, and kaolin group minerals	Gritstone	Sandstone with beds of conglomerate minor siltstone and shale	
G7A2	Ferrous iron, AlOH group minerals	Hardy sandstone	Sandstone coarse to medium-grained, generally arkosic, but includes local volcanoclastic sandstone and siltstone	These units are found in outwash fans, and their spectral characteristics can be changed through time as new deposition happened.
G7A3	Ferrous iron, minor FeOH, and kaolin group minerals	-		
G7A4	Ferrous iron, minor FeOH, and kaolin group minerals	-	Colluvial, sand, silt, and gravel in outwash fans; unconsolidated	
G7A5	Ferrous iron, minor FeOH, and kaolin group minerals	-	Ferruginous duricrust includes massive, pisolitic and nodular ferricrete	
G8A1	Minor contents of ferrous iron, FeOH, and kaolin group minerals	-	Felsic volcanic sandstone, tuffaceous, local quartz sandstone	
G8A2	Sparsely distributed FeOH and kaolin group minerals	-	Felsic volcanic sandstone, tuffaceous, local quartz sandstone	
G9A1	High ferrous iron content, minor FeOH, and kaolin group minerals	MT ROE basalt	Massive porphyritic vesicular and amygdaloidal basalt; some pillow basalt	The mineral distribution confirms this unit is mafic rock, as explained by the geological map and field data.
G9A2	Minor contents of ferrous iron and kaolin group minerals	-	Partly consolidated colluvial sand, silt, and gravel in proximal outwash fans	-
G10A1	High ferrous iron content, minor FeOH, and kaolin group minerals	-	Amphibolite and amphibolite schist	Ferrous iron group minerals are the main constituents of mafic and ultramafic rocks, which makes these results reasonable.
G10A2	High ferrous iron content, minor FeOH, and kaolin group minerals	Tonalite, basalt, quartz vein, chlorite, schist, pyroxenite wall rock	Meta basalt and meta dolerite; local pillowed structures	
G10A3	High ferrous iron content, minor FeOH, and kaolin group minerals	Chert-quartz-chlorite-carbonate-schist, siltstone/sandstone		

G11A1	AlOH and kaolin group minerals	quartz-chlorite-carbonate-schist	schistose, metamonzogranite	Spectra of this unit show felsic composition, although its most parts show dark features in the band ratio images.
G11A2	High ferrous iron, minor FeOH, and kaolin group minerals	Ultramafic dike	Talc-carbonate chlorite serpentine, carbonate-schist	Minerals reasonably match the geological map and field data.
G2A3	Ferrous iron group minerals	-	Residual calcrete, massive nodular and cavernous limestone	Ferrous iron group minerals can be indicators of carbonates.
G5A12	Ferrous iron with minor kaolin and FeOH group minerals	-	komatiite basalt, massive and pillowed lavas, subvolcanic intrusions, local pyroxene	
G12A1	High ferrous iron content, MgOH group minor FeOH, and kaolin group minerals	Greywacke, carbonate, chert	Meta peridotite and serpentine-schist; meta dunite, chert	The ferrous iron group minerals such as olivine and pyroxene are constituents of peridotite and serpentine rocks, which are also rich in MgOH content.
G12A2	High ferrous iron content, minor FeOH, and kaolin group minerals	-	Metaperidotite and serpentine-schist; metadunite, chert	
G13A1	AlOH group minerals	Schist	porphyritic rhyolite and rhyodacite, local felsic volcanic rocks	This unit is compositionally felsic.
G13A2	Ferrous iron and kaolin group minerals	-	Partly consolidated colluvial sand, silt, and gravel, scree and talus	-
G13A3	High ferrous iron, sparsely distributed AlOH, FeOH and kaolin group minerals	-	Interlayered psammitic and pelitic rocks, shale, siltstone, and sandstone	
G14A1	Ferrous iron and kaolin group minerals	Fuchsitic chert, chlorite-quartz	carbonate, silicified mafic schist; komatiite basalt, massive and pillowed lavas, subvolcanic intrusions, local pyroxene	
G14A2	Ferrous iron and kaolin group minerals	-	shale, pelitic schist, siltstone	
G14A3	Ferrous iron and kaolin group minerals	-	carbonate_ altered and silicified, mafic schist	
G15A1	Ferrous iron and minor AlOH group minerals	-	Shale, chert, grey tuffaceous sandstone, and iron formation; dolerite includes local gabbro	A relatively mafic unit between two felsic rocks
G15A2	AlOH group minerals	sandstone	Quartz-porphyritic rhyolite, locally schistose	

The following figure ([Figure 5.10](#)) indicates lithological interpretations in the training area using the Sentinel-2 image and aerial photograph within the previously defined lithological boundaries. The visual interpretation of the sentinel-2 image in the validation area is attached as [Appendix 12](#). The sentinel-2 data was able to show the thin stratigraphic units and iron oxide rich zones.

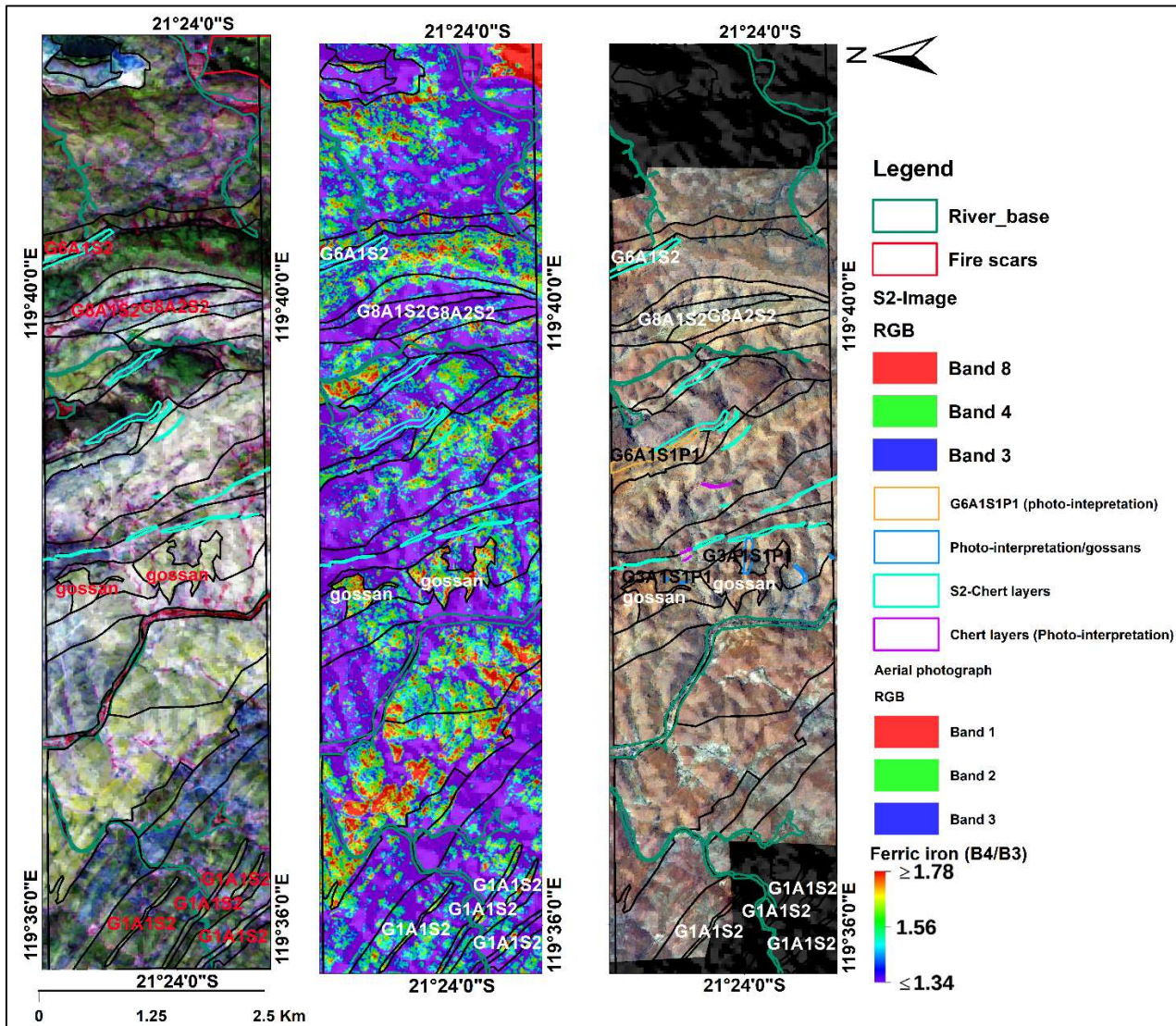


Figure 5. 10: Lithological interpretation along the training strip using sentinel_2 image within the previously defined boundaries from gamma-ray and ASTER data. The map on the left side is a false-color composite of the Sentinel-2 image. The mineral map is sentinel_2 band ratio (b4/b3). The map on the right side is an aerial photograph used to validate the occurrence of gossans, and chert layers interpreted using the sentinel-2 image. The only iron oxides validated by the aerial photograph are mentioned as gossans. Some details added using the aerial photograph are displayed in different colors, as mentioned in the legend. S2-chert is the outlines of the interpreted chert units resulted from the visual interpretation of the sentinel-2 color composite image. Only the units added using sentinel-2, and aerial photograph is explained here. The other lithological boundaries are described in [Table 5.2](#) above.

The aerial photograph was used to validate the lithological boundaries interpreted using the other remote sensing images, thin chert layers, and gossans interpreted using the sentinel-2 image. Its higher spatial resolution provides a chance to delineate the accurate boundaries, although its color contrast is low compared to the other remote sensing images ([see Appendix 13](#)).

Table 5. 3: Description of the lithological boundaries interpreted using Sentinel-2 data ([Figure 5.10](#)).

Assigned codes	Lithological description (source of the lithological information is the geological map)
G1A1S2	Quartz, feldspar, tonalite, and monzogranite as subvolcanic intrusions
G1A2S2	Komatiite, talc-carbonate, dolerite
G3A1S2	Gossanous units
G6A1S2	BIF and ferricrete (low radioelement content)
G8A1S2	Felsic volcanic sandstone, tuffaceous, local quartz sandstone
G8A2S2	felsic volcanic sandstone, tuffaceous, local quartz sandstone

5.4.2. Images classification

One of the results of maximum likelihood classification applied in the training area is (i.e., stacked gamma-ray and ASTER) indicated in [Figure 5.11](#), and the others are attached as [Appendix 14](#). The classification accuracies of the training area are 92.1087% for GRS, 91.2163% for ASTER-GRS, and 90.4515% for GRS-ASTER-Sentinel 2 images. The trend of these numbers shows that the accuracy is decreasing with increasing levels of details, although the difference is minimal. Decreasing accuracy with increasing levels of details might be due to the lower spectral/radiometric contrast between the newly interpreted lithological units. (example; differentiating dacite from rhyolite is not as easy as separating basalt from rhyolite in remote sensing). The lithologic groups identified using the gamma-ray data have a higher compositional variation between each other and then higher radiometric contrast. The lithologic units interpreted using the ASTER data within the pre-defined boundaries by gamma-ray data will have similar radiometric characteristics, and they only differ by spectral signatures. So when the stacked gamma-ray and ASTER data classified, the classification accuracy of the newly interpreted units partially decreases due to their similarity in radiometric characteristics. The Sentinel-2 data was also able to differentiate lithologic units that cannot be identified using the relatively lower resolution gamma-ray and ASTER datasets within the previously delineated boundaries. Therefore when the stacked gamma-ray, ASTER, and Sentinel-2 data classified, the accuracy of the newly added units partially decreases due to the similarity in the gamma-ray and ASTER responses with their parent units.

[Figure 5.13](#) shows the relationship between the surface area of the lithologic units with the classification accuracies. The graph partially shows a direct relationship even though the change is minor. That is expected because the accuracy difference from the low to the higher resolution images are also minor.

Although the accuracy is decreasing with an increasing level of detail, the differences are insignificant, and the accuracies are above the conventionally acceptable figure (i.e., >85%). Therefore the detailed classifications are preferable due to the amount of information they contain.

Legend of figure 5.11: the stratigraphic units are summarized from the geological map and the field data.

Symbol Stratigraphic unit

G1 Mafic and ultramafic rocks

G2 & G16 Felsic volcanics and volcanoclastic sediments

G3 Felsic volcanics and volcanoclastic sediments, relatively higher radioelement contents

G4 Komatiite basalt; relatively high radioelements

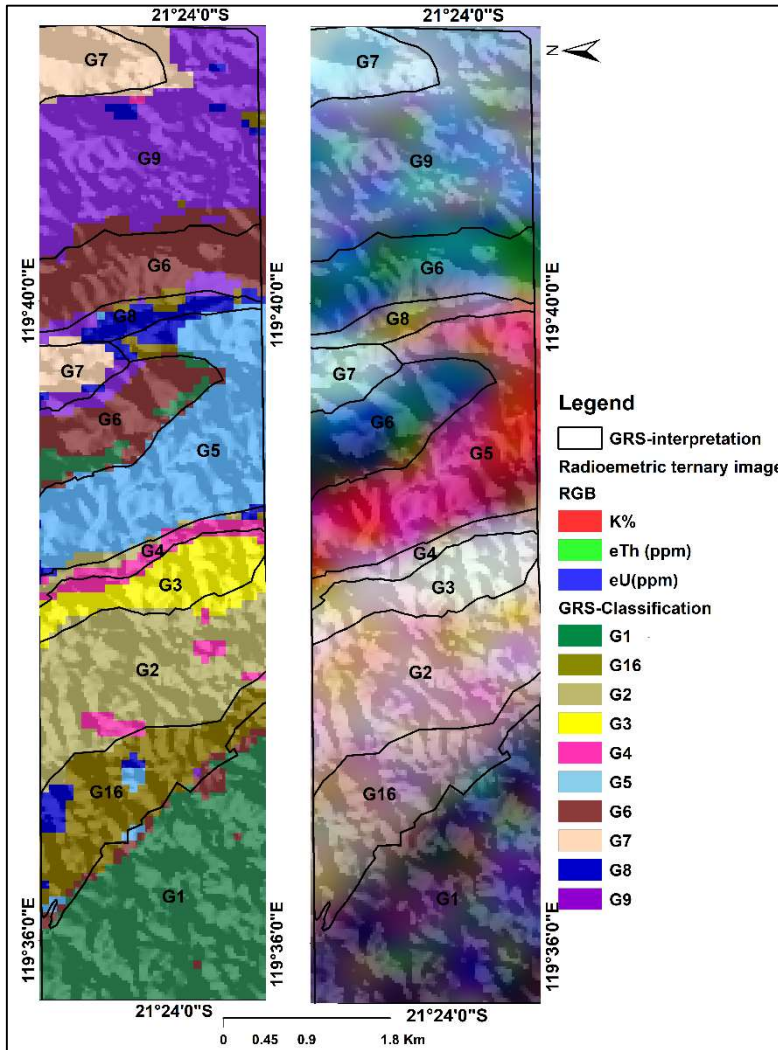
G5 Potassium enriched komatiite basalt and felsic volcanics

G6 Banded iron formation

G7 Sandstones and unconsolidated sediments

G8 Felsic volcanic rocks

G9 Basalt



The accuracy assessment in the training area was to compare the classified maps to the visual interpretations (i.e., to evaluate the quality of classification). On the other hand, the accuracy of the validation area is used to see the variations of the spectral/radiometric characteristics of the stratigraphic units throughout the study area that is an “uncommon” kind of validation.

Figure 5. 11: Maximum likelihood classified gamma-ray map and visually interpreted gamma-ray map of the training area. The classification accuracy was estimated by comparing the classified map (left) with the visual interpretation of the image (right).

Legend of figure 4.11: the lithological units come from the geological map and the field data.

Symbol	Lithology	Symbol	Lithology
G1A1	Mafic and ultramafic units of	G6A2	Felsic volcanic sandstone
G1A2 & G1A4	Dolerite-gabbro and talc-carbonate	G6A3	Sedimentary unit
G1A3	Tonalite	G6A4	Ferrous iron-rich rocks
G1A6	Dolerite and local gabbro	G7A1	Sandstone
G16A1, G2A1, G2A2, & G3A1	Felsic volcanics and volcanoclastic sediments	G7A2 and G7A3	Sandstone
G4A1	Komatiite basalt with high radioelements	G7A4	Unconsolidated sediments
G5A1	Potassium enriched felsic volcanic rocks	G7A5	Iron formation
G5A2	Potassium enriched komatiite basalt	G8A1 and G8A2	Felsic volcanic rocks
G5A4	Felsic volcanic sandstone	G9A1	Basalt
G5A6	Ferrous iron-rich rocks	G9A2	Partly consolidated colluvial sand
G6A1	BIF		

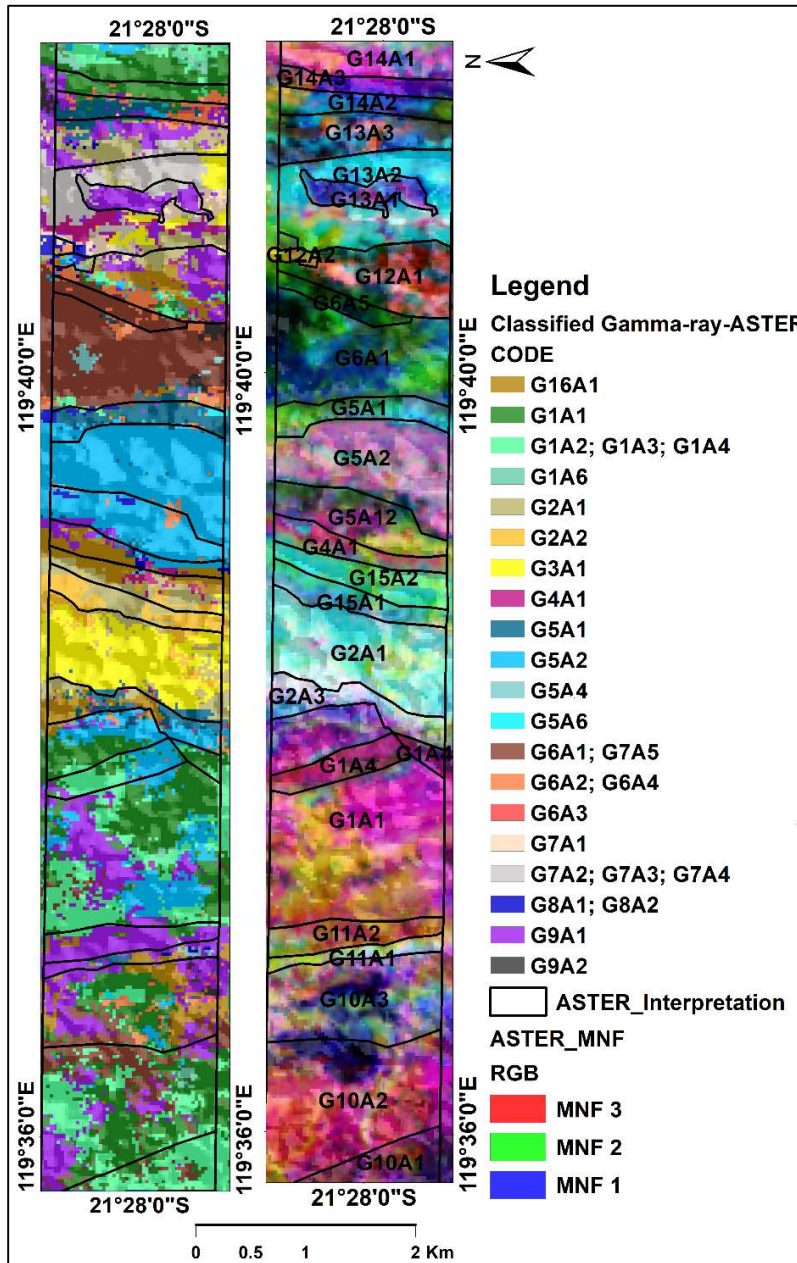


Figure 5. 12: Maximum likelihood classified map of stacked gamma-ray and ASTER data (left) and the visually interpreted ASTER image (right) in the validation area.

5.4.1. Extrapolation

In this thesis, the term 'extrapolation' is used to explain the applicability of the classification methods and spectral/radiometric signatures used to classify the training areas in the entire study area (see Section 4.5). Figures 5.14, 6.2, and Appendix 23 are the extrapolation results of stacked gamma-ray-ASTER classification, stacked gamma-ray-ASTER-Sentinel-2 classification, and gamma-ray classification, respectively. The major stratigraphic units were classified following the clear boundaries in all the three-step extrapolations even though the level of noise increases with increasing level of details. In the gamma-ray classification, the basaltic unit, which covers the northern part of the study area, is classified similar to the sandstone unit (see Appendix 23) due to its enhanced radioelement contents. However, in the stacked gamma-ray and remote sensing images, this unit was classified as a basalt (unit G9A1 of Figure 5.14) because the spectral responses of basalt and sandstone are quite different.

5.4.3. Validation

The accuracies of the classified images estimated on the validation area are 79.6954%, 68.4953%, and 67.8452% for the gamma-ray, Gamma ray-ASTER, and Gamma-ray-ASTER-Sentinel-2 classifications, respectively. The overall accuracy estimations in the validation area are much lower than those of the training area due to compositional variations of the north-south trending stratigraphic units. Compositional variation within a specific stratigraphic unit can be resulted either during the formation of the unit or later by geomorphologic activities. All the lithologic units which are part of the training area are not part of the validation area and vice versa. Therefore, only the continuous stratigraphic units were used to estimate the classification accuracy of the validation area. The units used to estimate the accuracy of the validation area are listed in Appendices 19, 20, and 21 for the three-stage image classifications.

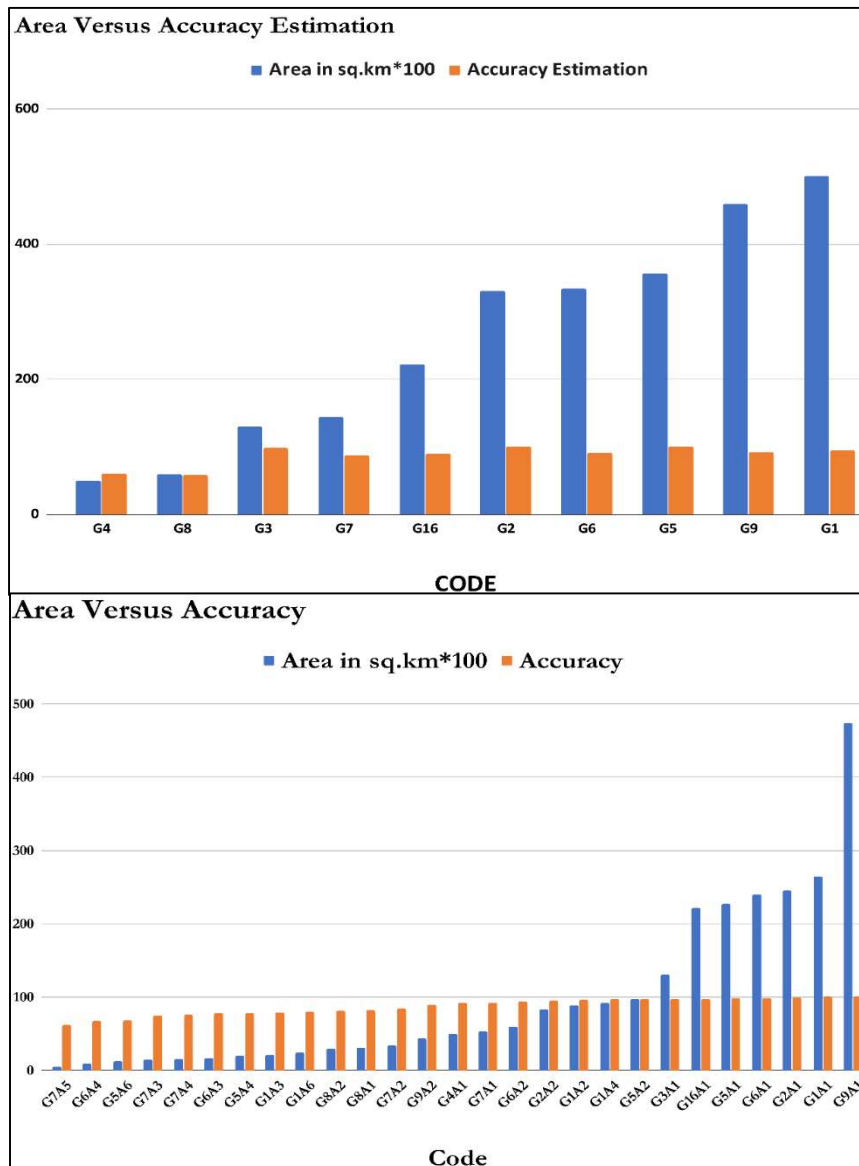


Figure 5. 13: Surface area of the lithologic units versus the accuracy of classifications. Area versus accuracy of gamma-ray image classification (top), of stacked gamma-ray, and ASTER image classification (bottom). Legends of the codes displayed here are mentioned on pages 32 and on this page.

Legend of figure 5.14: the stratigraphic units are summarized from the geological map and the field data.

<i>Symbol</i>	<i>Stratigraphic unit</i>
<i>G1</i>	Mafic and ultramafic rocks
<i>G2 & G16</i>	Felsic volcanics and volcanoclastic sediments
<i>G3</i>	Felsic volcanics and volcanoclastic sediments, relatively higher radioelement contents
<i>G4</i>	Komatiite basalt; relatively high radioelements
<i>G5</i>	Potassium enriched komatiite basalt and felsic volcanics
<i>G6</i>	Banded iron formation
<i>G7</i>	Sandstones and unconsolidated sediments
<i>G8</i>	Felsic volcanic rocks
<i>G9</i>	Basalt

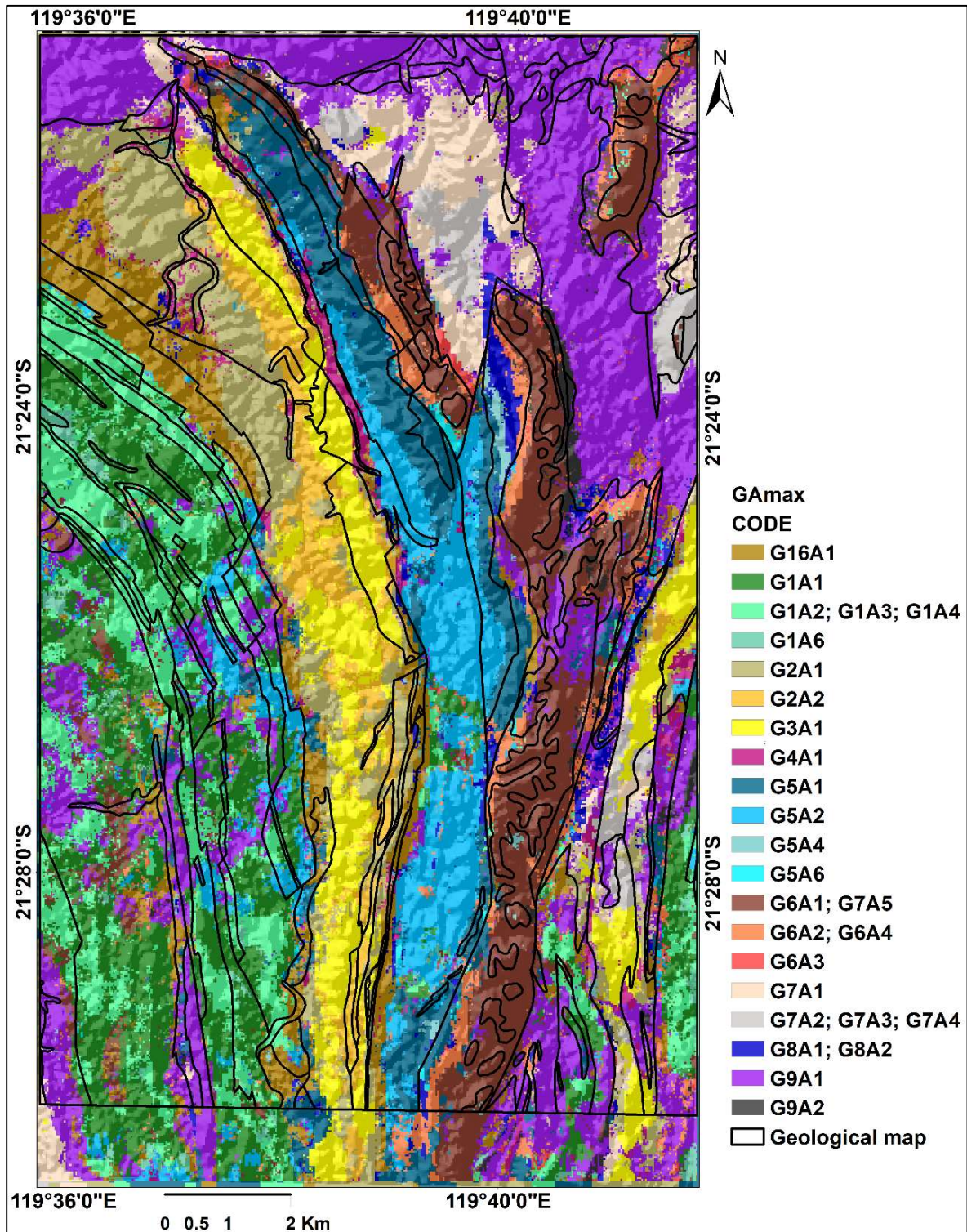


Figure 5. 14: Maximum likelihood classified map derived from stacked gamma-ray and ASTER data using classification signatures from the training area (extrapolation). The legend of this map is explained on the previous page.

6. DISCUSSION

Results of the data integration approach show new contributions in reconstructing the volcano-sedimentary sequences of the northern Coongan greenstone belt. This section discusses the results of the interpretations and the contributions of the gamma-ray, ASTER, and Sentinel-2 images as well as the aerial photograph in improving the lithostratigraphic interpretation of the northern Coongan greenstone belt.

6.1. Mineral indices

The mineral indices produced using ASTER and Sentinel-2 band ratios correlate with the geological map and field data interpretations. The mafic and ultramafic units and the iron formations are enriched in ferrous iron and FeOH group minerals (Barnes & Roeder, 2001). Ferrous iron group minerals such as chlorite, actinolite, pyroxene, olivine, and biotite are constituent minerals of mafic and ultramafic rocks. Mafic and ultramafic rocks are rich in iron and magnesium elements from which the term 'ferromagnesian rocks' was derived. Chlorite and actinolite minerals are the main constituent minerals of Archean greenstone belts, which gives green colors to the rocks. Ferrous iron group minerals are the dominant SWIR active minerals in the study area, and occur in the Talga Talga subgroup, parts of the Salgash subgroup, the Cleaverville formation, and the Fortescue group rocks. Magnesium hydroxyl (MgOH) group minerals occur in limited parts of the study area associated with serpentine, schistose, chlorite-schist, meta_peridotite, basalt, and gabbro units, ([see Appendix 9](#)). MgOH group minerals are constituents of hydrated ferromagnesian rocks that can be created either by metamorphism or alteration of carbonates, mafic and ultramafic units. The ASTER spectral were not able to indicate carbonate rocks in this study area. Impurities can affect spectra of rocks and give difficulty to differentiate them using coarse resolution data like ASTER. Parts of the Shay intrusive and thin linear features in the Talga Talga subgroup indicate the occurrence of magnesium hydroxyl group minerals.

The felsic volcanic rocks and volcanoclastic sedimentary rocks of the Duffer and Wyman formations are rich in aluminum hydroxyl (AlOH) group minerals. AlOH group minerals (i.e., phengite, muscovite, paragonite, lepidolite, illite, montmorillonite, kaolinite/dickite) can be either weathering products of felsic rocks or products of hydrothermal alteration. The integrated data analysis helped to identify the source of the AlOH group minerals. The association of the AlOH group minerals with rocks of felsic composition leads to the argumentation that the minerals could be weathering products of these rocks. The reaction of silica-rich rocks with surface water (hydration) can also form clay minerals. Nevertheless, there are additional indications of hydrothermal activities, especially in the Duffer formation. One of the supporting evidence for the presence of hydrothermal alteration is the association of iron oxide minerals with the volcanic and volcano-sedimentary rocks of felsic composition. It is unusual for compositionally felsic rocks to be enriched in iron oxides unless a deposition or hydrothermal alteration processes happened in that area. According to the digital elevation model, the felsic units of the Duffer formation are topographically elevated compared to the surrounding mafic rocks (i.e., Talga Talga and Salgsh subgroups). So the possibility of transportation and deposition of the iron oxide minerals from the mafic units to the felsic rocks is very low in this study area.

Moreover, the aerial photograph shows gossanous features in the Duffer formation. Gossans appear as smaller size dome-like structures showing dark brown colors and topographically elevated compared to the background lithology. Correlating all these observations leads to the conclusion that there are indications of hydrothermal alteration processes in the north-south trending Duffer formation of the northern Coongan greenstone belt.

In the north-central part of the study area, there is a kaolin group mineralization following a specific pattern ([Figure 5.3](#)). According to the geological map and field data, the host lithologies of this mineralization vary from felsic to mafic volcanics and sedimentary rocks, which are parts of the Salgash subgroup, Wyman formation, and the Fortescue group. This wide range of lithological variation showing uniform mineralization indicates that the mineralization in this area was not part of the primary depositional processes. There are various possibilities of post mineralization, such as deposition of transported materials and hydrothermal alteration processes. Therefore this area might indicate hydrothermal alteration processes since kaolin group minerals are indicators of this process.

Generally, the mineral distribution of the study area, which was able to be mapped using ASTER-SWIR and Sentinel-2-VNIR images, includes ferrous iron, aluminum hydroxyl, kaolin, iron hydroxyl, and magnesium hydroxyl group minerals from the most to the least dominant, respectively.

6.2. Lithological interpretation and images classifications

A stepwise geological interpretation was used to identify the spectral and radiometric characteristics of lithological units of the Coongan greenstone belt. The relative abundance of radioelements and their absolute contents was able to differentiate the lithologic groups with high compositional variations as felsic, intermediate, mafic/ultramafic, and “sedimentary” rocks. In most parts of the study area, the absolute and relative abundance of radioelements is conventional (i.e., higher content in felsic rocks; lower content in mafic and ultramafic rocks) (Wilford et al., 1997). Nevertheless, units G4 and G5 displayed in [Figure 5.11](#) (part of the Salgash subgroup) show unusual contents of radioelements ([see also Section 6.2.3](#)).

The ASTER data was able to differentiate the main lithologic units of the study area based on the surface mineral distributions and color composite of different band combinations, as described in [Table 5.2](#). Many details were added to the boundaries interpreted using gamma-ray data. The ASTER data was able to differentiate:

- The ferrous iron-rich mafic rocks, and MgOH rich talc-carbonate, serpentine, and peridotites
- Clay rich felsic volcanic rocks and felsic rocks with no diagnostic spectral feature
- Minor compositional variations within the same stratigraphic units caused by either geomorphologic activities or hydrothermal alterations

The high-resolution Sentinel-2 image used for the lithological interpretation has only four spectral bands at 10-meter resolution. Therefore it played a minor role in identifying the major lithologic units. Some lithological boundaries were added using the Sentinel-2 image, but most of the units were already delineated using the ASTER data apart from the units which have a small spatial extent. The Sentinel-2 data was able to delineate:

- The chert layers intercalated with different lithologic units
- The gossanous rocks/iron oxide rich zones

The lithological boundaries interpreted using ASTER and Sentinel-2 data do not necessarily indicate different stratigraphic units. A single unit can have a relative compositional difference in two or more different areas due to several reasons. This difference in spectral/electromagnetic response can happen by surface features that are affected by geomorphologic activities. The aerial photograph was very useful as a validation data of the sentinel-2 interpretation results due to its high resolution, which is almost a ground truth ([see Appendix 14](#)). The aerial photograph was able to delineate the gossanous rocks of the study area. The chert layers and other units which have a small spatial extent were mapped using the aerial photograph.

After visual interpretation of all datasets, image classifications were applied based on stepwise visual interpretations. The accuracy estimation of the three-step image classification shows a partial decrease as the level of detail increases. The gamma-ray classification provides higher overall accuracy due to the higher contrast between the different lithologic groups. The classification accuracy of the stacked GRS-ASTER is lower than that of the gamma-ray and higher than the accuracy of the stacked GRS-ASTER-Sentinel-2. This might be unexpected because accuracy usually increases with increasing resolution of data. If the lithological boundaries were the same, classification accuracy should increase with increasing resolution of data. However, when more lithologic units were added to the previously interpreted groups, the spectral/radiometric contrast between the newly added units might be minor, and differentiating them becomes more difficult due to their similarity in spectral/radiometric characteristics. In this case, the overall classification accuracy decreases with an increasing level of detail. The fact that they were differentiable in the visual interpretations is because only the relatively higher resolution ASTER/sentinel-2 image was used for the visual interpretations. But, the image classifications include the gamma-ray data, and the units interpreted using the ASTER/Sentinel-2 data have similar radiometric characteristics with their parent units.

The accuracy estimations on the training area are much higher than that of the validation area. The classified maps also look noisy in the southern parts of the study area (see Figure 5.14). This indicates variations in spectral/radiometric characteristics of the stratigraphic units as we go from north to south, which is an implication of compositional variations. The north-south compositional variation might not necessarily be associated with the primary compositional variation. Instead, it can be due to geomorphologic activities like weathering, erosion, deposition, alteration, and so on. In fact, there are also lithologic units which are not continuous from north to south and vice versa. The Fortescue group and the Croydon group stratigraphic units found only in the northern part of the study area. So they are parts of the training area but not the validation area. On the other hand, the Dalton suit group ultramafic intrusions occur only in the southern part of the study area, which is not included in the training area. Generally, the northern half of the study area is classified more accurately compared to the southern half.

Stratigraphy of the Coongan greenstone belt shows a younging sequence as we go from west to east of the study area (Zegers, 1996). The following subsections describe the major stratigraphic units of the Coongan greenstone belt and their correlation with the interpretation results of this thesis. The lithologic groups mentioned in the following subsections are based on the Australian Stratigraphic Units Database Geoscience Australia and Australian Stratigraphy Commission., (2017), and the literature works by (Hickman & Van Kranendonk, 2012; Zegers 1996) as well as the unpublished field description document by Hein et al., (n.d.). The stratigraphic sequences were interpreted in groups, subgroups, and formations based on their stratigraphic level explained in the Australian Stratigraphic Units Database (Geoscience Australia and Australian Stratigraphy Commission, 2017).

The main stratigraphic boundaries interpreted by Hickman AH, Van Kranendonk, (2008) are compared to the lithological interpretations of this thesis, as showing in Figure 6.1 below. The boundaries mostly fit each other except in some areas which show partial shifts. These partial shifts can result from the difference in spatial resolution of the datasets from which the lithological interpretations were made.

6.2.1. The Talga Talga subgroup

The Talga Talga subgroup is the oldest subgroup of the Warawoona group, which is Paleoproterozoic in age (ca. 3.49-3.31 Ga). This unit is generally mafic in composition, which comprises massive and pillowed basalts, tholeiitic basalts with interbedded thin chert units, and minor felsic rocks (Zegers, 1996). It also

includes dolerite and gabbro sills and minor iron formations. It is represented by **B and E** in [Figure 6.1](#). This unit is split into two main components, by a relatively felsic unit which is not part of the Talga Talga subgroup (Emu pool super suite). The westernmost part of the Talga Talga subgroup shows relatively greenish color in the radiometric ternary image due to relative thorium enrichment compared to the other radioelements. In the geological map, the western part of the Talga Talga subgroup ([unit B of Figure 6.1](#)) is described as metabasalt and metadolerite. The eastern half of the Talga Talga subgroup ([unit E of Figure 6.1](#)) is komatiite basalt, massive, and pillowed lavas. It appears as a dark unit in the geophysical and remote sensing data due to its mafic composition. It is also relatively enriched in ferrous iron group minerals.

The gamma-ray classification result of the Talga Talga subgroup ([see Appendix 23](#)) indicates the occurrence of iron formations intercalated with the mafic rocks confirming the previous studies Zegers, (1996) and the geological map used in this thesis. The relative difference in spectral responses of the different units intercalated within the Talga Talga subgroup makes the classified remote sensing images a bit noisy ([see Figure 5.14](#)). However, the overall picture shows a clear boundary with the other major stratigraphic units.

6.2.2. The Duffer formation

The Duffer Formation (i.e., [unit F of Figure 6.1](#)) consists of mainly felsic volcanics and volcanoclastic sediments. Its thickness varies between 1 and 3 km, which increases from south to north. The main lithologic units of this formation are rhyolites, dacites, agglomerates sandstone, and conglomerates. The duffer formation shows a gossanous appearance and is often intercalated with chert layers in various locations. The Duffer formation (ca. 3.47-3.46 Ga) occurs between the Talga Talga and Salgash subgroups of the Warrawoona group. It is part of the Coongan subgroup, which is included in the Warrawoona group. The interpretation results of this study show that the composition of the duffer formation varies from west to east, especially in its northern part. The radioelement contents and the AIOH mineral groups increase from west to east, which indicates the acidity of the rocks is increasing in this direction. The aluminum hydroxyl enrichment can be due to the accumulation of hydrothermal alteration products. The north-western part of the duffer formation shows mafic spectra in the remote sensing images, although the geological map described it as a felsic volcanics and volcanoclastic sedimentary rocks (i.e., dacitic volcanic breccia; porphyritic dacite breccia, local volcanoclastic sandstone, tuff, and conglomerate). The mafic spectral response can result from the intercalated mafic intrusives (dolerite/gabbro), as indicated in the field data. In this study, the duffer formation is described as an altered unit due to the occurrence of gossans and AIOH bearing minerals.

6.2.3. The Salgash subgroup

The Salgash subgroup is the upper part of the Warrawoona group, dated at ca. 3.46-3.43 Ga ([unit G of Figure 6.1](#)). The Salgash subgroup has mafic and felsic parts. The mafic unit contains major komatiite basalt, massive and pillowed lavas, and subvolcanic intrusions. The felsic component of the Salgash subgroup includes porphyritic rhyolite, rhyodacite, felsic volcanic sandstone, tuff, and local quartz sandstone (Hickman AH, Van Kranendonk, 2008). The Salgash subgroup has relatively high potassium content and shows reddish color in the radiometric ternary image. The mafic part of the Salgash subgroup shows two distinct features in the gamma-ray data. The western part of the mafic unit ([unit G4 of Figure 6.1](#)) consists of a higher content of all three radioelements, approximately similar to the felsic volcanic rocks, which is unexpected ([see Table 5.1](#)).

On the other hand, the eastern part of the mafic unit in the Salgash subgroup (i.e., [part of unit G5 in Figure 6.1](#)) shows selective potassium enrichment while it contains very low contents of thorium and uranium. The selective potassium enrichment of unit [G5 of Figure 6.1](#) can happen due to several reasons. Potassium is

sensitive to weathering, and it can be easily leached out. In this case, the felsic component of unit **G5** should contain relatively higher potassium content naturally since felsic rocks usually do. (i.e., the felsic component of unit **G5** is rhyolite rock that is an extrusive equivalent of granite). Hence the potassium enrichment of the komatiite basalt can be resulted by the deposition of transported materials from the felsic unit. The mafic and felsic components of the Salgash subgroup were determined using the ASTER image interpretation. The Salgash subgroup shows some intercalations with the Wyman formation ([see Figure 6.1](#)).

6.2.4. Wyman formation (Kelly group)

The Wyman formation (ca. 3.325–3.318 Ga) is part of the Kelly Group, which overlays the Salgash subgroup ([unit J of Figure 6.1](#)). Felsic volcanic sandstone, tuff, local quartz sandstone, felsic volcanic rock, porphyritic rhyolite, rhyodacite, chert, pelitic schist, shale, minor siltstone, and local basalt are the lithologic units of the Wyman formation. The Wyman formation occurs in several parts of the study area, as indicated in [Figure 6.1 \(unit J\)](#). Generally, it has a felsic composition except in some parts showing low content of radioelements. Aluminum hydroxyl and kaolin group minerals occur in this formation. Part of the Wyman formation that is located in the south-eastern part of the study area has similar spectral characteristics to the duffer formation and also classified similarly to gossanous rocks see [Figure 6.2](#). However, the gossanous signatures in the Wyman formation might not result from true gossans. The sentinel-2 image in this formation was affected by fire scars, and the gossanous signature might be due to the impact of fire scars (i.e., the unit represented by [2 in Figure 6.2](#)). Radiometrically the Wyman formation located in the south-eastern part of the study area is similar to the Lalla Rookh sandstone see [Figure 6.1](#).

6.2.5. Kelly ultramafic unit

The south-eastern end of the study area ([unit O of Figure 6.1](#)), which is part of the Kelly Group, contains carbonate-altered and silicified, fine- to medium-grained mafic schist according to the geological map by Hickman AH, Van Kranendonk, (2008). However, the ASTER data used in this study was not able to identify the carbonate signatures. In fact, ASTER is not very good at identifying individual minerals due to its coarse resolution. So there might be a possibility of mixing with the other MgOH group minerals identified using the ASTER band ratio ([see section 5.3.5](#)). This unit has elevated uranium content compared to the other radioelement contents and shows blue color in the radiometric ternary image. Its lower potassium content and elevated ferrous iron group minerals indicate that the unit has mafic composition. It was classified similarly to the Talga Talga subgroup in all the three-step image classification results due to its mafic composition.

6.2.6. Emu pool super suit

The Emu pool super suit is a compositionally felsic unit located between the western and eastern parts of the Talga Talga subgroup ([unit C of Figure 6.1](#)). It shows relatively higher radioelement contents and AlOH group minerals, which makes it relatively felsic compared to the surrounding mafic rocks. A thin (ca. 0.5 km) deformed ultramafic unit (carbonate-chlorite schist) overlays this felsic unit ([see Figure 6.1](#)).

6.2.7. Shay intrusion

The shay intrusion (Ca. 3.04) is part of the Dalton suite group, which comprises a Mesoarchean age (3.20–3.07 Ga) ultramafic intrusions ([unit M of Figure 6.1](#)). The lithologic units of the Shay intrusion are gabbro, dolerite, dunite, peridotite, serpentine-chlorite schist, serpentinite, meta-pyroxenite, and ultramafic schist. This unit is located in the south-eastern part of the study area, and its thickness increases from north to south. It shows a relative uranium enrichment and ferrous iron group minerals in the gamma-ray and remote sensing data, respectively. It is also one of the units indicating MgOH group minerals, the other being the

Talga Talga subgroup. This unit was not well classified in all datasets because it does not continue up to the training area, and there were no representative samples of it.

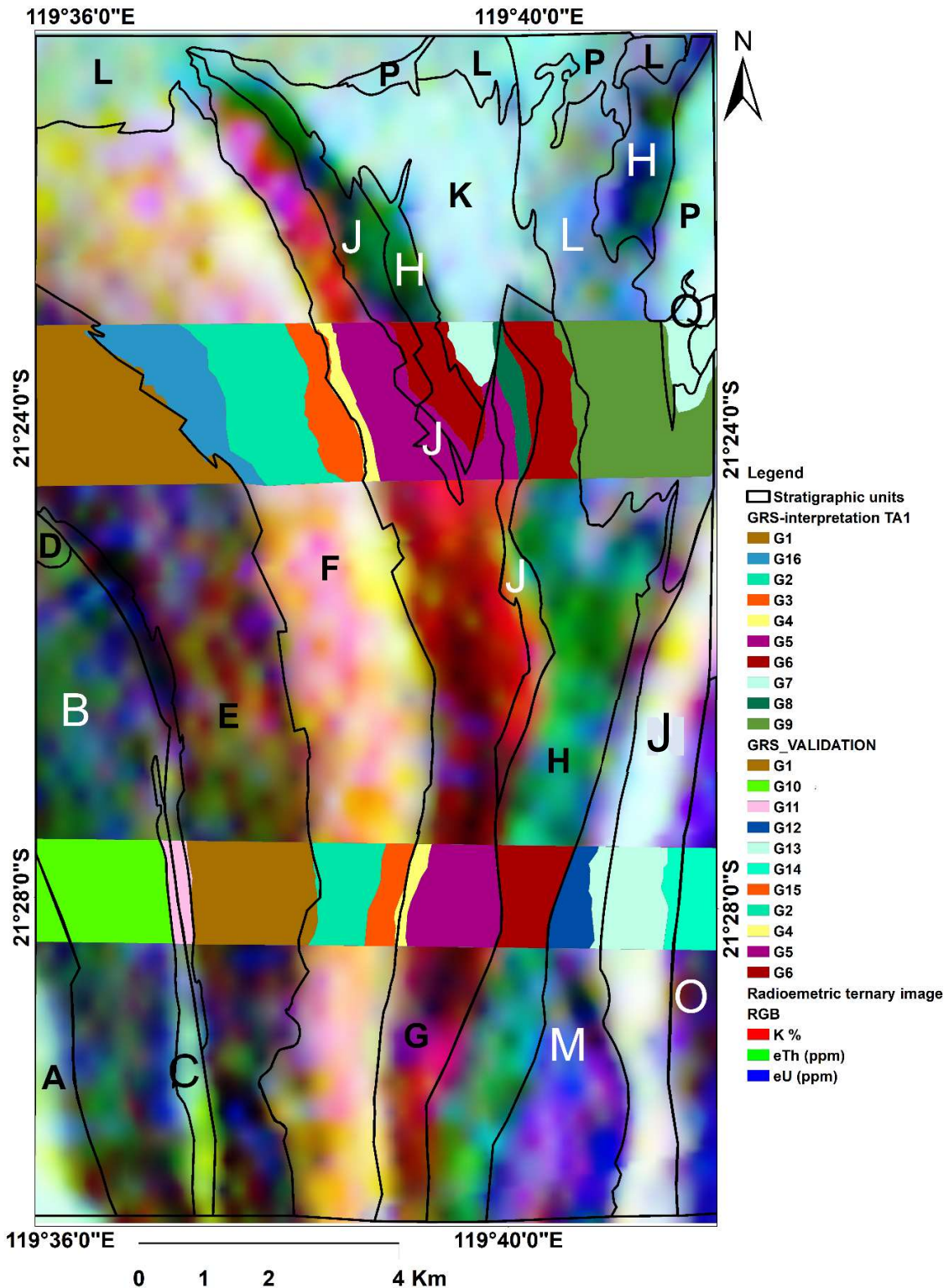


Figure 6. 1: Gamma-ray interpretations of the training and validation areas underlying the major stratigraphic boundaries of the northern Coongan greenstone belt. The stratigraphic boundaries were interpreted by Hickman AH, Van Kranendonk, (2008). The codes mentioned in the legend are explained in [Table 5.1](#). According to the geological map, unit [A](#) is amphibolite and amphibolite schist. Unit [P](#) displayed in the northern part of this map is partly consolidated colluvial sediments. The other units are described in the subsections above and below.

6.2.8. Cleaverville formation (Gorge Creek group)

The Cleaverville formation dated Ca. 3.02-3.15 Ga is part of the Gorge Creek group that ages ca. 3.05-2.94 Ga. It is a sedimentary unit that contains thick banded iron-formation, ferruginous chert, local banded quartz-magnetite-grunerite rock, chert, and minor jaspilite. The Cleaverville formation appears as a dark unit in the remote sensing images due to the occurrence of ferrous iron group minerals ([unit H of Figure 6.1](#)). It is well classified (i.e., coherent with the clear boundaries) in all the three-step image classifications due to its distinctive spectral/radiometric characteristics compared to other stratigraphic units. It has relatively enhanced thorium content and shows greenish color in the radiometric ternary image. A large portion of the Cleaverville formation is covered by Cenozoic residual sediments (Hickman AH, Van Kranendonk, 2008). The reason for thorium enrichment in the Cleaverville formation can be the occurrence of these residual sediments since thorium is less mobile, and it usually associates with leftover sediments. Potassium and uranium are relatively soluble and mobile elements, respectively, which are sensitive to geomorphologic activities.

6.2.9. Lalla Rookh formation (Croydon Group)

The Lalla Rookh formation part of the Croydon group is located in the northern part of the study area ([unit K of figure 6.1](#)). It is a Mesoarchean age (2.95-2.94 Ga) unit that includes sandstone with beds of conglomerate, minor siltstone, and shale. It has relatively higher radioelement contents compared to the surrounding mafic rocks. The ASTER spectra of this unit did not show any diagnostic features because silica is less active in the shortwave infrared wavelength region. It also indicates iron oxide occurrences. Iron oxides usually occur in sandstones as cementing materials and resulted in red sandstones. Some parts of the Lall Rookh sandstone and the Hardy sandstone were classified as the same group in the remote sensing maps due to their similarity in spectral/radiometric characteristics.

6.2.1. Fortescue group (Mount Bruce Supergroup)

The Fortescue group (ca. 2.78-2.63 Ga) comprises the Mount Roe basalt, the Hardy sandstone, and Kylenea formation (Hickman AH, Van Kranendonk, 2008). The Mount Roe basalt covers the northern and north-eastern parts of the study area (i.e., [unit L of Figure 6.1](#)). It comprises massive, porphyritic, vesicular, and amygdaloidal basalt, some pillow basalt, dolerites, conglomerate, pebbly sandstone, sandstone, chert, and quartz clasts (Zegers, 1996). The Mount Roe basalt show relatively enhanced radioelement contents compared to the other mafic rocks. The gamma-ray image classification result shows the northern part of the study area, which is the MT Roe basalt, was classified with the felsic sandstone of Lalla Rookh formation ([Appendix 23](#)). However, the classified remote sensing images were able to delineate the whole MT Roe basalt with accurate boundaries, as indicated by the geological map ([Figures 5.14 and 6.2](#)). Alluvial and colluvial sediments overlay the MT Roe basalt in various locations ([unit P of Figure 6.1](#)).

The Hardy sandstone of the Fortescue group consists of arkosic coarse to fine-grained sandstone, local volcanoclastic sandstone, and siltstone ([unit Q of Figure 6.1](#)). The Hardy sandstone shows a felsic response in the remote sensing and geophysical datasets. A small part of the Kylenea formation is included in this study area ([unit D of Figure 6.1](#)). Its lithologic units are massive and vesicular tholeiitic basaltic andesite and Pillow basalt. The Kylenea formation has relatively higher thorium content compared to the surrounding mafic rocks.

6.3. Hydrothermal alteration

Literature works mentioned that low-grade metamorphism and hydrothermal alteration are common processes in the Coongan greenstone belt (Zegers, 1996). Carbonate alteration and silicification are

mentioned as typical alteration processes in greenstone belts. Hydrothermal alterations usually show distinctive features in remote sensing and geophysical datasets. Some unique characteristics of hydrothermal alterations are selective enrichment/depletion of radioelements (i.e., potassium), enrichment of clay minerals, the occurrence of volcanogenic massive sulphides, and the presence of chert layers.

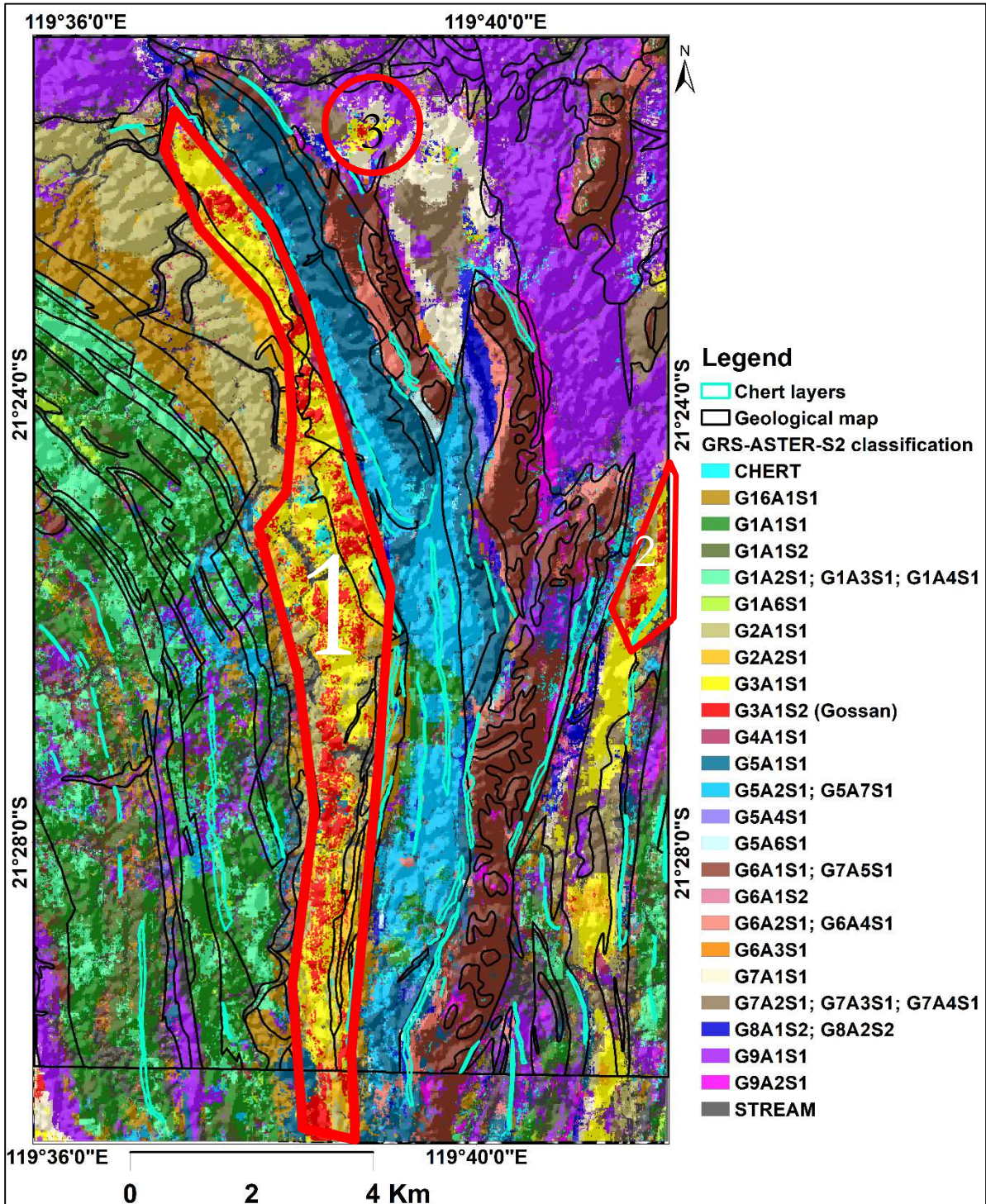


Figure 6. 2: Maximum likelihood classified map of stacked gamma-ray, ASTER, and Sentinel-2 images. Spectral signatures used to classify this map are collected from the training area (extrapolation). The legend of this map is displayed below. The red boundaries were drawn to show lithologic units, which were classified as gossanous features.

In this study, the indications of hydrothermal alterations were interpreted based on the relationships between the radioelement contents, and mineral groups with lithologies described in the geological map and field data. The gamma-ray data shows an unusual distribution of radioelements in the Salgash subgroup (i.e., selective potassium enrichment). However, the remote sensing data did not indicate any hydrothermal alteration mineral occurrences in this area. The selective potassium enrichment can result from deposition of transported materials.

Legend of figure 6.2: the lithological units come from the geological map and the field data.

Code	Lithologic units	Code	Lithologic units
G1A1S1	komatiite basalt, massive and pillowed lavas, local pyroxene	G6A1S1, G6A1S2	BIF and ferricrete (low radioelement content)
G1A1S2	Quartz, feldspar, tonalite, and monzogranite as subvolcanic intrusions	G6A2S1	felsic volcanic sandstone, tuffaceous, local quartz sandstone
G1A2S1, G1A2S2, G1A4S1	Komatiite, talc-carbonate, dolerite	G6A3S1	sandstone with beds of conglomerate, minor siltstone, and shale
G1A3S1	pillowed and variolitic komatiite basalt	G6A4S1	Felsic volcanic sandstone, tuffaceous, local quartz sandstone BIF
G1A6S1	Dolerite and local gabbro	G7A1S1	Sandstone with beds of conglomerate, minor siltstone, and shale
G2A1S1	Dolerite-gabbro, Volcanic sandstone, dacitic volcanic breccia	G7A2S1	unconsolidated sand (high TC)
G2A2S1	Dacitic volcanic breccia, sandstone, tuff, conglomerate	G7A3S1	Ferruginous duricrust, ferricrete
G3A1S1	Rhyolitic tuffaceous volcanoclastic sandstone, ash beds	G7A4S1	Colluvial sand, silt, and gravel in outwash fans
G3A1S2	Gossaneous rocks	G7A5S1	ferruginous duricrust, pisolitic, and nodular ferricrete
G4A1S1	Komatiite basalt	G8A1S2	felsic volcanic sandstone, tuffaceous, local quartz sandstone
G5A1S1	potassium enriched Felsic volcanic sandstone, local quartz sandstone, andesite rock	G8A2S2	felsic volcanic sandstone, tuffaceous, local quartz sandstone
G5A2S1	potassium enriched komatiite basalt	G9A1S1	Massive porphyritic, vesicular and amygdaloidal basalt
G5A4S1	Felsic volcanic sandstone, tuffaceous, local quartz sandstone	G9A2S1	Colluvial sand, silt and gravel
G5A6S1	Ferruginous chert, banded quartz	G16A1S1	Dolerite-gabbro, felsic volcanic sandstone, local chert dacitic volcanic breccia
G5A7S1	potassium enriched Felsic volcanic sandstone, local quartz sandstone, andesite rock		

The ASTER band ratios (B5+B7)/B6 and B6/B5 show clay-rich stratigraphic zones along with the Duffer formation ([unit 1 of Figure 6.2](#)) and in the northernmost part of the Salgash subgroup, respectively. These clay-rich stratigraphic zones can be indications of hydrothermal alterations. The gamma-ray data did not show any unique characteristics in these areas. The Duffer formation is also enriched in iron oxide minerals, while its natural composition is felsic (the unit represented by [1 in Figure 6.2](#)). The iron oxides that are associated with felsic rocks can be products of hydrothermal alteration processes. The Duffer formation also appears gossanous in the high-resolution aerial photograph ([Appendix 13](#)). Gossans are weathered and decomposed parts of volcanogenic massive sulphides (Van Kranendonk, 2006).

Additionally, the field data indicates the presence of gossans in the Duffer formation. Based on the criteria mentioned in the above paragraphs, the duffer formation is nominated as a hydrothermally altered unit. Unit [G3A1S2 in Figure 5.10](#) is interpreted as a gossanous rock. The classification result of the stacked GRS-ASTER-Sentinel-2 indicates the occurrence of gossanous rocks throughout the north-south trending duffer formation (i.e., the unit represented by yellowish color in [Figure 6.2](#)). The unit represented by 3 in [Figure 6.2](#) also classified as a gossanous unit, but the aerial photograph does not indicate any features related to gossan.

Generally, indications of hydrothermal processes are present throughout the study area since the chert units interlayered with all the stratigraphic units of the coongan greenstone belt are also indicators of hydrothermal processes. However, the Duffer formation is a promising area showing strong alteration characteristics, including ALOH enrichment ([Figure 5.3](#)), the occurrence of gossans ([Appendix 13](#)), and the often intercalated chert layers ([Figure 6.2](#)). Potential economic mineral deposits are associated with volcanogenic massive sulphides/gossans (Van Kranendonk, 2006). From this study, the Duffer formation looks prominent area for mineral deposits, and further studies are needed.

Hydrothermal systems are the most favored sites for searching for early life in addition to their importance as sources of economic mineral deposits (Van Kranendonk, 2006). The Physico-chemical conditions in the hydrothermal systems show partial similarities to the conditions of the early earth due to the presence of heat and water in both conditions. Around 3.5 Ga, there was massive volcanism, and high ambient temperature on the earth, which makes it almost similar to hydrothermal systems. The dominant minerals and rocks in hydrothermal systems indicate fossil records of their genetic inheritance. Hydrothermal springs usually contain high concentrations of dissolved materials. When discharge happens, gasses are released, which leads to temperature falls and then deposition/precipitation of dissolved components. These dissolved components are usually carbonates, silica, iron, and manganese oxides, which forms barite, cherts, and gossans during their deposition (Gillings, 1996). Any living organisms which were existing in the hot springs become fossilified and preserved within the deposited sediments since the environment was anaerobic.

The need for early life studies of the earth is to find correspondent characteristics of the planet Mars. Several studies indicate that early mars was almost similar to early earth, and hydrothermal systems on the earth show a similarity for hydrothermal systems on mars to some extent (Gillings, 1996).

6.4. Chert layers of the Coongan greenstone belt

Chert layers are located in various areas of the Coongan greenstone belt intercalated with all the stratigraphic units ([see Figure 6.2](#)). Visual interpretation of the Sentinel-2 image and the aerial photograph was able to show these chert layers ([see Appendix 13](#)). The visually interpreted chert layers were not well classified in the stacked GRS-ASTER-Sentinel-2 map. Lithologic units with a smaller size can be better indicated by visual interpretation than image classification.

There are two different points of view about the formation of chert units in the eastern Pilbara Craton. The first one stated that chert units were deposited as epiclastic and evaporative sedimentary units and then silicified later through the circulation of hydrothermal fluids (Buick & Dunlop, 1990; Van Kranendonk et al., 2002). The second point of view stated that chert units were originally precipitated from hydrothermal fluids. In both cases, chert units are indicators of hydrothermal processes. Therefore the abundance of interbedded chert layers in the Coongan greenstone belt can be an indicator of hydrothermal processes.

6.5. Data integration

Combining several datasets for geological interpretations is useful to improve the certainty of the interpretations. Example: Gamma-ray image interpretations confirmed by ASTER and Sentinel-2 image interpretations can improve the quality of the results. In this study, integrated analysis of remote sensing and gamma-ray images aided by field geological interpretations were able to show the relationships between the rock units and their spectral/radiometric characteristics. The rock units mentioned in the geological map and field data show the following characteristics in the gamma-ray and remote sensing images.

The mafic and ultramafic rocks contain a low content of radioelements, high ferrous iron group minerals, and appear as dark units in the aerial photograph. Eg. The Talga Talga subgroup and the MT Roe basalt.

The felsic volcanic rocks affected by alteration/weathering indicate a high content of radioelements and AlOH bearing minerals. These rocks show a gossanous appearance in the aerial photograph. Eg. The Duffer formation.

The unaltered felsic volcanic/volcanoclastic rocks show high radioelement contents without any SWIR active mineral indications. Eg. the Lalla Rookh formation

The altered/metamorphosed talc-carbonate rocks (i.e., according to the geological map) appear as dark features in the gamma-ray data and show minor MgOH group minerals in the ASTER band ratio.

The iron formations contain relatively higher thorium content compared to the other radioelements and ferrous iron group minerals. Eg. the Cleaverville formation

Iron oxides mapped using the Sentinel-2 band ratio occur throughout the study area either as primary constituents of the rocks or as surface coating materials.

The data integration also added more information about the study area that was not well-known before this study. The indications of hydrothermal processes and the chert units delineated by the data integration approach are some of the most important contributions to the geological interpretation of the study area.

Stepwise interpretation from low to high-resolution data helps in delineating the accurate lithological boundaries.

7. CONCLUSION AND RECOMMENDATIONS

7.1. Conclusion

The following conclusions are drawn based on the results of the analysis and presented together with the research questions.

7.1.1. Which VNIR/SWIR active minerals are present in the study area?

Maps of mineral indices were produced using ASTER and Sentinel-2 band ratio algorithms. The mineral groups identified in short wave infrared are ferrous iron, aluminum hydroxyl, kaolin, iron hydroxyl, and magnesium hydroxyl group minerals. Ferrous iron mineral groups are the most dominant minerals in the study area, which associates with all the mafic, ultramafic igneous rocks, and banded iron formations. Aluminum hydroxyl group minerals occur in the felsic volcanic rocks and volcanoclastic sediments, specifically the Duffer formation, the Wyman formation, and minor contents in the Hardy formation. The kaolin group minerals show a typical pattern in the north-central part of the study area. These mineral groups occur in the rhyolitic rocks of the Salgash subgroup and Wyman formation. They also cover part of the Fortescue Group, which has basaltic composition. Kaolin group minerals occur sparsely distributed throughout the study area except in the felsic volcanics and volcanoclastic sediments of the Duffer and Wyman formations (but found in the northern part of Wyman formation). Iron hydroxyl group minerals occur in minor contents sparsely distributed in the mafic, ultramafic igneous rocks, and iron formations. Magnesium hydroxyl mineral groups occur in limited locations associated with serpentine, schistose, chlorite-schist, meta_peridotite, basalt, and gabbro rocks, specifically in the Shay intrusion and the Talga Talga subgroup.

Iron oxide minerals were mapped using Sentinel-2 band ratios. Iron oxides occur throughout the study area either as main components of the rocks or as coatings and deposited materials. Goethite and hematite are the iron oxide types found in the study area. Cleaverville formation and the Lalla Rookh sandstone are enriched in goethite and hematite minerals. On the other hand, hematite mineral occurs in the Duffer formation and the southern part of the Salgash subgroup. The occurrence of iron oxides was validated by visual interpretation of the aerial photograph. Areas containing iron oxides appear as dark brown colors in the aerial photograph.

7.1.2. How does the contribution of each dataset can help in reconstructing the volcano-sedimentary sequence of the northern Coongan greenstone belt?

Each of the datasets used in this study contributes specific information to the interpretation. The geophysical data was able to delineate stratigraphic units with higher compositional variations. Generally, the gamma-ray data was able to identify the following units.

- The mafic and ultramafic units of the Talga Talga subgroup; komatiites, basalt, dolerite/gabbro
- The felsic volcanic and volcano-sedimentary rocks of the Duffer formation with relative enrichment in radioelement contents from west to east
- The selectively potassium enriched Salgash subgroup consisting of massive/komatiite basalts and rhyolitic tuffaceous rocks.
- The Cleaverville formation with enhanced thorium content compared to the other stratigraphic units.
- The Lalla Rookh and the Hardy sandstones which contain high radioelement contents
- The Fortescue Group containing relatively enhanced radioelement contents compared to the other mafic and ultramafic rocks
- The Shay intrusive with enhanced uranium content compared to the other radioelements

The ASTER data was used to differentiate relative compositional variations among felsic and/or mafic rocks as well as sedimentary units. Lots of details were added using the ASTER data to the pre-defined lithological boundaries using gamma-ray data. For example, the Salgash subgroup has mafic and felsic components, which have similar radiometric characteristics. But the ASTER data was able to differentiate the mafic and felsic rocks.

The Sentinel-2 data was used to map lithologic units with a smaller spatial extent like chert, gossans, and different linear features. Specifically, it was useful to map iron oxide rich zones as indicators of hydrothermal alteration.

7.1.3. What is the accuracy of the geological maps produced from geophysical and remote sensing data?

The accuracy of the classified maps was estimated in the training and validation areas. The resulted accuracy estimations are:

Training area

- Gamma-ray classification 92.1087%
- Stacked gamma-ray-ASTER classification, 91.2163%
- Stacked gamma-ray-ASTER-Sentinel-2 classification, 90.4515%

Validation area

- Gamma-ray classification 79.6954%,
- Stacked gamma-ray-ASTER classification, 68.4953%,
- Stacked gamma-ray-ASTER-Sentinel-2 classification, 67.8452%

Classification accuracy decreases from the gamma-ray data to the resampled and stacked gamma-ray-ASTER data and then to the stacked gamma-ray-ASTER-Sentinel-2 data in the training and validation areas. A partial similarity in spectral/radiometric characteristics of the newly interpreted lithologic units within the previously delineated broad boundaries might cause a decrement of classification accuracy.

Accuracy estimations of all the classified datasets are higher in the training area compared to the validation area. This is the indication of compositional variations in the north-south trending lithostratigraphic units of the northern Coongan greenstone belt. Some of the lithologic units of the study area are not continuous from north to south, although most of them do. So the wide gap between the accuracy estimations of the training and validation areas is due to compositional differences between the lithological units. The compositional differences can be primary and/or secondary types (i.e., original compositional variations or variations resulted from geomorphologic activities).

7.1.4. Are there any indications of hydrothermal alteration processes? What are the unique characteristics of hydrothermal alteration minerals in different datasets?

In this study, the Duffer formation is designated as a hydrothermally altered unit. Non-usual enrichment/depletion of potassium content, enrichment of clay minerals, the occurrence of volcanogenic massive sulphides and chert units are the unique characteristics of hydrothermal alteration. Clay minerals, chert layers, and volcanogenic massive sulphides occur in the Duffer formation of the study area. The gamma-ray data did not indicate any unique features in the Duffer formation. Nevertheless, the AIOH bearing minerals, frequently interbedded chert layers, and gossanous rocks in the Duffer formation can be possible indications of hydrothermal alteration.

7.1.5. How does the data integration approach can improve the lithostratigraphic interpretation of the study area?

Integration of remote sensing and gamma-ray data with geological field studies was able to improve the lithostratigraphic interpretation of the northern Coongan greenstone belt by adding more details, by delineating accurate lithological boundaries and by determining the prominent areas of hydrothermal alteration. Integration of the relatively higher resolution remote sensing data with field observation points was able to determine the thin chert layers interbedded with all stratigraphic units of the study area. Similarly,

integration of aster data showing AlOH bearing minerals, Sentinel-2 data indicating the occurrence of iron oxides, and an aerial photograph showing gossanous features was able to determine the possible indications of hydrothermal alteration.

7.2. Recommendations

Further studies are recommended, especially in the prominent hydrothermally altered unit (i.e., duffer formation). Characterizing the assemblage of clay minerals might help in confirming whether the Duffer formation is hydrothermally altered or surface hydration and oxidation processes were responsible for the formation of clays. However, the multispectral image used in this study is not very suited to identify individual minerals. Analyzing the chemistry of the altered versus non-altered minerals is also important in determining the true source of clay minerals.

LIST OF REFERENCES

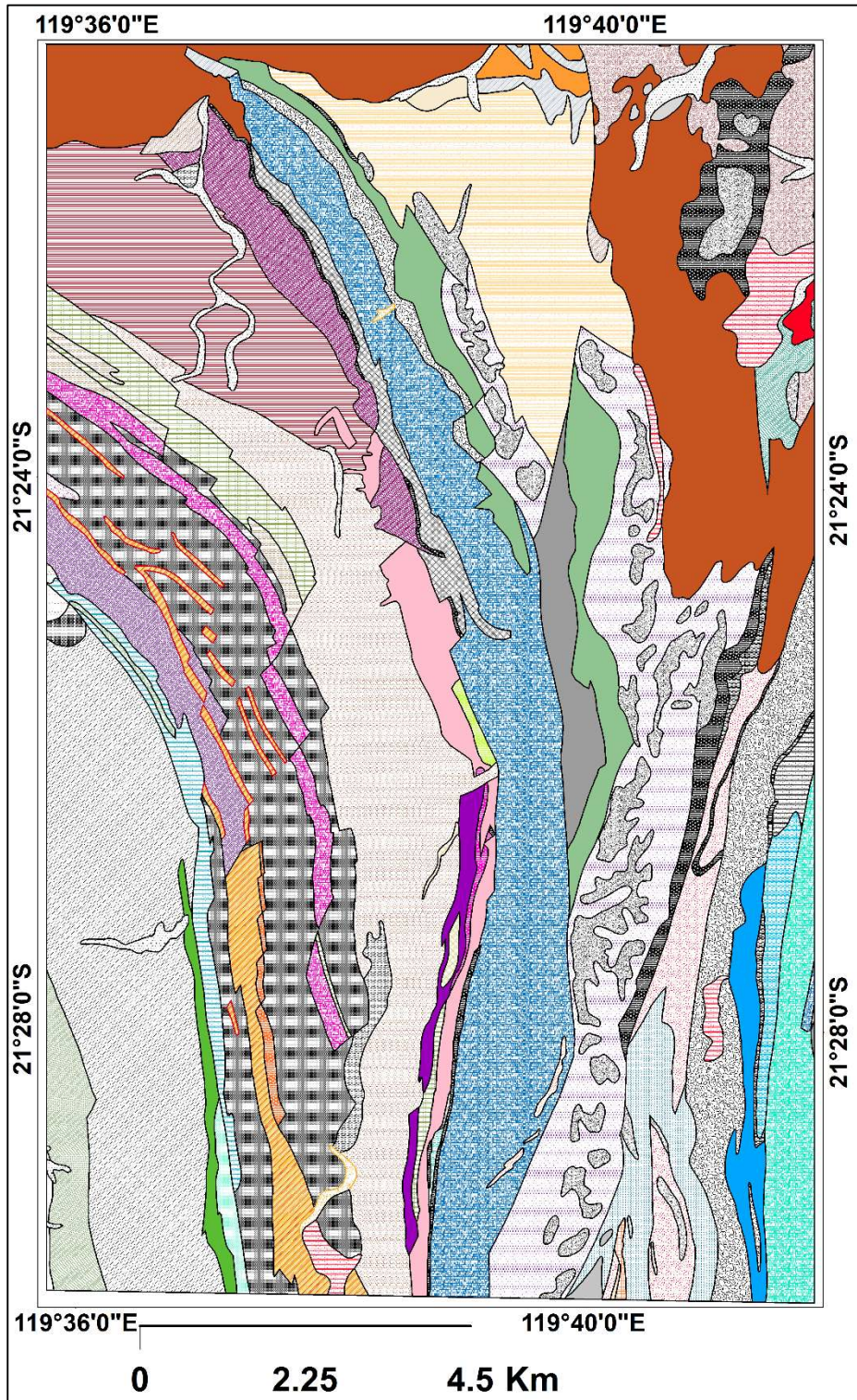
- Al-Nahmi, F., Saddiqi, O., Hilali, A., Rhinane, H., Baiddar, L., El Arabi, H., & Khanbari, K. (2017). Application of Remote sensing in Geological Mapping, Case Study Al Maghrabah Area- Hajjah Region, Yemen. In ISPRS Annals of the Photogrammetry, Remote Sensing and Spatial Information Sciences (Vol. 4, pp. 63–71). Safranbolu, Karabuk. <https://doi.org/10.5194/isprs-annals-IV-4-W4-63-2017>
- Anhaeusser, C. R. (2014). Archaean greenstone belts and associated granitic rocks - A review. *Journal of African Earth Sciences*, 100(December), 684–732. <https://doi.org/10.1016/j.jafrearsci.2014.07.019>
- Barnes, S. J., & Roeder, P. L. (2001). The Range of Spinel Compositions in Terrestrial Mafic and Ultramafic Rocks. *Journal of Petrology*, 42(12), 2279–2302. <https://doi.org/10.1093/petrology/42.12.2279>
- Brown, A. J., Cudahy, T. J., & Walter, M. R. (2006). Hydrothermal alteration at the Panorama Formation, North Pole Dome, Pilbara Craton, Western Australia. *Precambrian Research*, 151(3–4), 211–223. <https://doi.org/10.1016/j.precamres.2006.08.014>
- Brown, A. J., Walter, M. R., & Cudahy, T. J. (2005). Hyperspectral imaging spectroscopy of a Mars analog environment at the North Pole Dome, Pilbara Craton, Western Australia. *Australian Journal of Earth Sciences*, 52, 353–364. <https://doi.org/10.1080/08120090500134530>
- Buick, R., & Dunlop, J. S. R. (1990). Evaporitic sediments of Early Archaean age from the Warrawoona Group, North Pole, Western Australia. *Sedimentology*, 37(2), 247–277. <https://doi.org/10.1111/j.1365-3091.1990.tb00958.x>
- Chiozzi, P., Pasquale, V., & Verdoya, M. (2007). Radiometric survey for exploration of hydrothermal alteration in a volcanic area. *Journal of Geochemical Exploration*, 93(1), 13–20. <https://doi.org/10.1016/j.gexplo.2006.07.002>
- Congalton, R. G. (1991). A review of assessing the accuracy of classifications of remotely sensed data. *Remote Sensing Environment*, (37), 35–46.
- Cudahy, T. (2012). ASTER Geoscience Product Notes for Australia (No. EP-30-07-12-44) (Vol. 1). Retrieved from http://c3dmm.csiro.au/Australia_ASTER/Australian_ASTER_Geoscience_Product_Notes_FINALx.pdf
- Dentith, M., & Mudge, S. (2014). *Geophysics for the mineral exploration geoscientist*. Cambridge University Press (first edit). Perth: Cambridge University Press. <https://doi.org/https://doi.org/10.1017/CBO9781139024358.002>
- Earth Remote Sensing Data Analysis Center. (2003). ASTER Reference Guide, Version 1.0. NASA. Retrieved from https://unit.aist.go.jp/igg/rs-rg/ASTERSciWeb_AIST/en/documnts/pdf/ASTER_Ref_V1.pdf
- Elawadi, E., Ammar, A., & Elsirafy, A. (2004). Mapping surface geology using airborne gamma-ray spectrometric survey data - A case study. (and A. E. Eslam Elawadi, Ahmed Ammar, Ed.), *Nuclear Materials Authority of Egypt, Airborne Exploration Dept.*, (November), 7. Retrieved from <https://www.researchgate.net/publication/259822736>
- European Space Agency. (2015). *Sentinel-2 User Handbook*. ESA. Retrieved from https://sentinel.esa.int/documents/247904/685211/Sentinel-2_User_Handbook
- Ford, K., Harris, J. R., Shives, R., Carson, J., & Buckle, J. (2008). Remote predictive mapping 2. Gamma-ray spectrometry: A tool for mapping Canada's North. *Geoscience Canada*, 35(3–4), 109–126. Retrieved from <https://www.researchgate.net/publication/285872174>
- Geoscience Australia and Australian Stratigraphy Commission. (2017). *Australian Stratigraphic Units Database*. Retrieved June 10, 2020, from <https://asud.ga.gov.au/search-stratigraphic-units/results/26238>
- Geoscience Australia and Australian Stratigraphy Commission. (2017). *Australian Stratigraphic Units Database*. Retrieved May 14, 2020, from <https://asud.ga.gov.au/search-stratigraphic-units>
- Gillings, A. (1996). Evolution of hydrothermal ecosystems on earth (and Mars?). *BioEssays*, 18(6), 515–517. <https://doi.org/10.1002/bies.950180614>
- Gordon, H. R., & Morel, A. Y. (1983). Atmospheric Correction. In Harris Geospatial Solutions, Inc. (pp. 68–71). Retrieved from <https://www.harrisgeospatial.com/docs/AtmosphericCorrection.html#Log>
- Haldar, S. K. (2018). Economic Mineral Deposits and Host Rocks. In A. Shapiro (Ed.), *Mineral Exploration, Principles and Applications* (second edi, pp. 25–45). Kolkata: Elsevier.

- <https://doi.org/https://doi.org/10.1016/B978-0-12-814022-2.00002-2>
Harris Geospatial Solutions, I. (2020). SMACC. Retrieved April 21, 2020, from <https://www.harrisgeospatial.com/docs/SMACC.html>
- Hecker, C., Ruitenbeek, F. J. A. Van, Werff, H. M. A. Van Der, Bakker, W. H., Hewson, D., & Meer, F. D. Van Der. (2017). Spectral absorption feature analysis for geological remote sensing applications.
- Hein, K. A. A., Leeuw, G. A. M. de, Scherrenberg, A. F., Wijbrans, J. R., & S., W. (n.d.). Volcano-sedimentary stratigraphy of the northern Coongan Greenstone Belt, East Pilbara Granite-Greenstone Terrain, Australia. un-published work.
- Hickman, A. H., & Van Kranendonk, M. J. (2012). Early Earth evolution: evidence from the 3.5-1.8 Ga geological history of the Pilbara region of Western Australia. *Geological Survey of Western Australia*, 35(1), 283–297. Retrieved from https://www.aca.unsw.edu.au/sites/default/files/publications/Pilbara_Episodes_2012.pdf
- Hickman AH, Van Kranendonk, M. (2008). Marblebar_2855.pdf. Geological Survey of Western Australia, 119. Retrieved from <https://geodocs.dmirns.wa.gov.au/Web/documentlist/3/Combined/P00AY>
- Huston, D., Blewett, R., Mernaugh, T., Sun, S.-S., & Kamprad, J. (2000). Gold deposits of the Pilbara craton: Results of AGSO Research 1998-2000. AGSO-Geoscience Australia, Record. Canberra.
- Kokaly, R. F., Clark, R. N., Swayze, G. A., Livo, K. E., Hoefen, T. M., Pearson, N. C., ... Klein, and A. J. (2017). USGS Spectral Library Version 7. U.S. Geological Survey Data Series 1035, 61 P. <https://doi.org/10.3133/ds1035>.
- Maden, N., & Akaryali, E. (2015). Gamma-ray spectrometry for recognition of hydrothermal alteration zones related to a low sulfidation epithermal gold mineralization (eastern Pontides, NE Türkiye). *Journal of Applied Geophysics*, 122, 74–85. <https://doi.org/10.1016/j.jappgeo.2015.09.003>
- Nicolet, J.-P., & Erdi-Krausz, G. (2003). Guidelines for radioelement mapping using gamma ray spectrometry data. *International Atomic Energy Agency*, 4(July), 1549-1555.
- Pirajno, F. (2010). *Hydrothermal Processes and Mineral Systems*. (P. A. Cawood, Ed.) (resvised e). Perth: Geological Survey of Western Australia. <https://doi.org/2008933283>
- Richards, J. A., & Jia, X. (2006). *Remote Sensing Digital Image Analysis*. Springer-Verlag. Berlin/Heidelberg: Springer-Verlag. <https://doi.org/10.1007/3-540-29711-1>
- Richardson, L. M. (1997). Marble Bar (Marble Bar, western Port Hedland, eastern Roebourne, and northeastern Pyramid 1:250 000 sheet areas) airborne geophysical survey, 1996 : operations report. Canberra. Retrieved from <https://catalogue.nla.gov.au/Record/1808940>
- Scherrenberg, A. F., Hein, K. A. A., & White, S. (2004). Middle Archaean gold deposits in the North Shaw-Coongan Greenstone Belt, Australia: The relative timing of events responsible for gold mineralization. *Ore Geology Reviews*, 25, 175–197. <https://doi.org/10.1016/j.oregeorev.2004.04.001>
- Schetselaar, E. M., Chung, C. J. F., & Kim, K. E. (2000). Integration of landsat TM, gamma-ray, magnetic, and field data to discriminate lithological units in vegetated granite-gneiss terrain. *Remote Sensing of Environment*, 71(1), 89–105. [https://doi.org/10.1016/S0034-4257\(99\)00069-3](https://doi.org/10.1016/S0034-4257(99)00069-3)
- Shanks, W. C. (Pat). (2012). Hydrothermal Alteration in Volcanogenic Massive Sulfide Occurrence Model. US Geological Survey Scientific Investigations Report 2010–5070–C, 107(5), 1073–1073. <https://doi.org/10.2113/econgeo.107.5.1073>
- Slavinski, H., Morris, B., Ugalde, H., Spicer, B., Skulski, T., & Rogers, N. (2010). Integration of lithological, geophysical, and remote sensing information: a basis for remote predictive geological mapping of the Baie Verte Peninsula, Newfoundland. *Canadian Journal of Remote Sensing*, 36(2), 99–118. <https://doi.org/10.5589/m10-031>
- Solomon, M., Tornos, F., Large, R. R., Badham, J. N. P., Both, R. A., & Zaw, K. (2004). Zn-Pb-Cu volcanic-hosted massive sulfide deposits: Criteria for distinguishing brine pool-type from black smoker-type sulfide deposition. *Ore Geology Reviews*, 25, 259–283. <https://doi.org/10.1016/j.oregeorev.2004.01.003>
- Testa, F. J., Villanueva, C., Cooke, D. R., & Zhang, L. (2018). Lithological and hydrothermal alteration mapping of epithermal, porphyry and tourmaline breccia districts in the argentine andes using ASTER imagery. *Remote Sensing*, 10(2), 1–45. <https://doi.org/10.3390/rs10020203>
- Van der Meer, F. D., van der Werff, H. M. A., & van Ruitenbeek, F. J. A. (2014). Potential of ESA's Sentinel-2 for geological applications. *Remote Sensing of Environment*, 148, 124–133. <https://doi.org/https://doi.org/10.1016/j.rse.2014.03.022>
- van der Werff, H., & van der Meer, F. (2015). Sentinel-2 for mapping iron absorption feature parameters. *Remote Sensing*, 7, 12635–12653. <https://doi.org/https://doi.org/10.3390/rs71012635>

- Van Kranendonk, M. J. (2006). Volcanic degassing, hydrothermal circulation, and the flourishing of early life on Earth: A review of the evidence from c. 3490-3240 Ma rocks of the Pilbara Supergroup, Pilbara Craton, Western Australia. *Earth-Science Reviews*, 74, 197–240. <https://doi.org/10.1016/j.earscirev.2005.09.005>
- Van Kranendonk, M. J., Hickman, A. H., Smithies, R. H., & Nelson, D. R. (2002). Geology and tectonic evolution of the Archean North Pilbara Terrain, Pilbara Craton, Western Australia. *Economic Geology*, 97, 695–732. <https://doi.org/10.2113/gsecongeo.97.4.695>
- Wilford, J. R., Bierwirth, P. N., & Craig, M. A. (1997). Application of airborne gamma-ray spectrometry in soil/regolith mapping and applied geomorphology. *AGSO Journal of Australian Geology & Geophysics*, 17(2), 201–216. Retrieved from https://d28rz98at9flks.cloudfront.net/81503/Jou1997_v17_n2_p201.pdf
- Yong-gui, Z., Zheng-le, C., Xing-tong, C., & Bai-lin, C. (2014). Alteration zone mapping for detecting potential mineralized areas in Kaladawan of north altyn tagh using ASTER data. In *IOP Conference Series: Earth and Environmental Science* (Vol. 17 012173). Beijing. <https://doi.org/10.1088/1755-1315/17/1/012173>
- Youssef, M. A. S., & Elkhodary, S. T. (2013). Utilization of airborne gamma-ray spectrometric data for geological mapping, radioactive mineral exploration, and environmental monitoring of southeastern Aswan city, South Eastern Desert, Egypt. *Geophysical Journal International*, 195(3), 1689–1700. <https://doi.org/https://doi.org/10.1093/gji/ggt375>
- Zegers, T. E. (1996). Structural, kinematic, and metallogenic evolution of selected domains of the Pilbara granitoid-greenstone terrain. Utrecht University. Retrieved from <https://www.amazon.com/Structural-kinematic-metallogenic-evolution-granitoid-greenstone/dp/9057440040>

[APPENDICES](#)

[Appendix 1](#): 1:100,000 scale geological map by (Hickman AH, Van Kranendonk, 2008)



Legend of the geological map

Legend											
	A-CDI-st		A-FOR-bbg		A-KEE-uk		A-WAa-od		A-WAm-bkd		_A2-d-k
	A-CLco-mgg		A-FOR-od		A-KEw-cc		A-WAd-fds		A-WAm-ccj		_C1
	A-DA-mads		A-GCe-cc		A-KEw-fnm		A-WAd-fdx		A-WAm-od		_C2
	A-DA-mapt		A-GCe-ci		A-KEw-fnt		A-WAd-fnt		A-WAm-uk		_R1-k
	A-DA-mats		A-GCf-stq		A-KEw-fr		A-WAd-gmap		A-WAn-mb		_R3-f
	A-DA-mogl		A-KEE-bb		A-KEw-frtz		A-WAd-shi		A-WAn-mba		_R3r-f
	A-EM-mgms		A-KEE-bbo		A-KEw-mh		A-WAdm-ccj		A-WAp-frp		_W1
	A-FOb-sc		A-KEE-bk		A-KEw-mls		A-WAh-bko		A-WAp-frtt		zq
	A-FOb-sp		A-KEE-cc		A-KEw-sh		A-WAh-mbms		A-WAp-mfs		
	A-FOh-st		A-KEE-mbmk		A-KEw-shz		A-WAh-mutk				_A1
	A-FOk-bb		A-KEE-mc		A-Pls-kdz		A-WAm-bb				_A1c
	A-FOk-bbo		A-KEE-od		A-Pls-xs-c		A-WAm-bk				_A2

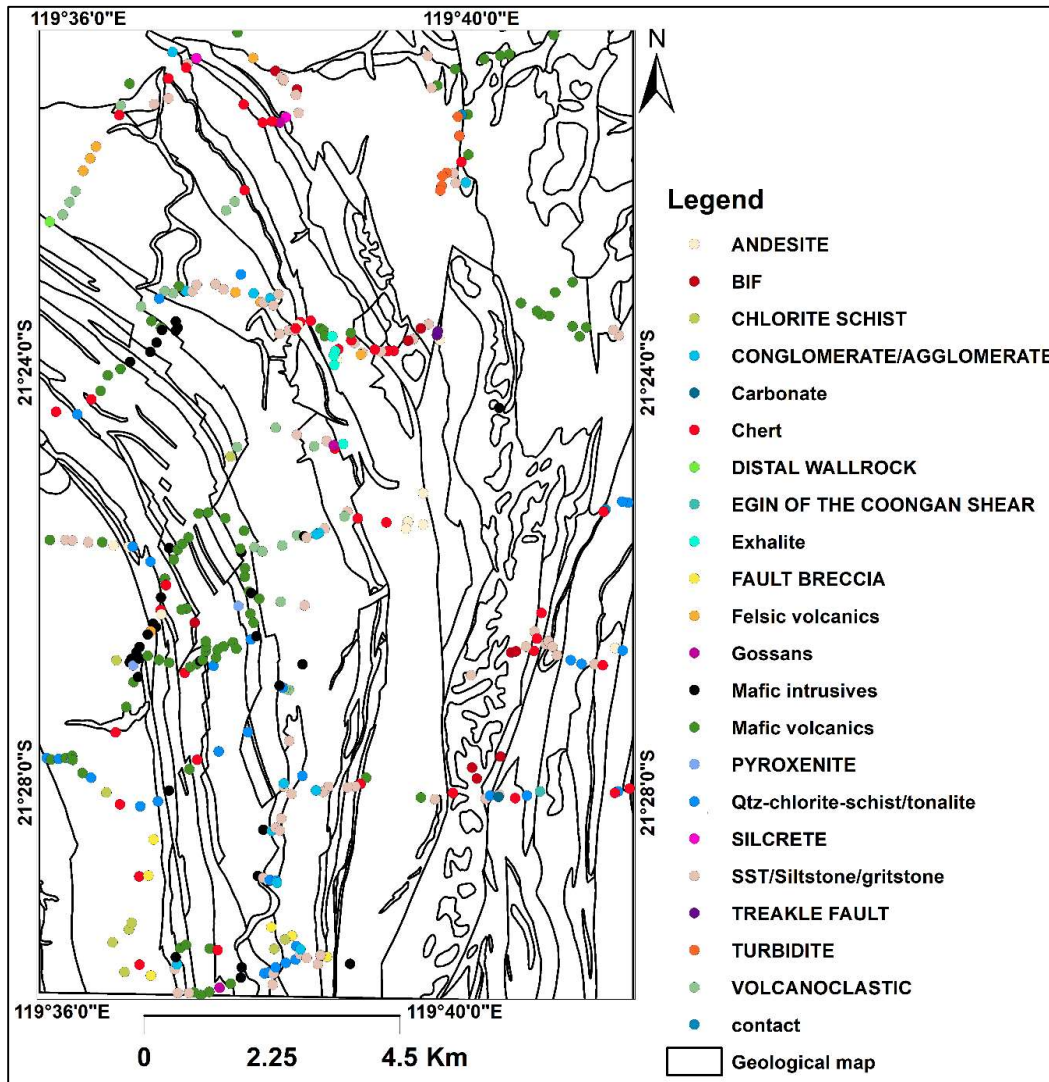
Legend description of the geological map in Appendix of 1

GEOOBS_	GEOOBS_I	CODE	JNCODE	NARRATIVE	REGOLITH	SUPERGRG	GROUP	FORMATIC	ION	ERA	PERIOD
2095	2374	_A1	2855;_A1	Sand, clay, silt, and gravel in active drainage areas	Alluvial uni					PHANERO; CENOZOIC	QUATERN
1648	1927	_A1c	2855;_A1c	Sand, silt, and gravel in active drainage channels; includes clay, silt, and sand in poorly defined drainage courses on flo	Alluvial uni					PHANERO; CENOZOIC	QUATERN
1903	2182	_A2	2855;_A2	Consolidated alluvial sand, silt, and gravel; dissected by present-day drainage	Alluvial uni					PHANERO; CENOZOIC	
1905	2184	_A2-d-k	2855;_A2-	Consolidated alluvial gravel, sand, and silt; local carbonate cement; dissected by present-day drainage	Alluvial uni					PHANERO; CENOZOIC	
1814	2093	_C1	2855;_C1	Colluvial sand, silt, and gravel in outwash fans; scree and talus; proximal mass-wasting deposits; unconsolidated	Colluvial u					PHANERO; CENOZOIC	QUATERN
2020	2299	_C2	2855;_C2	Partly consolidated colluvial sand, silt, and gravel in proximal outwash fans; scree and talus; dissected by present-day	Colluvial u					PHANERO; CENOZOIC	
1964	2243	_R1-k	2855;_R1-	Residual calcrete; massive, nodular, and cavernous limestone; variably silicified	Residual u					PHANERO; CENOZOIC	QUATERN
1929	2208	_R3-f	2855;_R3-	Ferruginous duricrust and ferruginous colluvium; locally includes ferruginous alluvium; consolidated to partly consolid	Residual u					PHANERO; CENOZOIC	
1957	2236	_R3r-f	2855;_R3r-	Ferruginous duricrust; includes massive, pisolitic, and nodular ferricrete; locally underlies OAKOVER FORMATION	Residual u					PHANERO; CENOZOIC	
1897	2176	_W1	2855;_W1	Silt, sand, and pebbles in distal sheetwash fans; no defined drainage	Sheetwash					PHANERO; CENOZOIC	QUATERN
1895	2174	A-CDl-st	2855;A-CD	sandstone with beds of conglomerate, and minor siltstone and shale; metamorphosed		De Grey St	Croydon G			ARCHEAN	
2544	2823	A-CLco-mg	2855;A-CL	Metagranodiorite to metatonalite; clotty hornblende textured; strongly foliated		Callina Sup				ARCHEAN	
2884	3163	A-DA-mad	2855;A-DA	Metadunite, schistose						ARCHEAN	
2433	2712	A-DA-map	2855;A-DA	Metaperidotite and serpentine-chlorite schist		Dalton Sup				ARCHEAN	
2671	2950	A-DA-mat	2855;A-DA	Serpentinite, schistose						ARCHEAN	
2912	3191	A-DA-mog	2855;A-DA	Metaleucogabbro						ARCHEAN	
2597	2876	A-EM-mgn	2855;A-EM	Strongly foliated to schistose metamonzogranite; fine to medium grained		Emu Pool				ARCHEAN	
1870	2149	A-FOb-sc	2855;A-FO	Conglomerate, pebbly sandstone, and sandstone; dominantly chert and quartz clasts; locally silicified		Mount Bru Fortescue				ARCHEAN	
1922	2201	A-FOb-sp	2855;A-FO	Sandstone, pebbly sandstone, and minor conglomerate; dominantly chert and quartz clasts; locally silicified		Mount Bru Fortescue				ARCHEAN	
2094	2373	A-FOh-st	2855;A-FO	Sandstone; coarse- to medium grained; generally arkosic, but includes local volcanoclastic sandstone and siltstone		Mount Bru Fortescue	HARDEY FC			ARCHEAN	
2144	2423	A-FOk-bb	2855;A-FO	Massive and vesicular tholeiitic basaltic andesite; thick flows		Mount Bru Fortescue	KYLENA FC			ARCHEAN	
2390	2669	A-FOk-bbc	2855;A-FO	Pillow basalt		Mount Bru Fortescue	KYLENA FC			ARCHEAN	
1394	1644	A-FOr-bbg	2855;A-FO	Massive porphyritic vesicular and amygdaloidal basalt; some pillow basalt		Mount Bru Fortescue	MOUNT R			ARCHEAN	
1856	2135	A-FOr-od	2855;A-FO	Dolerite		Mount Bru Fortescue	MOUNT R			ARCHEAN	
1848	2127	A-GCe-cc	2855;A-GC	Chert; white and grey; locally banded; minor jaspilite and iron formation; metamorphosed		De Grey St Gorge Cre	CLEAVERV			ARCHEAN	
2055	2334	A-GCe-ci	2855;A-GC	Banded iron-formation and ferruginous chert; local banded quartz-magnetite-grunerite rock; metamorphosed		De Grey St Gorge Cre	CLEAVERV			ARCHEAN	
2350	2629	A-GCF-stq	2855;A-GC	<Null>	<Null>	<Null>	<Null>	<Null>	<Null>	<Null>	<Null>
2181	2460	A-KEe-bb	2855;A-KE	Massive basalt; metamorphosed		Pilbara Sup Kelly Grou				ARCHEAN	
2478	2757	A-KEe-bbo	2855;A-KE	Pillowed basalt; includes local massive basalt, dolerite, and komatiitic basalt; metamorphosed		Pilbara Sup Kelly Grou				ARCHEAN	
1902	2181	A-KEe-bk	2855;A-KE	Komatiitic basalt, massive and pillowed lavas and subvolcanic intrusions; local pyroxene spinifex texture; metamorph		Pilbara Sup Kelly Grou				ARCHEAN	
2195	2474	A-KEe-cc	2855;A-KE	Chert; metamorphosed		Pilbara Sup Kelly Grou				ARCHEAN	
2312	2591	A-KEe-mbr	2855;A-KE	Carbonate-altered and silicified, fine- to medium-grained mafic schist after komatiitic basalt		Pilbara Sup Kelly Grou				ARCHEAN	
2477	2756	A-KEe-mc	2855;A-KE	Metachert; includes grey and white layered quartzite derived from chert		Pilbara Sup Kelly Grou				ARCHEAN	
2625	2904	A-KEe-od	2855;A-KE	Dolerite; includes local gabbro; metamorphosed		Pilbara Sup Kelly Grou				ARCHEAN	
1954	2233	A-KEe-uk	2855;A-KE	Komatiite with pyroxene spinifex texture; local talc-carbonate rock; metamorphosed		Pilbara Sup Kelly Grou				ARCHEAN	
2620	2899	A-KEw-cc	2855;A-KE	Chert; metamorphosed		Pilbara Sup Kelly Grou	WYMAN F			ARCHEAN	
2759	3038	A-KEw-fnn	2855;A-KE	Interbedded felsic volcanic siltstone, sandstone, conglomerate, and shale		Pilbara Sup Kelly Grou	WYMAN F			ARCHEAN	
1890	2169	A-KEw-fnt	2855;A-KE	Felsic volcanic sandstone; tuffaceous; local quartz sandstone; metamorphosed		Pilbara Sup Kelly Grou	WYMAN F			ARCHEAN	
1908	2187	A-KEw-fr	2855;A-KE	Porphyritic rhyolite and rhyodacite; local felsic volcanoclastic rocks; metamorphosed		Pilbara Sup Kelly Grou	WYMAN F			ARCHEAN	
1918	2197	A-KEw-frtz	2855;A-KE	Fine-grained, grey bedded chert derived from silicified felsic ash; metamorphosed		Pilbara Sup Kelly Grou	WYMAN F			ARCHEAN	
2594	2873	A-KEw-mh	2855;A-KE	Interlayered psammitic and pelitic rocks; metamorphosed shale, siltstone, and sandstone		Pilbara Sup Kelly Grou	WYMAN F			ARCHEAN	
2548	2827	A-KEw-mls	2855;A-KE	Pelitic schist; metamorphosed shale and minor siltstone		Pilbara Sup Kelly Grou	WYMAN F			ARCHEAN	

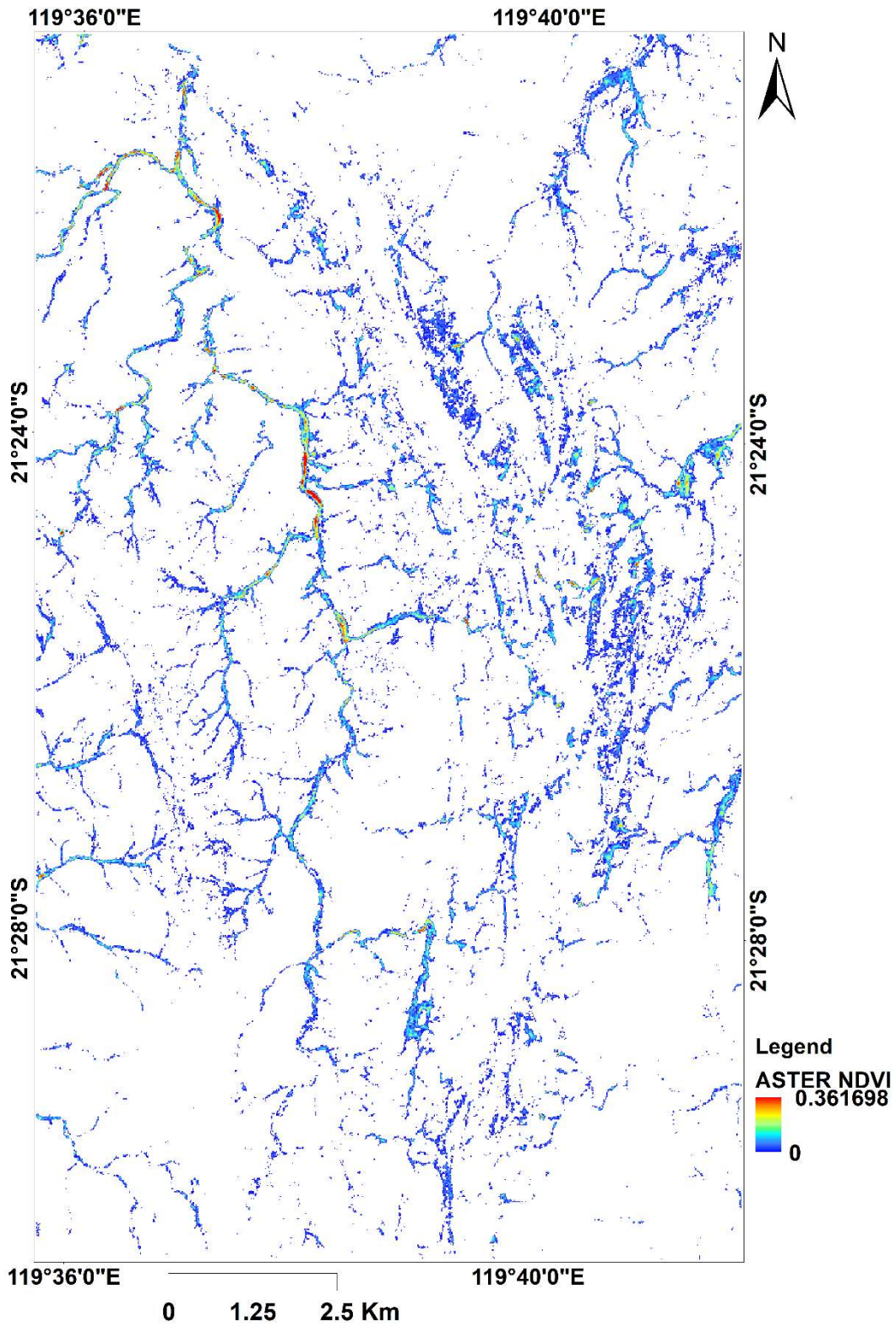
DATA INTEGRATION FOR RECONSTRUCTING OF VOLCANO-SEDIMENTARY SEQUENCES IN COONGAN GREENSTONE BELT EASTERN PILBARA CRATON, WESTERN AUSTRALIA

2872	3151	A-KEw-shz	2855;A-KE	Grey and white chert after shale and fine-grained felsic tuff; metamorphosed	Pilbara Sup	Kelly Group	WYMAN F	ARCHEAN
1930	2209	A-Pls-kdz	2855;A-Pls	White, grey, and blue-black layered chert after dolomite; locally stromatolitic; metamorphosed	Pilbara Sup		STRELLEY	ARCHEAN
2466	2745	A-Pls-xs-c	2855;A-Pls	Sandstone, conglomerate, chert, and silicified carbonate rocks; local silicified volcanic rocks; stromatolitic; metamorphosed	Pilbara Sup		STRELLEY	ARCHEAN
1945	2224	A-WAa-od	2855;A-W	Fine- to medium-grained dolerite; metamorphosed	Pilbara Sup			ARCHEAN
2105	2384	A-WAd-fds	2855;A-W	Dacitic volcanic breccia, sandstone and tuff; metamorphosed	Pilbara Sup			ARCHEAN
1948	2227	A-WAd-fd	2855;A-W	Dacitic volcanic breccia; porphyritic dacite breccia in a dacitic matrix; local volcanoclastic sandstone, tuff, and conglomerate	Pilbara Sup			ARCHEAN
2032	2311	A-WAd-fnt	2855;A-W	Fine-grained felsic volcanic sandstone; local chert, wacke and conglomerate; thinly bedded; locally silicified; metamorphosed	Pilbara Sup			ARCHEAN
2159	2438	A-WAd-gr	2855;A-W	Quartz- and feldspar-porphyritic micromonzogranite; as subvolcanic intrusions; metamorphosed	Pilbara Sup			ARCHEAN
2516	2795	A-WAdm-c	2855;A-W	Jaspilitic chert; metamorphosed	Pilbara Sup			ARCHEAN
2527	2806	A-WAd-shi	2855;A-W	Shale with interbeds of red and white layered chert, grey tuffaceous sandstone, and iron-formation; metamorphosed	Pilbara Sup			ARCHEAN
2387	2666	A-WAh-bk	2855;A-W	Pillowed komatiitic basalt; metamorphosed	Pilbara Sup			ARCHEAN
2760	3039	A-WAh-mk	2855;A-W	Mafic schist derived from komatiitic basalt; carbonate-tremolite-chlorite rock	Pilbara Sup			ARCHEAN
2368	2647	A-WAh-mc	2855;A-W	Talc-carbonate and chlorite-serpentine-carbonate schist; metamorphosed ultramafic volcanic rocks	Pilbara Sup			ARCHEAN
2583	2862	A-WAm-bl	2855;A-W	Basalt; generally massive, but locally pillowed; local dolerite sills; metamorphosed	Pilbara Sup			ARCHEAN
2030	2309	A-WAm-bl	2855;A-W	Komatiitic basalt, massive and pillowed lavas; local pyroxene spinifex texture; metamorphosed	Pilbara Sup			ARCHEAN
2043	2322	A-WAm-bl	2855;A-W	Pillowed and variolitic komatiitic basalt; metamorphosed	Pilbara Sup			ARCHEAN
2581	2860	A-WAm-cc	2855;A-W	Red, white, and black layered jaspilitic chert; metamorphosed	Pilbara Sup			ARCHEAN
2190	2469	A-WAm-oc	2855;A-W	Dolerite and local gabbro; metamorphosed	Pilbara Sup			ARCHEAN
2084	2363	A-WAm-uk	2855;A-W	Komatiite, with pyroxene spinifex texture; local talc-carbonate rock; metamorphosed	Pilbara Sup			ARCHEAN
2398	2677	A-WAn-mk	2855;A-W	Metabasalt and metadolerite; local pillow structures	Pilbara Sup			ARCHEAN
2450	2729	A-WAn-mk	2855;A-W	Medium grained, foliated amphibolite and amphibolite schist	Pilbara Sup			ARCHEAN
2183	2462	A-WAp-frp	2855;A-W	Quartz-porphyritic rhyolite; locally schistose; metamorphosed	Pilbara Sup			ARCHEAN
2211	2490	A-WAp-frp	2855;A-W	Quartz-porphyritic rhyolite; locally schistose; metamorphosed	Pilbara Sup			ARCHEAN
1931	2210	A-WAp-frt	2855;A-W	Rhyolitic tuffaceous volcanoclastic sandstone, including ash beds; well bedded; metamorphosed	Pilbara Sup			ARCHEAN
2790	3069	A-WAp-mf	2855;A-W	Metafelsic volcanic rock; schistose	Pilbara Sup			ARCHEAN
2752	3031	zq	2855;zq	Quartz vein or pod; massive, crystalline, or brecciated; age uncertain				PROTEROZOIC

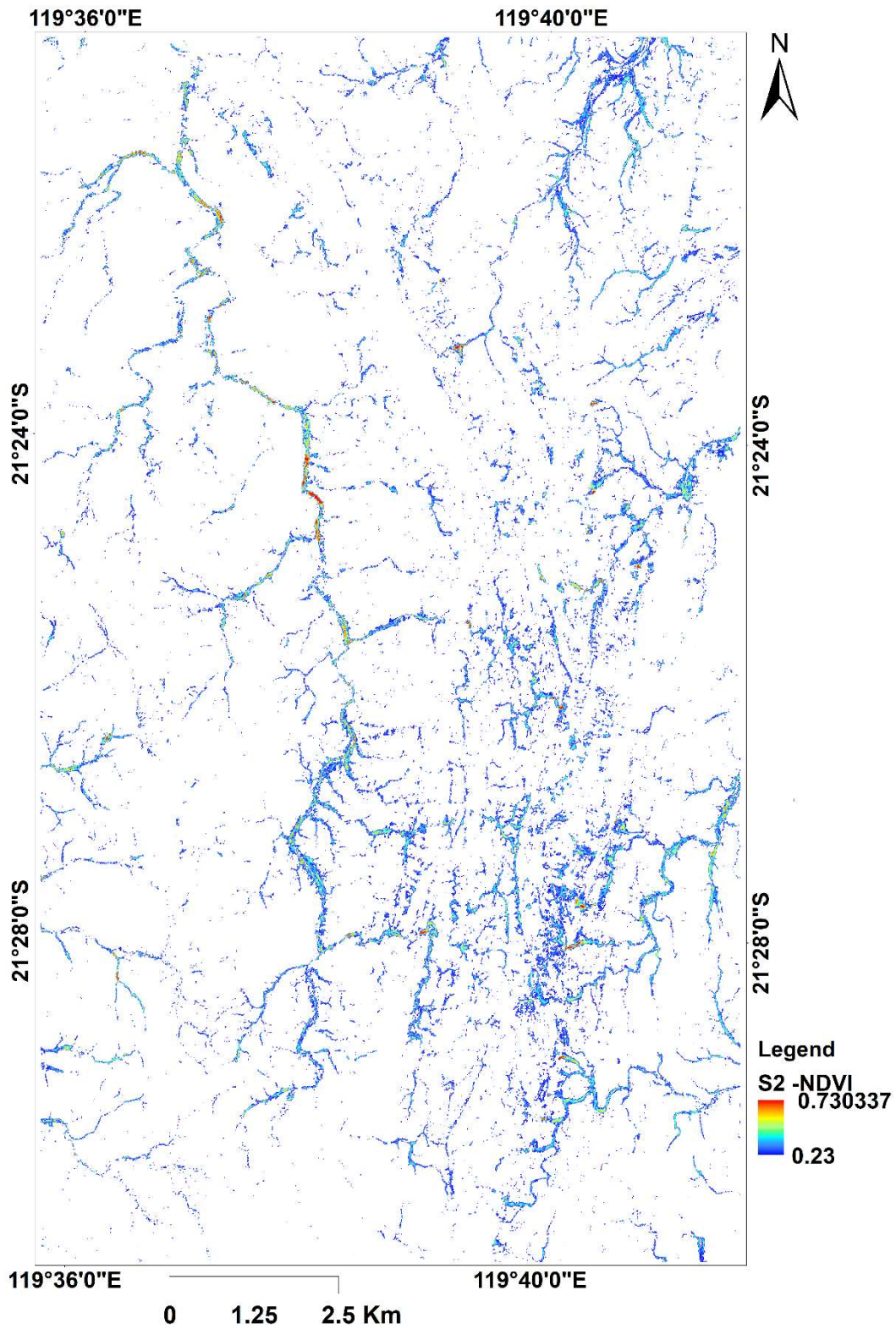
[Appendix 2](#): field observation data by Prof. dr. Kim.H, emeritus & visiting professor at the University of the Witwatersrand in South Africa.



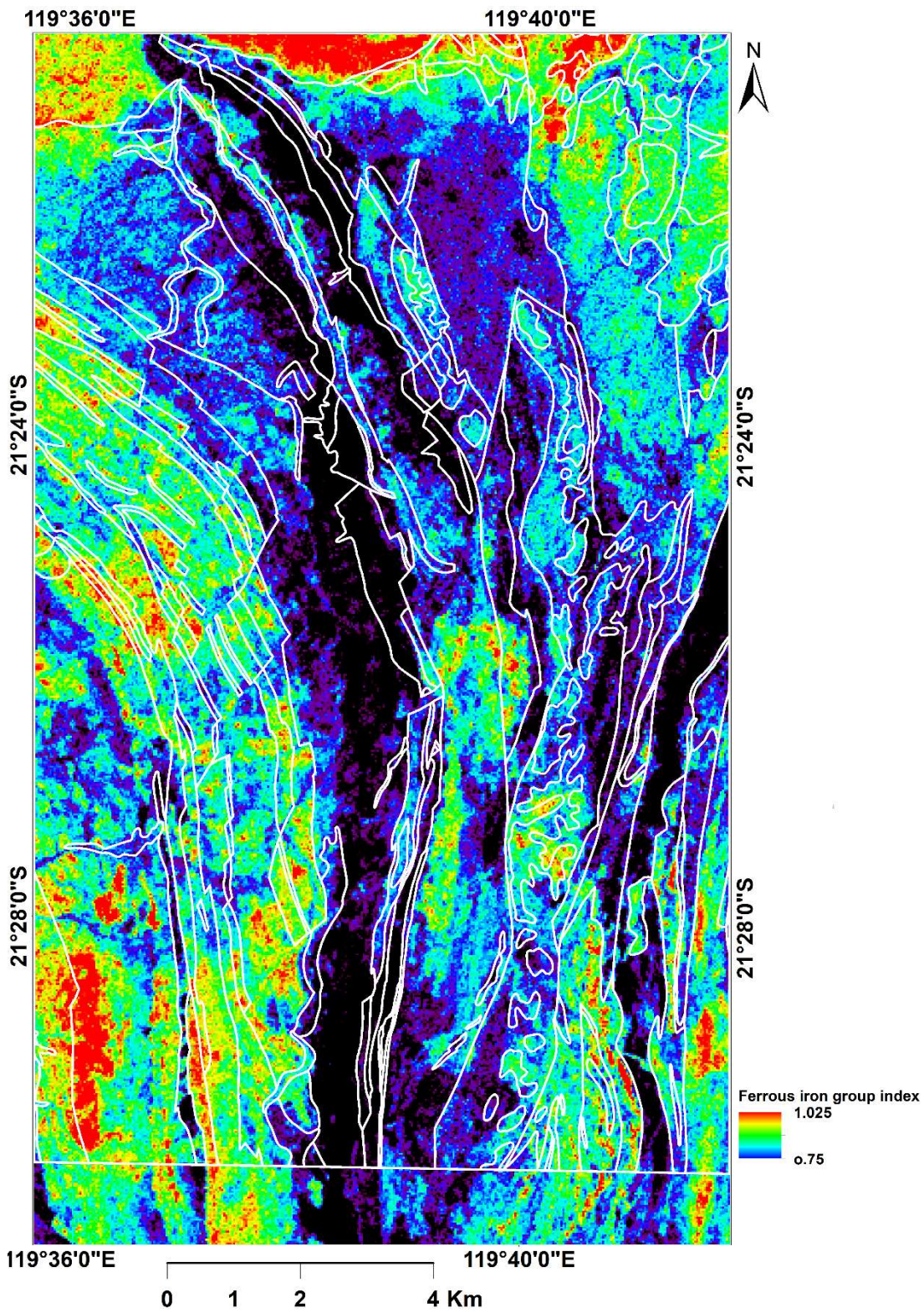
Appendix 3: ASTER NDVI



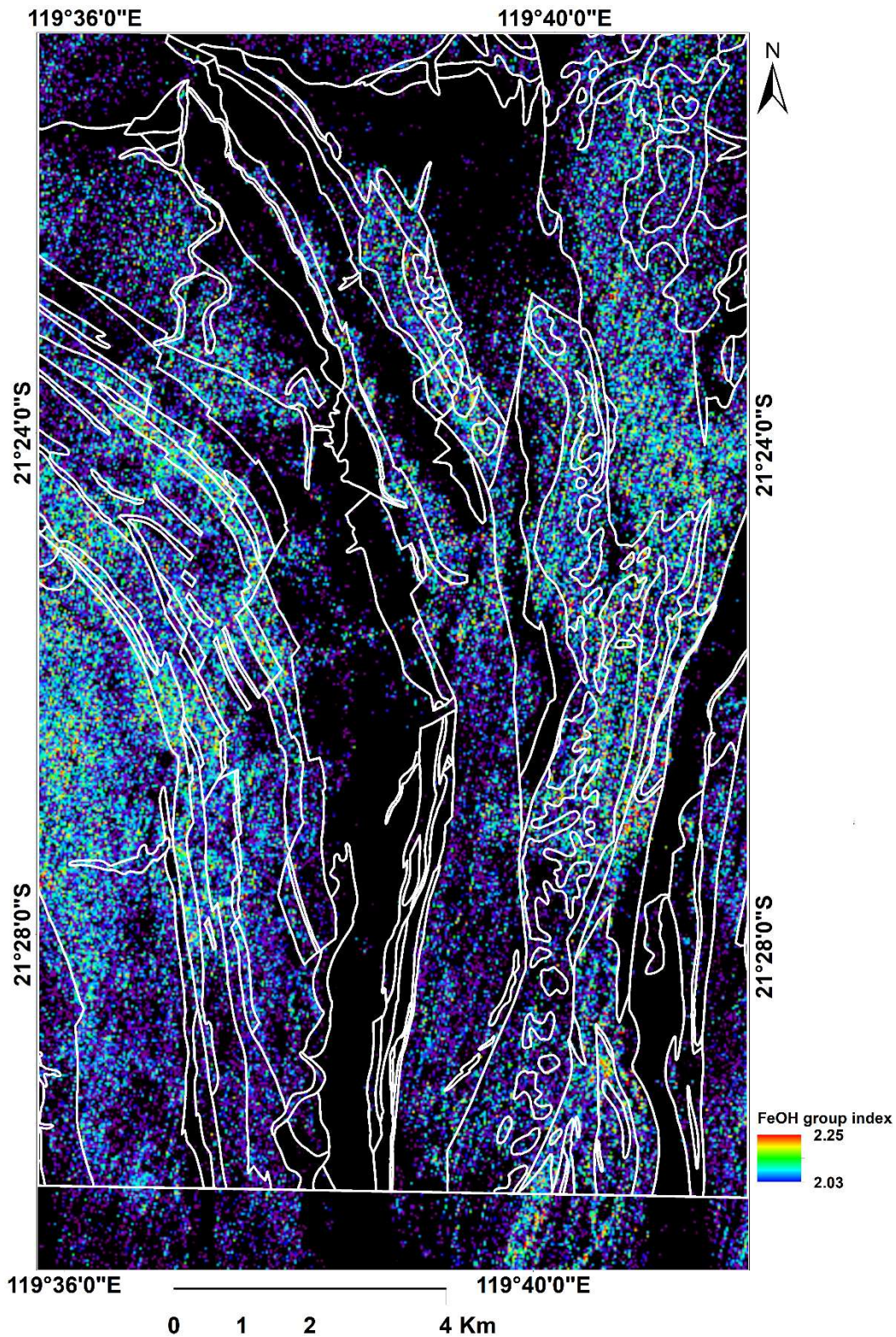
Appendix 4: Sentinel-2 NDVI



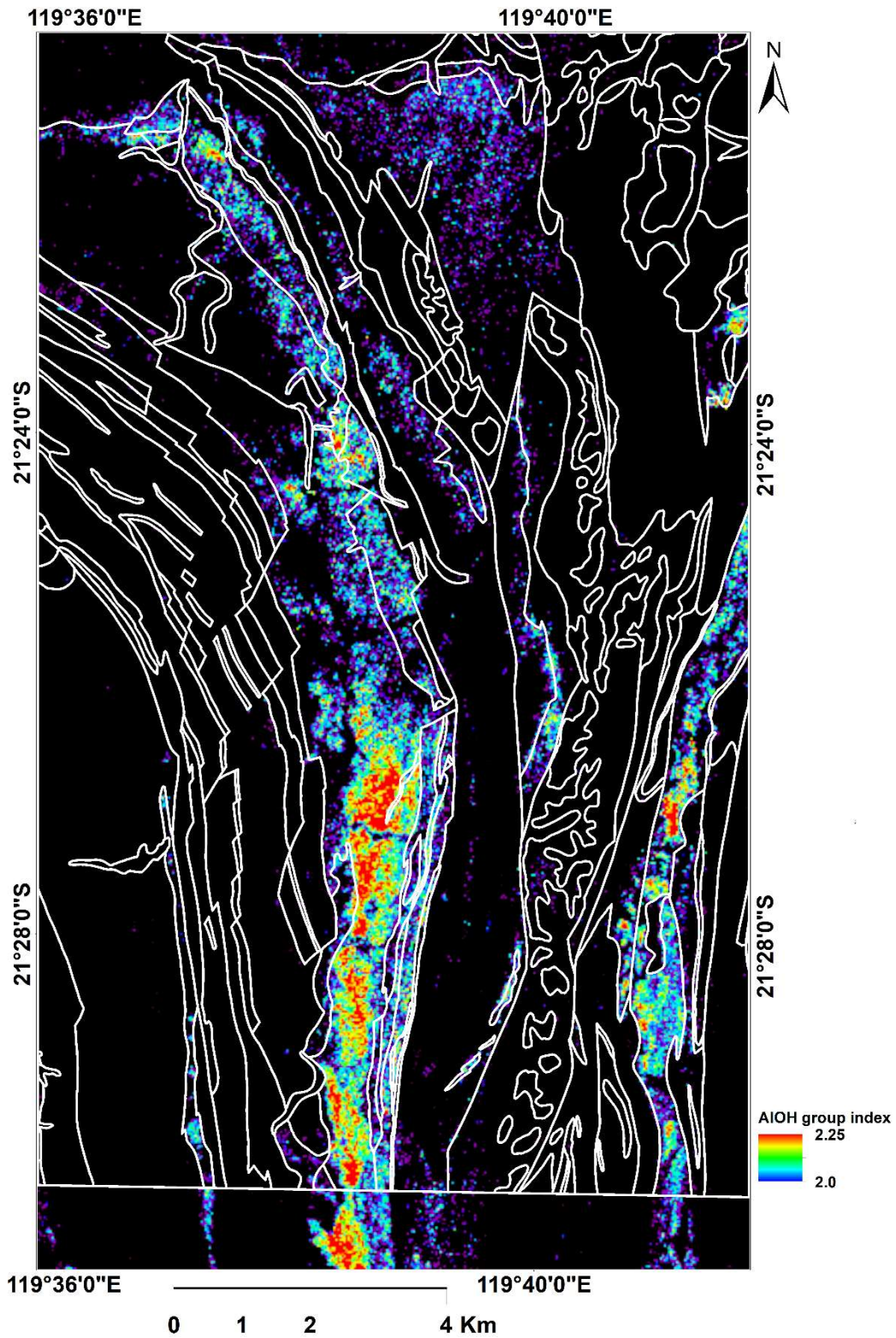
[Appendix 5](#): ASTER band ratio B5/B4 (ferrous iron group content in silicates/carbonates). The white lines are the lithological boundaries from the geological map.



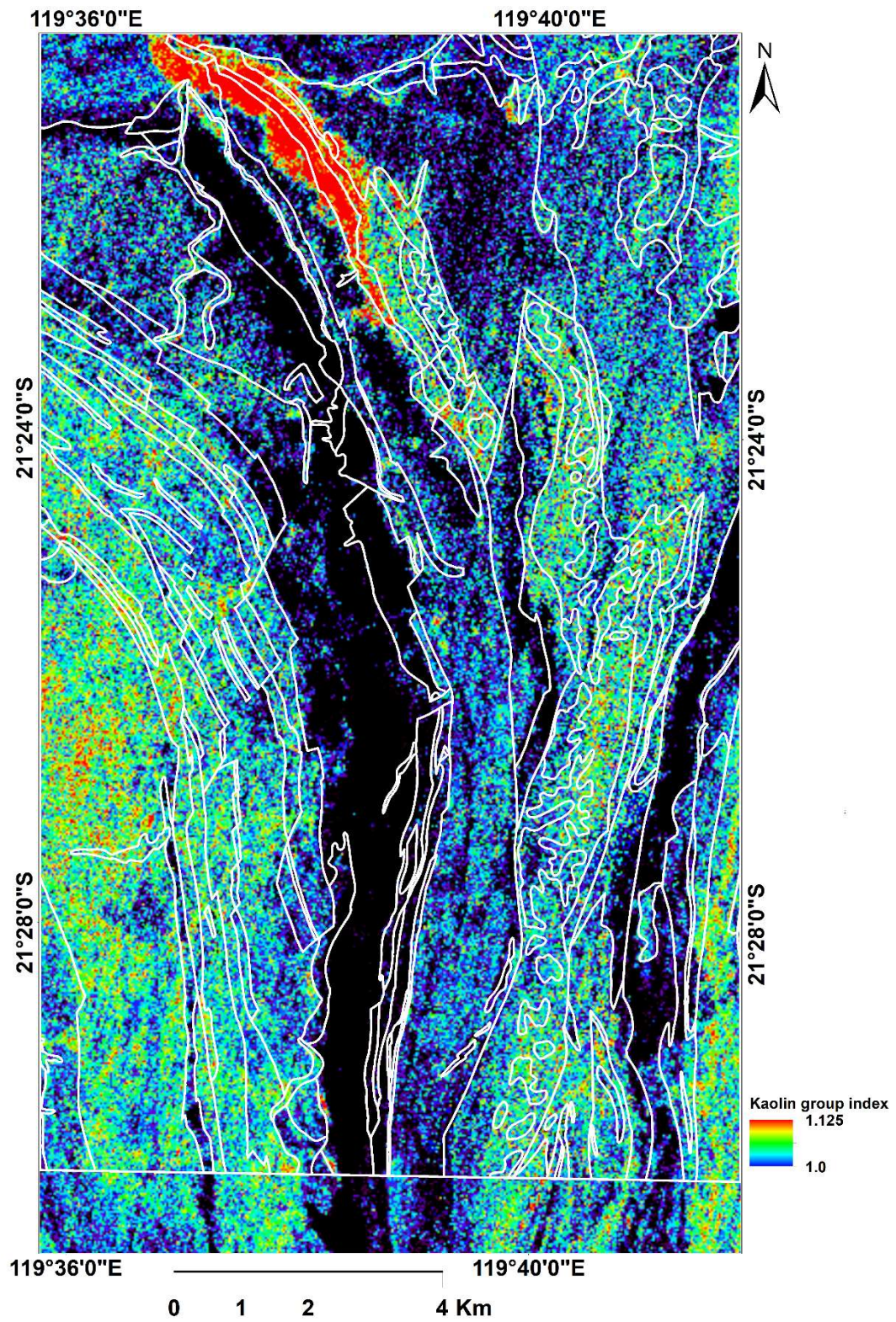
[Appendix 6](#): ASTER band ratio $((B6+B8)/B7)$ representing iron hydroxyl (FeOH) group mineral indices. The white lines are the lithological boundaries on the geological map.



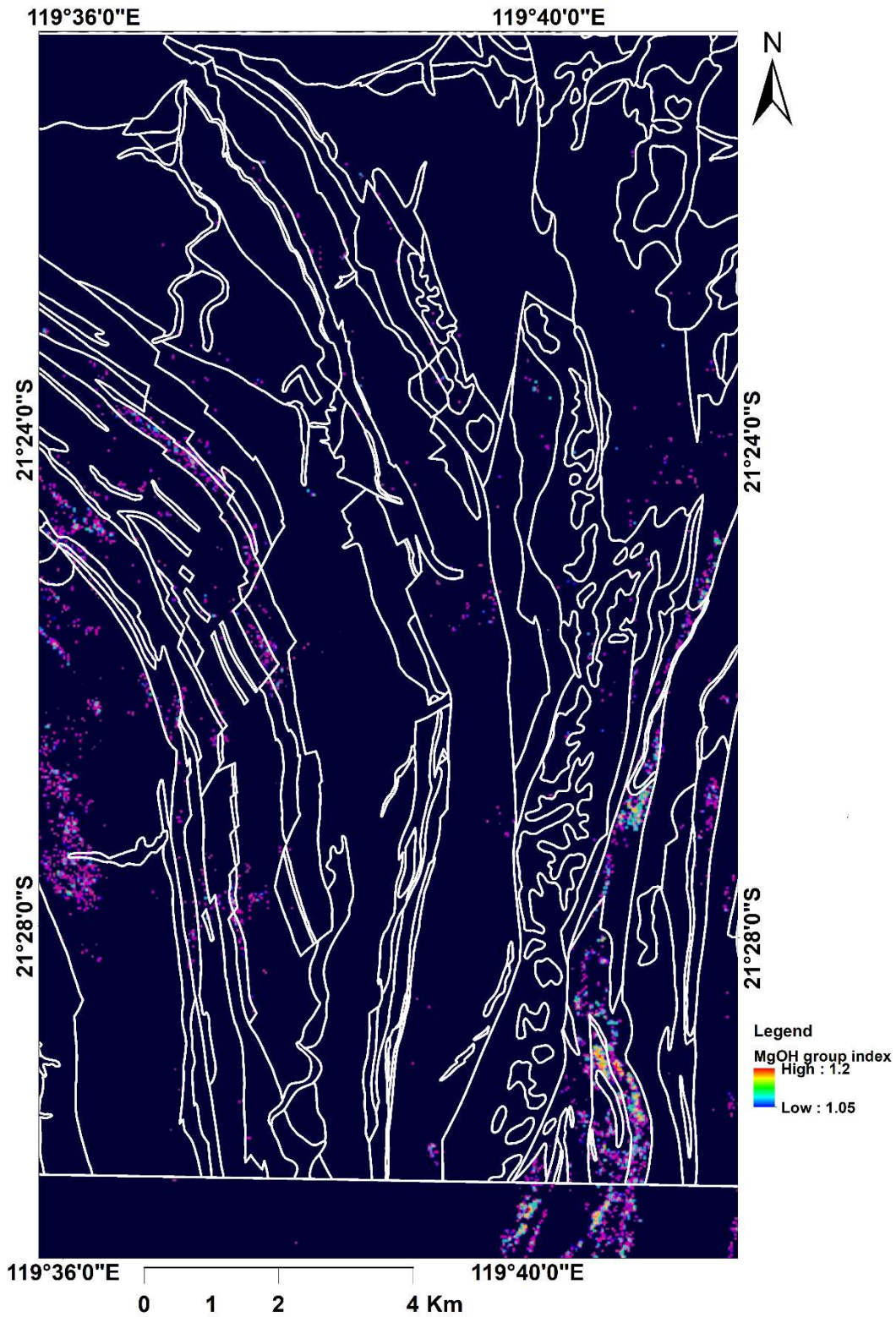
[Appendix 7](#): ASTER band ratio (B5+B7)/B6 showing AIOH group mineral indices. The white lines are boundaries of the geological map.



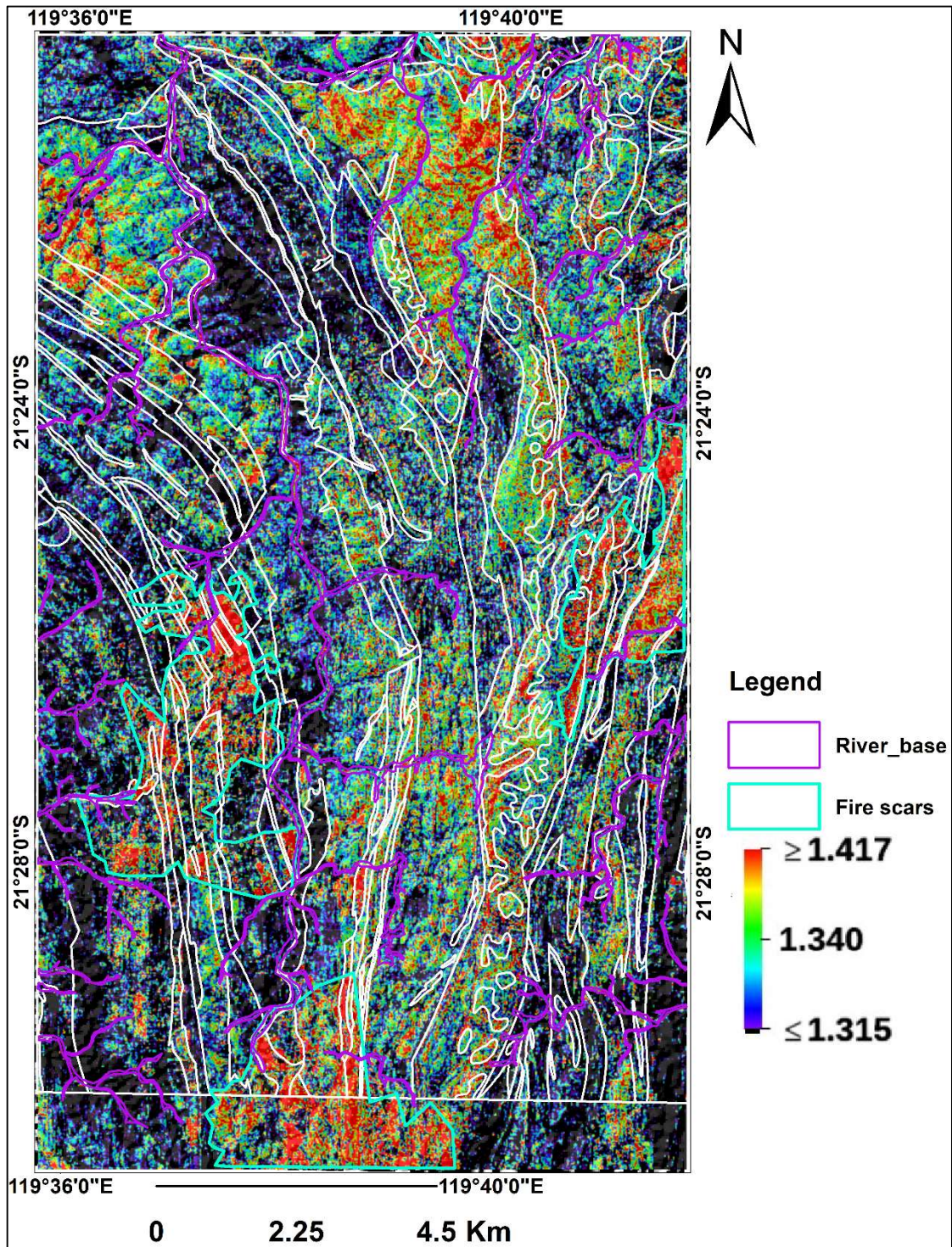
[Appendix 8](#): A map showing kaolin group mineral index produced by ASTER band ratio (B6/B5). The white lines are boundaries from the geological map.



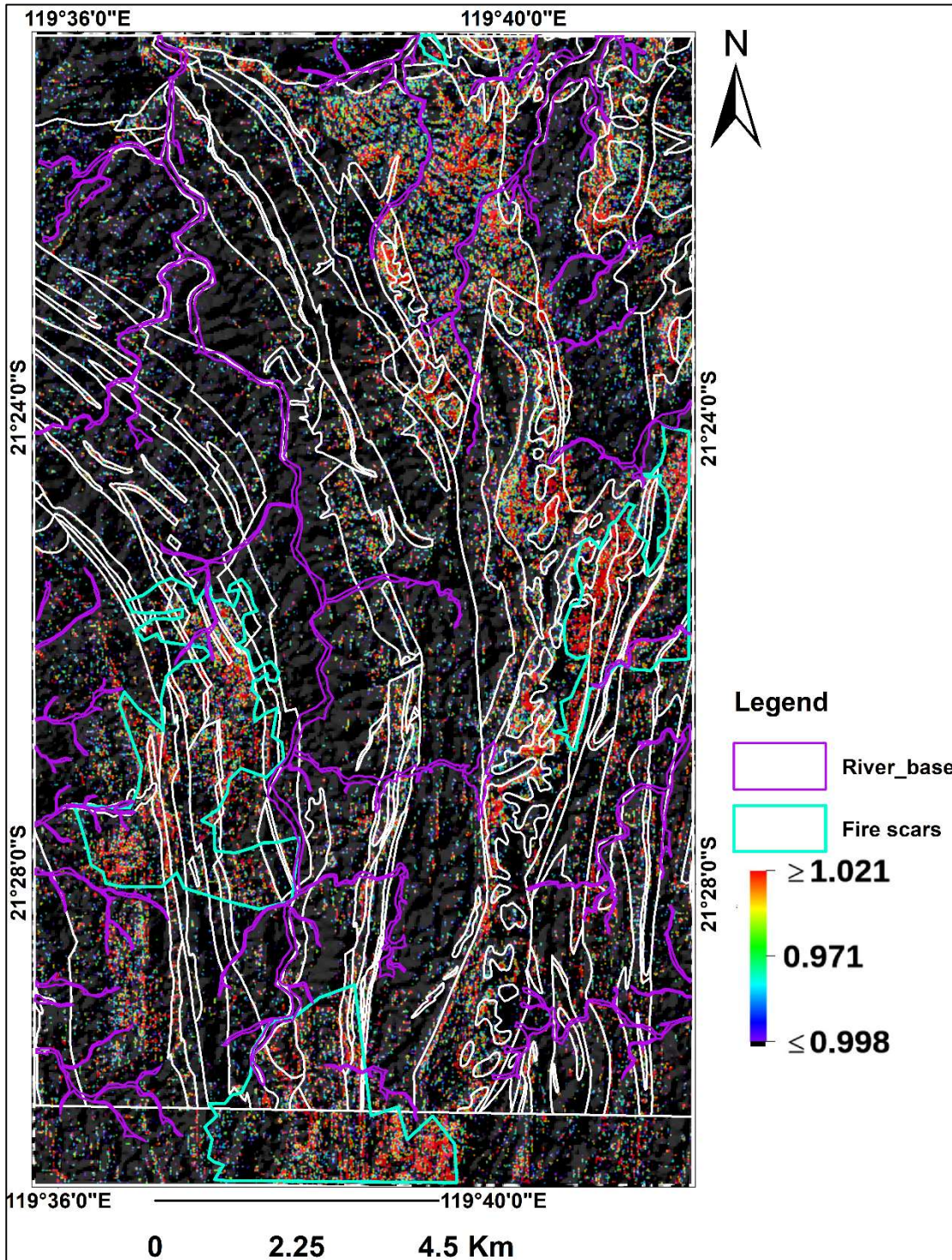
[Appendix 9](#): A map showing MgOH group mineral indices produced by ASTER band ratio $(B6+B9)/(B7+B8)$. The white lines are boundaries from the geological map.



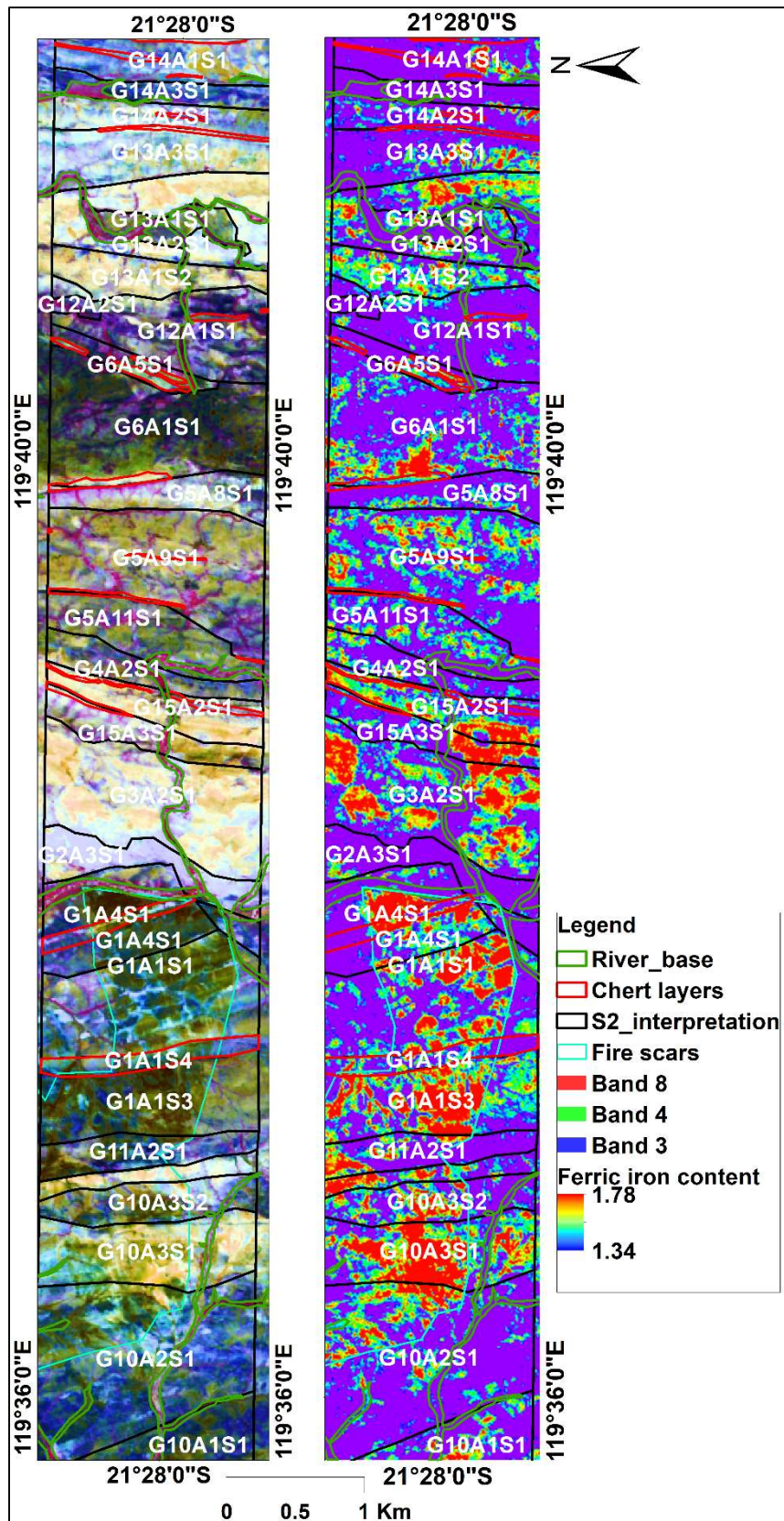
Appendix 10: Sentinel-2 band ratio $(B6+B9)/(B3+B8A)$ showing hematite occurrences.



Appendix 11: Sentinel-2 band ratio $(B6+B7)/(B8A+B9)$ showing goethite mineral occurrences.



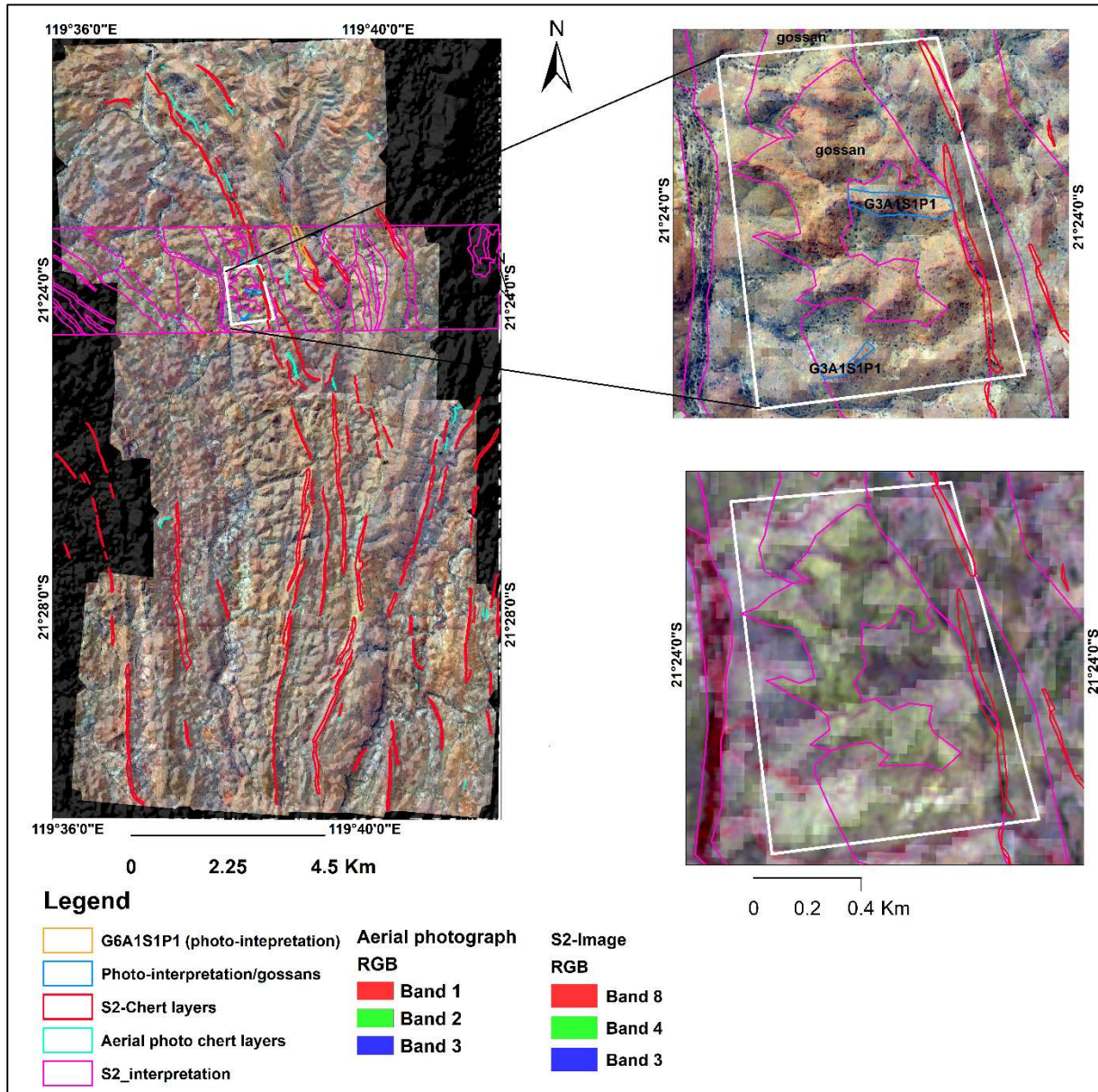
Appendix 12: Sentinel-2 interpretation of the validation area. The map on the left side is Sentinel-2 color composite, and the one on the right side is the Sentinel-2 band ratio (B4/B3) representing ferric iron content.



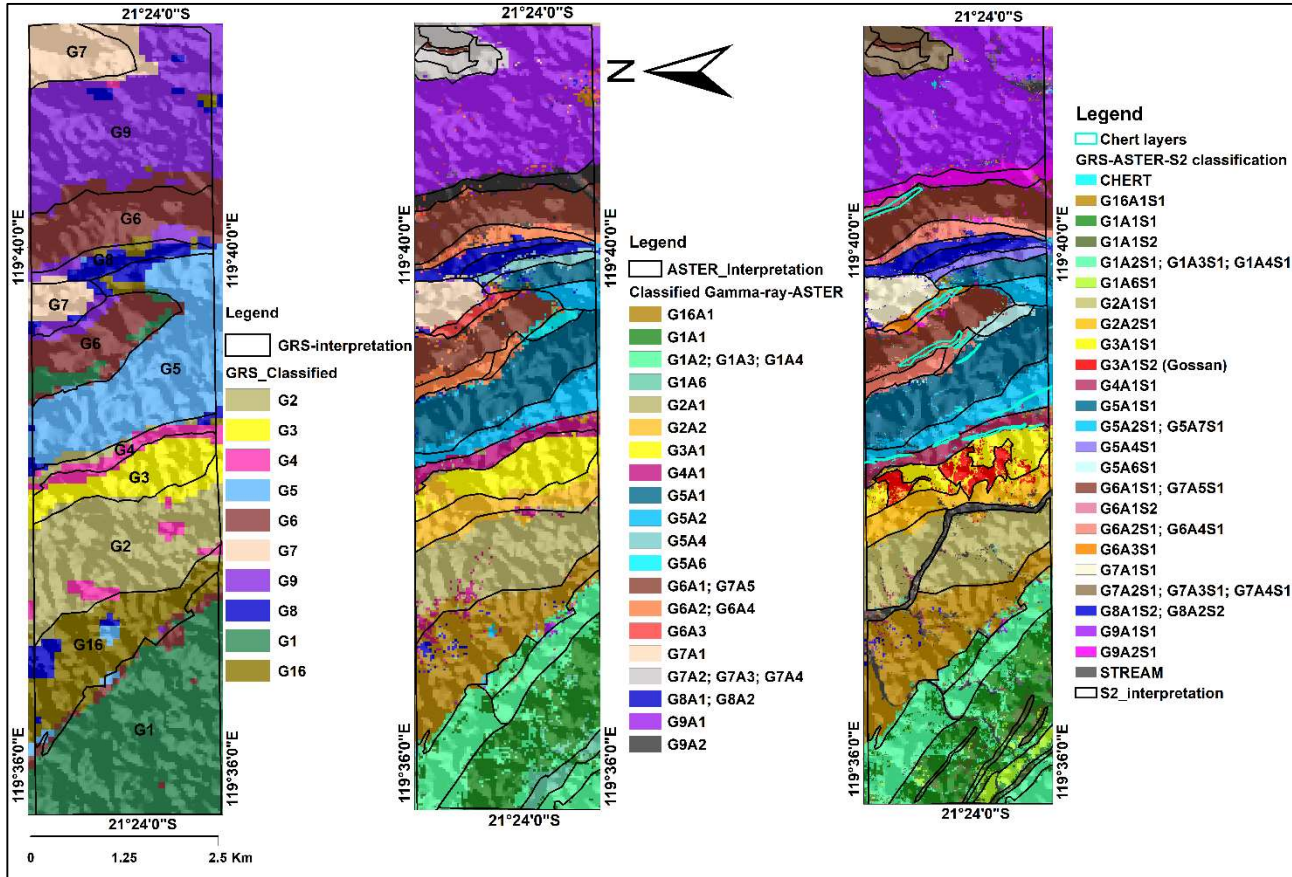
Legend of the map on Appendix 12

G10A3S2	Metabasalt and metadolerite
G11A1S1	Schistose, metamonzogranite
G11A2S1	Talc-carbonate chlorite serpentine, carbonate-schist
G12A1S1	Metaperidotite and serpentine-chlorite_schist, schistose
G12A2S1	Metaperidotite and serpentine-schist; metadunite, chert
G13A1S1	Porphyritic rhyolite and rhyodacite, local felsic volcanic rocks
G13A1S2	Metaperidotite and serpentine_chlorite schist
G13A2S1	Partly consolidated colluvial sand, silt, and gravel, scree and talus
G13A3S1	Interlayered psammitic and pelitic rocks, shale, siltstone, and sandstone
G14A1S1	Carbonate_altered and silicified, fine to medium-grained mafic schist
G14A2S1	Shale, pelitic schist, siltstone
G14A3S1	Carbonate_altered and silicified, mafic schist
G15A2S1	Quartz-porphyritic rhyolite, locally schistose, layered chert

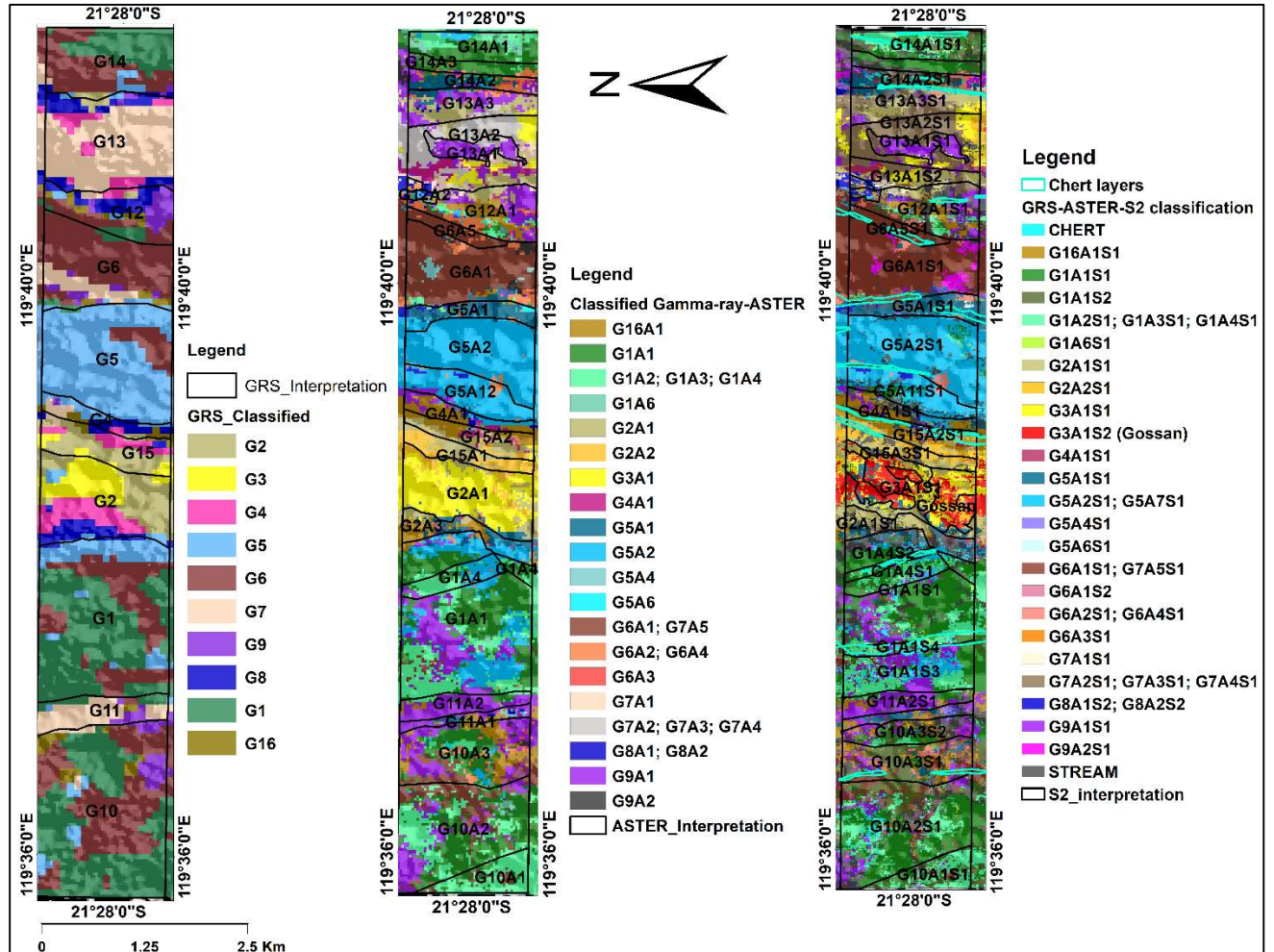
[Appendix 13](#): Aerial photograph and sentinel-2 images with overlaying chert layers interpreted using both of the datasets. This map shows the gossanous features of the Duffer formation and how does it look like in the aerial photograph and Sentinel-2 image. It also indicates how the boundaries interpreted using Sentinel-2 data were validated using the aerial photograph.



Appendix 14: Stepwise image classifications on the training area; gamma-ray image classification (left); stacked gamma-ray and ASTER image classification (middle); stacked gamma-ray, ASTER, and Sentinel-2 image classification (right).



Appendix 15: Stepwise image classifications on the validation area; gamma-ray image classification (left); stacked gamma-ray and ASTER image classification (middle); stacked gamma-ray, ASTER, and Sentinel-2 image classification (right).



[Appendix 16:](#) Accuracy estimation of the gamma-ray image classification in the training area

Confusion Matrix: [GRS-Training area] (122x199x1)

Overall Accuracy = (712/773) 92.1087%

Kappa Coefficient = 0.9102

Class	Commission (Percent)	Omission (Percent)	Commission (Pixels)	Omission (Pixels)	
G1	151	5.38	3.91	7/130	5/128
G16	1	9.78	5.68	9/92	5/88
G2	243	0.00	7.92	0/93	8/101
G3	8	1.89	1.89	1/53	1/53
G4	41	40.00	14.29	8/20	2/14
G5		0.00	7.07	0/92	7/99
G6	2	8.74	9.62	9/103	10/104
G7		11.54	9.80	6/52	5/51
G8	5	41.94	18.18	13/31	4/22
G9	29	7.48	12.39	8/107	14/113

Class	Prod. Acc. (Percent)	User Acc. (Percent)	Prod. Acc. (Pixels)	User Acc. (Pixels)	
G1	151	96.09	94.62	123/128	123/130
G16	1	94.32	90.22	83/88	83/92
G2	243	92.08	100.00	93/101	93/93
G3	8	98.11	98.11	52/53	52/53
G4	41	85.71	60.00	12/14	12/20
G5		92.93	100.00	92/99	92/92
G6	2	90.38	91.26	94/104	94/103
G7		90.20	88.46	46/51	46/52
G8	5	81.82	58.06	18/22	18/31

[Appendix 17](#): Accuracy estimation of the stacked gamma-ray and ASTER image classification in the training area

Confusion Matrix: [GRS-ASTER-Training area] (352x612x1)

Overall Accuracy = (5722/6273) 91.2163%

Kappa Coefficient = 0.9054

Class		Commission (Percent)	Omission (Percent)	Commission (Pixels)	Omission (Pixels)
G1A2	32	18.95	7.64	65/343	23/301
G1A3		37.84	4.17	42/111	3/72
G1A6	1	31.63	14.10	31/98	11/78
G1A1		5.46	26.61	25/458	157/590
G1A4	3	24.69	15.89	59/239	34/214
G16A1		3.80	8.98	18/474	45/501
G2A1		2.17	5.05	10/461	24/475
G2A2		19.66	11.74	46/234	25/213
G3A1		6.27	12.03	22/351	45/374
G4A1		15.68	5.45	29/185	9/165
G5A2		10.45	10.45	23/220	23/220
G5A1		3.04	5.56	16/526	30/540
G5A6		2.44	0.00	1/41	0/40
G5A4		25.30	18.42	21/83	14/76
G6A1		2.65	4.86	16/603	30/617
G6A2	1	21.82	11.64	36/165	17/146
G6A3	5	21.92	5.00	16/73	3/60
G6A4	4	0.00	5.71	0/33	2/35
G8A1		8.00	4.17	8/100	4/96
G8A2		32.35	9.80	44/136	10/102
G7A1		3.15	3.15	4/127	4/127
G7A2		17.46	1.89	11/63	1/53
G7A3		3.13	6.06	1/32	2/33
G7A4		0.00	2.27	0/43	1/44
G7A5		8.33	0.00	1/12	0/11
G9A1		0.43	2.20	4/939	21/956
G9A2		1.63	9.70	2/123	13/134

Class		Prod. Acc. (Percent)	User Acc. (Percent)	Prod. Acc. (Pixels)	User Acc. (Pixels)
G1A2	32	92.36	81.05	278/301	278/343
G1A3		95.83	62.16	69/72	69/111
G1A6	1	85.90	68.37	67/78	67/98
G1A1		73.39	94.54	433/590	433/458
G1A4	3	84.11	75.31	180/214	180/239

DATA INTEGRATION FOR RECONSTRUCTING OF VOLCANO-SEDIMENTARY SEQUENCES IN COONGAN GREENSTONE BELT EASTERN PILBARA CRATON,
WESTERN AUSTRALIA

G16A1		91.02	96.20	456/501	456/474
G2A1		94.95	97.83	451/475	451/461
G2A2		88.26	80.34	188/213	188/234
G3A1		87.97	93.73	329/374	329/351
G4A1		94.55	84.32	156/165	156/185
G5A2		89.55	89.55	197/220	197/220
G5A1		94.44	96.96	510/540	510/526
G5A6		100.00	97.56	40/40	40/41
G5A4		81.58	74.70	62/76	62/83
G6A1		95.14	97.35	587/617	587/603
G6A2	1	88.36	78.18	129/146	129/165
G6A3	5	95.00	78.08	57/60	57/73
G6A4	4	94.29	100.00	33/35	33/33
G8A1		95.83	92.00	92/96	92/100
G8A2		90.20	67.65	92/102	92/136
G7A1		96.85	96.85	123/127	123/127
G7A2		98.11	82.54	52/53	52/63
G7A3		93.94	96.88	31/33	31/32
G7A4		97.73	100.00	43/44	43/43
G7A5		100.00	91.67	11/11	11/12
G9A1		97.80	99.57	935/956	935/939
G9A2		90.30	98.37	121/134	121/123

[Appendix 18](#): Accuracy estimation of the stacked gamma-ray, ASTER and Sentinel-2 image classification in the training area

Confusion Matrix: [GRS-ASTER-S2-Training area] (1057x1835x1)

Overall Accuracy = (55047/60858) 90.4515%

Kappa Coefficient = 0.8970

Class	Commission (Percent)	Omission (Percent)	Commission (Pixels)	Omission (Pixels)
G1A2S1	18.60	5.94	369/1984	102/1717
CERT	1	59.26	128/216	19/107
G1A3S1	23.02	4.21	102/443	15/356
G1A1S2	56.11	18.13	670/1194	116/640
G1A6S1	31.84	7.35	206/647	35/476
G1A1S1	7.98	34.32	269/3373	1622/4726
G1A4S1	28.81	14.11	601/2086	244/1729
G16A1S1	5.28	8.26	308/5830	497/6019
G2A1S2	1.76	9.49	85/4826	497/5238
G2A2S1	12.49	7.03	315/2522	167/2374
G3A1S1	7.53	17.53	147/1953	384/2190
G3A1S2	24.69	13.07	279/1130	128/979
G4A1S1	17.44	5.40	196/1124	53/981
G5A2S1	7.23	9.17	132/1825	171/1864
G5A1S1	1.63	7.62	81/4977	404/5300
G5A7S1	17.09	3.43	87/509	15/437
G5A6S1	18.15	2.70	96/529	12/445
G6A1S1	3.69	11.85	151/4094	530/4473
G6A2S1	16.17	6.42	340/2103	121/1884
G6A4S1	28.52	1.42	83/291	3/211
G6A3S1	14.42	3.79	47/326	11/290
G6A1S2	16.00	0.59	32/200	1/169
G5A4S1	11.28	4.70	67/594	26/553
G8A1S1	5.50	3.29	48/872	28/852
G8A2S1	15.70	8.37	155/987	76/908
G7A1S1	2.33	1.37	24/1029	14/1019
G7A2S1	5.31	6.28	46/867	55/876
G7A3S1	12.29	0.32	43/350	1/308
G7A5S1	4.64	2.70	7/151	4/148
G9A1S1	0.66	2.58	69/10476	276/10683
G9A2S1	7.72	6.96	124/1607	111/1594
STREAM	35.82	7.53	500/1396	73/969
G7A4S1	1.15	0.00	4/347	0/343

Class	Prod. Acc. (Percent)	User Acc. (Percent)	Prod. Acc. (Pixels)	User Acc. (Pixels)
G1A2S1	94.06	81.40	1615/1717	1615/1984
CERT 1	82.24	40.74	88/107	88/216
G1A3S1	95.79	76.98	341/356	341/443
G1A1S2	81.88	43.89	524/640	524/1194
G1A6S1	92.65	68.16	441/476	441/647
G1A1S1	65.68	92.02	3104/4726	3104/3373
G1A4S1	85.89	71.19	1485/1729	1485/2086
G16A1S1	91.74	94.72	5522/6019	5522/5830
G2A1S2	90.51	98.24	4741/5238	4741/4826
G2A2S1	92.97	87.51	2207/2374	2207/2522
G3A1S1	82.47	92.47	1806/2190	1806/1953
G3A1S2	86.93	75.31	851/979	851/1130
G4A1S1	94.60	82.56	928/981	928/1124
G5A2S1	90.83	92.77	1693/1864	1693/1825
G5A1S1	92.38	98.37	4896/5300	4896/4977
G5A7S1	96.57	82.91	422/437	422/509
G5A6S1	97.30	81.85	433/445	433/529
G6A1S1	88.15	96.31	3943/4473	3943/4094
G6A2S1	93.58	83.83	1763/1884	1763/2103
G6A4S1	98.58	71.48	208/211	208/291
G6A3S1	96.21	85.58	279/290	279/326
G6A1S2	99.41	84.00	168/169	168/200
G5A4S1	95.30	88.72	527/553	527/594
G8A1S1	96.71	94.50	824/852	824/872
G8A2S1	91.63	84.30	832/908	832/987
G7A1S1	98.63	97.67	1005/1019	1005/1029
G7A2S1	93.72	94.69	821/876	821/867
G7A3S1	99.68	87.71	307/308	307/350
G7A5S1	97.30	95.36	144/148	144/151
G9A1S1	97.42	99.34	10407/10683	10407/10476
G9A2S1	93.04	92.28	1483/1594	1483/1607
STREAM	92.47	64.18	896/969	896/1396
G7A4S1	100.00	98.85	343/343	343/347

[Appendix 19:](#) Accuracy estimation of the gamma-ray image classification in the validation area.

Confusion Matrix: [GRS-Validation area] (122x199x1)

Overall Accuracy = (157/197) 79.6954%

Kappa Coefficient = 0.7325

	Class	Commission (Percent)	Omission (Percent)	Commission (Pixels)	Omission (Pixels)
G1	151	0.00	41.03	0/46	32/78
G2	243	0.00	25.81	0/23	8/31
G4	41	72.73	0.00	8/11	0/3
G5		16.39	0.00	10/61	0/51
G6	2	39.29	0.00	22/56	0/34

	Class	Prod. Acc. (Percent)	User Acc. (Percent)	Prod. Acc. (Pixels)	User Acc. (Pixels)
G1	151	58.97	100.00	46/78	46/46
G2	243	74.19	100.00	23/31	23/23
G4	41	100.00	27.27	3/3	3/11
G5		100.00	83.61	51/51	51/61
G6	2	100.00	60.71	34/34	34/56

[Appendix 20](#): Accuracy estimation of the stacked gamma-ray and ASTER image classification in the validation area.

Confusion Matrix: [GRS-ASTER-Validation area] (352x612x1)

Overall Accuracy = (874/1276) 68.4953%

Kappa Coefficient = 0.5666

Class	Commission (Percent)	Omission (Percent)	Commission (Pixels)	Omission (Pixels)
G1A1	24.39	49.01	50/205	149/304
G1A2	32 63.77	82.64	44/69	119/144
G2A2	0.00	66.67	0/5	10/15
G5A2	39.94	5.32	272/681	23/432
G6A1	0.00	9.06	0/261	26/287
G5A1	57.78	70.31	26/45	45/64
G4A1	100.00	100.00	10/10	30/30

Class	Prod. Acc. (Percent)	User Acc. (Percent)	Prod. Acc. (Pixels)	User Acc. (Pixels)
G1A1	50.99	75.61	155/304	155/205
G1A2	32 17.36	36.23	25/144	25/69
G2A2	33.33	100.00	5/15	5/5
G5A2	94.68	60.06	409/432	409/681
G6A1	90.94	100.00	261/287	261/261
G5A1	29.69	42.22	19/64	19/45
G4A1	0.00	0.00	0/30	0/10

[Appendix 21](#): Accuracy estimation of the stacked gamma-ray ASTER and Sentinel-2 image classification in the validation area

Confusion Matrix: [GRS-ASTER-S2-Validation area] (1057x1835x1)

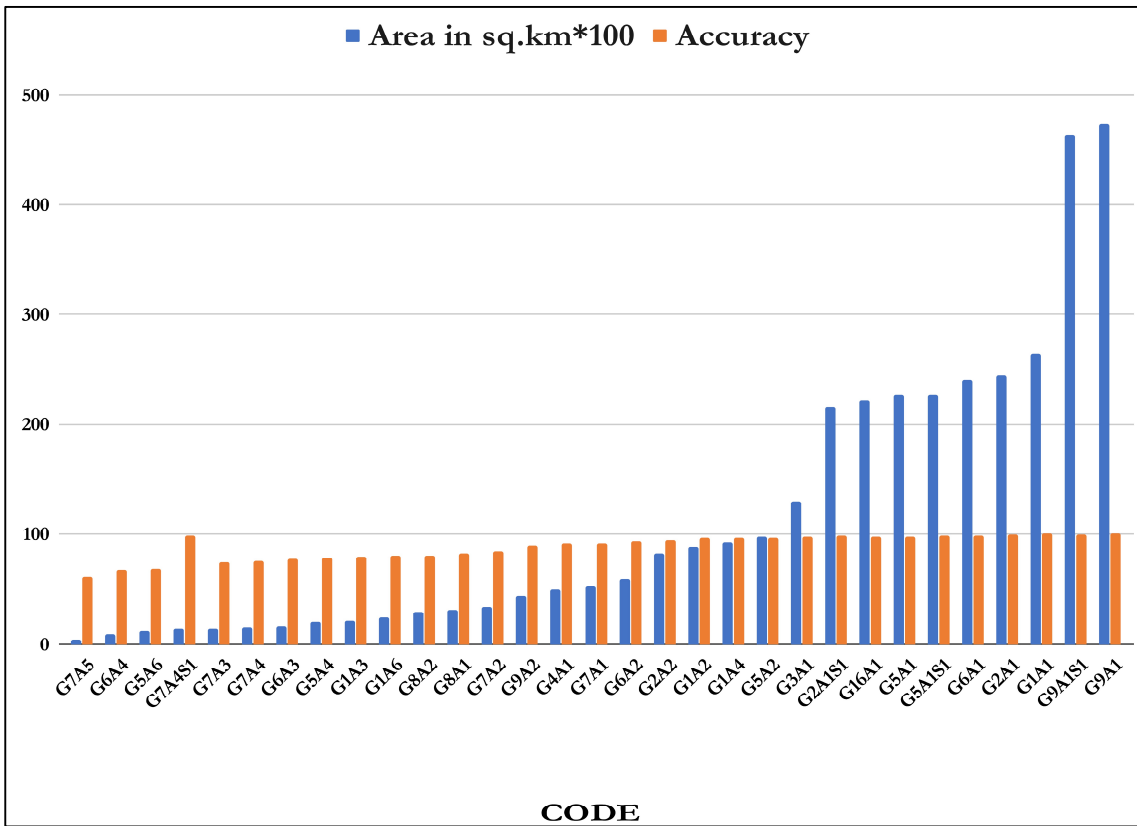
Overall Accuracy = (1420/2093) 67.8452%

Kappa Coefficient = 0.5930

Class	Commission (Percent)	Omission (Percent)	Commission (Pixels)	Omission (Pixels)
G1A1S1	75.48	80.46	157/208	210/261
G1A2S1	64.68	60.91	174/269	148/243
Chert 1	95.00	93.55	38/40	29/31
G16A1S1	100.00	100.00	86/86	8/8
G2A2S1	0.00	88.61	0/9	70/79
G4A1S1	100.00	100.00	52/52	72/72
G5A2S1	4.40	11.81	22/500	64/542
G5A1S1	41.36	17.65	79/191	24/136
G6A1S1	8.81	0.00	65/738	0/673
G7A1S1	0.00	100.00	0/0	48/48

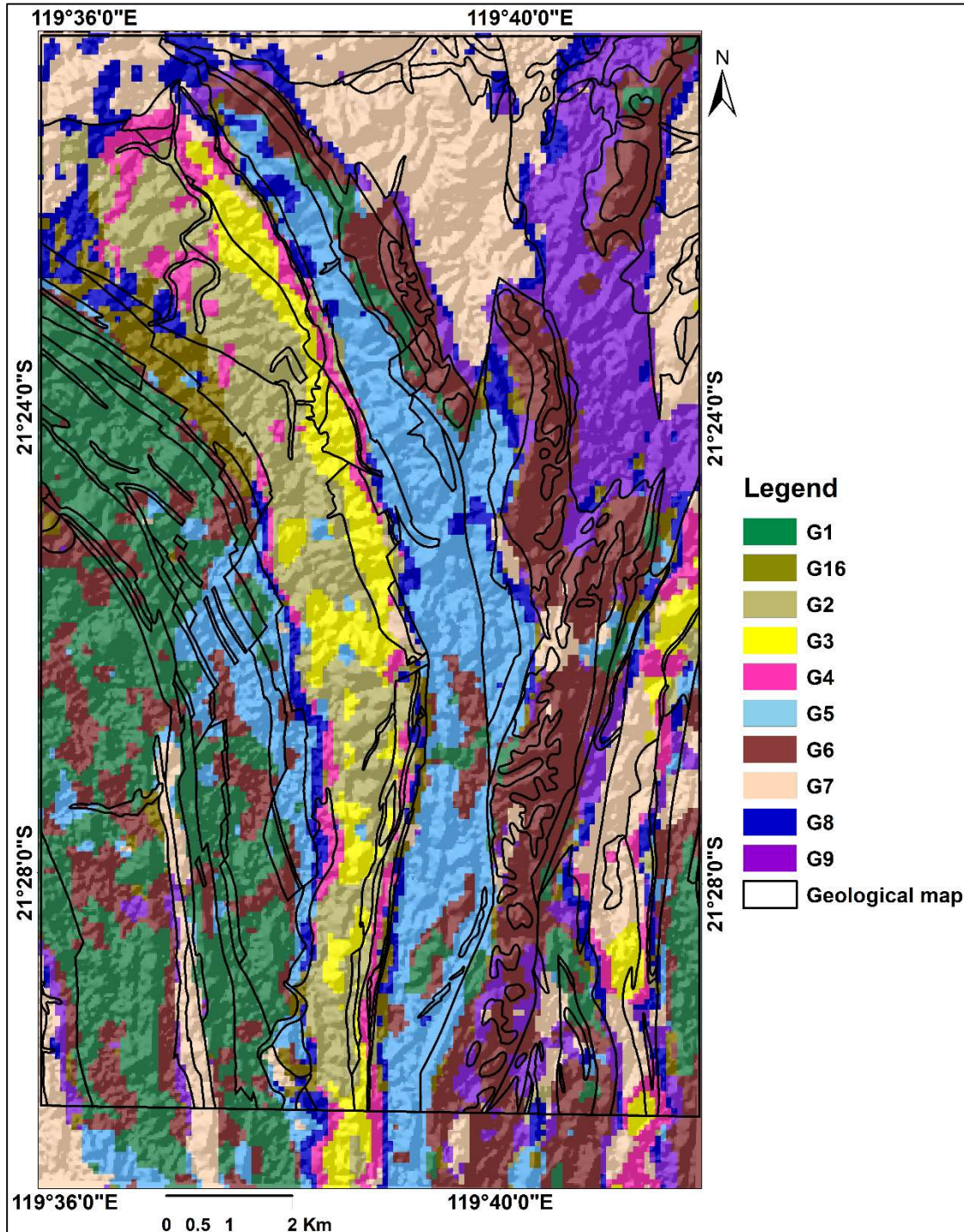
Class	Prod. Acc. (Percent)	User Acc. (Percent)	Prod. Acc. (Pixels)	User Acc. (Pixels)
G1A1S1	19.54	24.52	51/261	51/208
G1A2S1	39.09	35.32	95/243	95/269
CERT 1	6.45	5.00	2/31	2/40
G16A1S1	0.00	0.00	0/8	0/86
G2A2S1	11.39	100.00	9/79	9/9
G4A1S1	0.00	0.00	0/72	0/52
G5A2S1	88.19	95.60	478/542	478/500
G5A1S1	82.35	58.64	112/136	112/191
G6A1S1	100.00	91.19	673/673	673/738
G7A1S1	0.00	0.00	0/48	0/0

Appendix 22: Area versus accuracy of stacked gamma-ray, ASTER, and Sentinel-2 image classification in the training area.



[Appendix 23](#)

Maximum likelihood classified map of Gamma-ray data. Spectral signatures used to classified this map are collected from the training area (extrapolation). The legend of this map is illustrated on the next page.



Legend of appendix 23: the stratigraphic units are summarized from the geological map and the field data.

<i>Symbol</i>	<i>Stratigraphic unit</i>
<i>G1</i>	Mafic and ultramafic rocks
<i>G2 & G16</i>	Felsic volcanics and volcanoclastic sediments
<i>G3</i>	Felsic volcanics and volcanoclastic sediments, relatively higher radioelement contents
<i>G4</i>	Komatiite basalt; relatively high radioelements
<i>G5</i>	Potassium enriched komatiite basalt and felsic volcanics
<i>G6</i>	Banded iron formation
<i>G7</i>	Sandstones and unconsolidated sediments